Ore Geology Reviews 105 (2019) 310–336

Contents lists available at ScienceDirect

Ore Geology Reviews

journal homepage: www.elsevier.com/locate/oregeorev

How do metals escape from magmas to form porphyry-type ore deposits?

Jean-Louis Vigneresse[a,*], Laurent Truche[b], Antonin Richard[a]

[a] GéoRessources, UMR 7539, Université de Lorraine, 54506 Vandoeuvre/Nancy Cédex, France
[b] ISTerre, Université de Grenoble-Alpes, 38400 Saint-Martin-d'Hères, France

ARTICLE INFO

Keywords:
Ore formation
Fluid sparging
Multiple intrusions
Rates of processes
Diffusion/advection

ABSTRACT

Many precious and base metals (Cu, Au, Ag, Mo, W, Sn) in porphyry-type deposits are extracted from a granitic to granodioritic silicate melt and transported by magmatic-hydrothermal fluids to the site of ore deposition. Metals abundance increases from some ppb in the melt to % in ore bodies. Assuming a unique magmatic source for metals, it implies an exceptional combination of enrichment process acting over up to 4 orders of magnitude. Previous models of magma differentiation and hydrothermal circulations omitted to consider the role of metal segregation during magma chamber evolution. Models for the formation and evolution of intrusions have recently shifted from the so-called melting-storage-assimilation-homogenization (MASH) paradigm, basically steady state, to the mantle-melting-segregation-ascent-emplacement (m(M-SAE)) paradigm, dynamic and discontinuous in time. Successive magma injections of variable compositions progressively build the magma chamber. This is supported by field relations (e.g. cross-cutting dykes and stocks), textures (e.g. partially resorbed enclaves, or mineral fabrics), geochemistry (e.g. hybridization signatures), and age dating aswell as istopic studies. As melt crystallizes and forms a mush (> 50% crystals), volatiles also exsolve forming a magmatic volatile phase (MVP) while melt motion slows down. Metals partition between the three phases: melt; crystals; and MVP. They generally prefer the MVP owing to more favorable partition coefficients. This is indicated by metal content in coeval melt and fluid inclusions with homogenization temperatures above 600 °C, or in volcanic fumaroles. Here, by simulating the physical interactions between the three phases we suggest a model of fluid sparging, during which metals segregate towards the MVP by diffusion and are further transported by advection as metal complexes. The model also provides estimates of metal enrichment. An undimensional Péclet number rules the competition between diffusion and advection, basically scaling with respect to the inverse of the product of melt viscosity (η) by metal diffusivity (D). The threshold value of the Péclet number between diffusion and advection is roughly 10^{-9}. Fast diffusive metals (Au, Cu, Ag, W) readily diffuse from silicate melt and towards bubbles of the MVP. To escape the mush through tubular structures, the MVP must overcome a critical gas saturation level (about 20% vol.) usually reached after several magma injections. Advection then takes over and transports the metal-enriched MVP towards the top of the magma chamber. This leads to nearly coeval (1) separation between a high salinity-liquid phase and a low-salinity vapor phase, (2) fluid-rock interactions resulting in potassic, advanced argillic and phyllic alterations and (3) metal deposition. The metal enrichment scales as the ratio between partition coefficient (i.e. related to the gradient in chemical potential), diffusivity (i.e. related to the gradient of concentration), and melt viscosity (i.e. related to the gradient of momentum). The rates at which all such gradients relax determe metals enrichment, inducing chemical and physical instabilities, leading to a cyclic process. The whole cycle also encompasses the case of a partial, non-completed, full enrichment yielding to barren intrusions. A tentative model generalizes the sparging fluid model to other metal deposits linked to an intrusion. Such generalization should be interpreted as predicting metal enrichment by 3–4 orders of magnitude, rather than predicting an exact value.

1. Introduction

Non-ferrous metals are diversely abundant in the Earth's crust and mantle, with average concentrations (i.e. Clarke values) usually ranging between the ppb and ppm levels. Nevertheless, magmatic-hydrothermal processes result in economic deposits in which metal concentrations

* Corresponding author at: GéoRessources, BP 70239, 54506 Vandoeuvre/Nancy Cédex, France.
E-mail addresses: jean-louis.vigneresse@univ-lorraine.fr (J.-L. Vigneresse), laurent.truche@univ-grenoble-alpes.fr (L. Truche), antonin.richard@univ-lorraine.fr (A. Richard).

https://doi.org/10.1016/j.oregeorev.2018.12.016
Received 8 May 2018; Received in revised form 10 December 2018; Accepted 17 December 2018
Available online 21 December 2018
0169-1368/

may reach the % level. Understanding the mechanisms yielding to such enrichment represents the first step towards more predictive exploration strategies, allowing distinguishing between potentially barren and fertile magmatic intrusions (Vigneresse, 2019).

Detailed studies and general reviews of magmatic-hydrothermal ore deposits have been evolving since the begining of the 20th century and are very abundant in the literature of economic geology (e.g. Sillitoe, 1973; 2010; Hedenquist and Lowenstern, 1994; Hattori and Keith, 2001; Ulrich and Heinrich, 2001; Halter et al., 2004; Simon et al., 2006; Audétat et al., 2008; Harris et al., 2008; Webster et al., 2009; Zajacz and Halter, 2009; Pettke et al., 2010; Richards, 2011). These studies focus primarily on the second half of the deposit's history during which metals are transported and deposited by magmatic-hydrothermal fluids (Williams-Jones and Heinrich, 2005). The prior deep magmatic evolution remains poorly documented (Wilkinson, 2013). The magmatic stage has been commonly described according to theMASH model (Hildreth and Moorbath, 1998) which accounts for a stationary chemical differentiation of the magma (Štemprok, 1982; Breiter et al., 1999). Recent investigations have shifted this paradigm toward a far more dynamic system, chemical (Lee et al., 2014) and/or mechanical (Vigneresse, 2008), that has consequences on the fate of metals during melt evolution. This paper focuses on the metal concentration processes that operate during the magmatic stage *sensu strico*. It provides pathways for exploration.

The paper starts with a brief review of what has changed in the concepts of an evolving intrusion, here simply designed as a magma chamber. Magma is examined from its three major phases: crystals, viscous melt and a magmatic volatile phase (MVP). All metals present into the initial source rock, and consequently into the initial melt, partition between those three phases. The interactions between them are constrained by field observations, numerical modelling and chemical or physical experiments. The observations and experiments identify the leading parameters that control magma chamber construction and evolution, and thus metals behavior (Fig. 1).

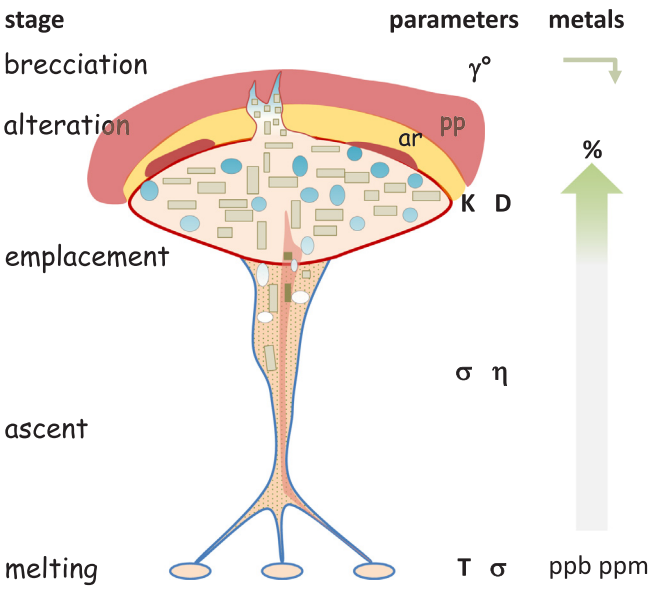

Fig. 1. Simplified cartoon, not to scale in space and time, showing the successive stages of magma intrusion; from melting; ascent; emplacement; alteration and brecciation. Several bursts of magma, with different composition and eventual different source (lower crust or mantle) fill the progressively crystallizing magma chamber, while a gaseous phase (MVP) exsolves. The corresponding parameters controling magma evolution are temperature (T) and stress (σ), viscosity (η). Partition coefficients (K) and diffusivity (D) control metal segregation from the melt toward the MVP. Their concentration (in blue) increases into the MVP due to fluid sparging of the melt. Finally, the MVP explodescreates bercciation at high strain rate (γ °), leading to metals deposition. The different alteration stages include from inward to outward: phyllic (ph), argilic (ar) and propylitic (pp) stages. (For interpretation of the references to colour in this figure legend, the reader is referred to the web version of this article.)

2. The magmatic stage

Before precipitating from hydrothermal fluids, metals already show high concentrations, indicating that the enrichment process starts during the magmatic stage. High temperature fluid and magma inclusions indicate such metals concentration. They are observed for instance as Cu in S-bearing MVP, as in Zaldivar, northern Chile (Campos et al., 2002; Harris et al., 2008; Rabbia et al., 2009). Au-bearing fluid inclusions are also observed from Bajo de la Alumbrera, Argentina (Ulrich and Heinrich, 2001). Homogenization temperatures recorded in Cu-Au-porphyry type deposits are commonly high, between 640 and 900 °C. They range from 720 to 780 °C in Bajo de la Alumbrera, Argentina (Ulrich and Heinrich, 2001), from 750 to 900 °C in Zaldivar, Chile (Campos et al., 2002), from 650 to 680 °C in La Escondida, Chile (Padilla-Garza et al., 2004) and from 640 to 725 °C in Bingham, Utah, USA (Roedder, 1971) for Cu-deposits. Mo-bearing porphyry deposits show homogenization temperatures > 600 °C in Hudson Bay Mountain, New Mexico (Bloom, 1981) and 550–650 °C in Henderson, Colorado (Carten et al., 1988). Au-mineralizations show temperatures between 400 and 460 °C in Nambija, Ecuador (Markowski et al., 2006) and 500–700 °C in various places in South Africa (Kolb, 2008). Those homogenization temperatures are the minimum temperature of the trapped fluids.

High temperature volcanic fumaroles also document metal enrichment up to several orders of magnitude relative to solidified lavas. High metal concentrations are observed at Mutnovsky and Kudryavy volcanoes, both in Kamchatka (Zelenski and Bortnikova, 2005). Aerosols and fumaroles indicate Cd-Pb-Bi and Pb-As-Bi sulphosalts; Pb-As and Bi sulphohalides; Cd, Pb, Tl halides; and an amorphous As-S compound. Similar enrichments in metals are also observed with native Au precipitates at Colima, Mexico, and Momotombo, Nicaragua (Taran et al., 1995; Taran et al., 2000) or aerosols from the Popocatepetl (Obenholzner et al., 2003). In Indonesia, the Merapi volcanic gases are enriched in metals relatively to the magma by factors ranging from 10^2 to 10^5 (Symonds et al., 1987). Metal-bearing precipitates surrounding the fumaroles are also chemically zoned with Bi, Cd, Pb, W, Mo, Zn and Cu, correlating with their respective diffusivities.

2.1. The changing conditions of a magma chamber evolution

The recent advances in magma chamber construction are rapidly reviewed below, focusing on their discontinuous nature, indicating cyclics aspects that have not been taken into sufficient account in previous models of igneous evolution related to porphyry-style ore deposits.

2.1.1. Magma chamber dynamics

A magma chamber basically consists of three major physical phases, namely a viscous melt, the solidified crystals and a magmatic volatile phase. Their respective amount evolves with time, from: (i) melt-dominant during partial melting, magma ascent and progressive crystallization (ii) solid-dominant during magma emplacement and cooling, with a mush composed of crystals (> 50%), a residual melt and a developing MVP, and (iii) solid-only during final solidification, with often explosive expulsion of the MVP and brecciation of the solid phase (Fig. 1). During the successive stages, from melting to emplacement, metals are incorporated to the melt, and progressively partition either into the MVP or into the first formed crystals. Partition coefficients and diffusivity govern their repartition between phases. Both parameters vary according to the melt and MVP properties, and are particularly sensitive to temperature. When incorporated to the solid phase, metals

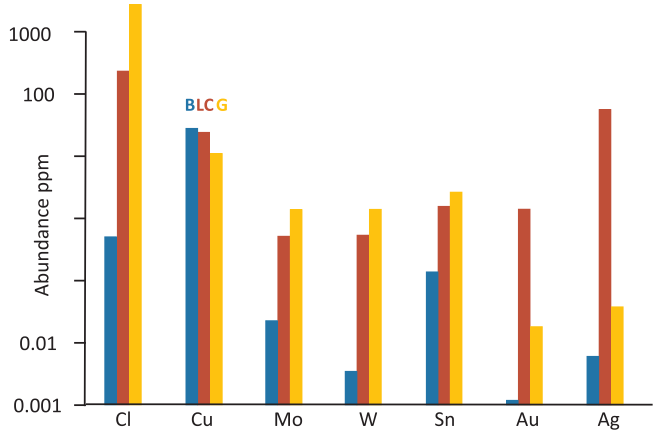

Fig. 2. Logarithmic abundance of metals involved in ore deposits, with their respective amount (in ppm) in basalts (B) and granites (G) (Hedenquist and Lowenstern, 1994) and in the lower crust (LC) (Rudnick and Gao, 2003). The elements (Au, Ag, Mo, Cl, Sn and W) are represented always in the same order and same colours in the different figures.

become inert, since their diffusivity increase by about 6 orders of magnitude.

2.1.2. The viscous melt

The melt in prohyry-type intrusions is commonly of dioritic to granodioritic composition. It basically derives from a calco-alkaline magma and may incorporate more mafic melts that mix with the previous melt forming hybrid magmas, or remain as massive gabbroic enclaves (Castro et al., 1991). Such a magma may also incorporate sulfides that generally remain unmixed (Eichelberger, 1975). Depending of their origin, crustal or mantellic, metals are in abundance of the source (Rudnick and Gao, 2003). The amount of material scavenged from the country rocks, i.e.the upper crust, during ascent and emplacement is negligible in a first approach, representing a maximum of 10%. Most metals from the periodic table are present (Fig. 2) into the melt in variable proportions, according to the "Clarke" distribution, from 10^{-4} to 10^{2} ppm (Laznica, 1999). The Goldschmidt's classification distinguishes between lithophiles, chalcophiles and siderophiles elements from their affinities for the upper crust, mantle or core (Goldschmidt, 1954). Conquently, the metal abundance varies, some being commonly more present in the continental crust, and derived granites, than into mantle-derived magmas (Fig. 2). For instance, a typical arc basalt contains 50–200 ppm Cu (Harris et al., 2005) and a 2–5 ppb of Au (Crocket and Teruta, 1977). By comparison, the upper crust indicates 28 ppm of Cu and 0.3 ppb of Au (Rudnick and Gao, 2003).

The controlling parameter that rules melting is essentially temperature (T). During dehydration melting, water is liberated by aqueous minerals breakdown, such as muscovite, biotite and amphibole (Clemens, 1990). Heat brought from the mantle helps in this process. The ambient stress pattern (σ) induces mechanical instabilities on the viscous melt (Fig. 1). It concentrates melts into small pockets and then forms veins that coalesce (Rabinowicz and Vigneresse, 2004). Veins ascend toward zones of lower strain, i.e. local extensional zones (Vigneresse, 1995), making the whole process discontinuous in space and time.

Chemically, silicate magmas evolve toward a more silicic (i.e. differenciated) composition. Here, the adopted alphabet classification (A-, I- and S-type) is adopted for granites as a simplification (Chappell and White, 1977, 2001; Eby, 1992). Silicate melts are buffered in oxygen and sulfur, i.e. in redox conditions (Fig. 3a). I-type granites are oxidized and follow the nickel-nickel oxide (NNO) buffer whereas S-type granites are reduced, and follow the fayalite-magnetite-quartz (FMQ) buffer (Kishima and Sakai, 1984). They also follow a pyrite-pyrrhotite-magnetite (py-po-mt) buffer for S (Crerar et al., 1978), indicating a f_{SO2}/f_{H2S} of about 0.5 or less. In a similar way, A-type magmas are buffered above the FMQ buffer (Fig. 3b).

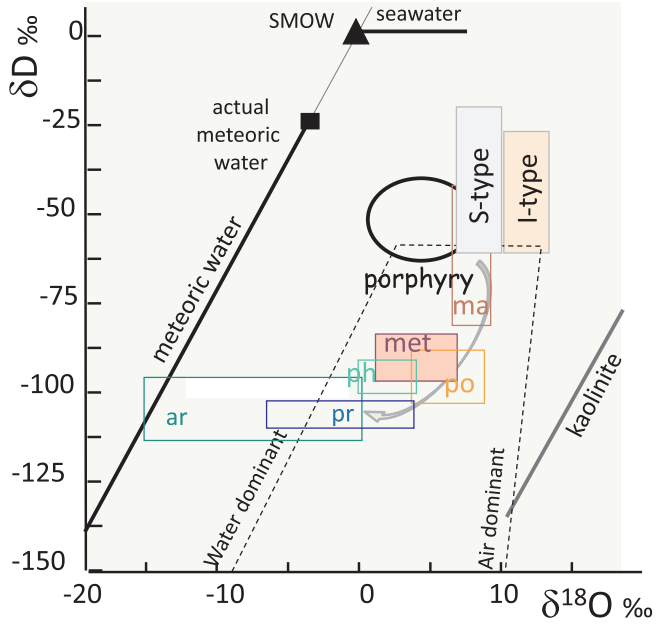

Fig. 3. Redox buffer conditions (a), in terms of oxygen fugacity (f_{O2}) and (b) sulphur fugacity (f_{S2}), both scaled in temperature. Different buffers are indicated: Hematite-magnetite (HMT), sulphide-sulphate (SO_2-H_2S), nickel-nickel oxide (NNO), fayalite-magnetite-quartz (FMQ), pyrite-bornite-chaleopyrite (py-bo-cp), pyrite-pyrrhotite (py-po), arsenopyrite- loellingite-pyrrhotite (asp-lo + po). The fugacity ratio of sulphate/sulphide is also indicated by dashed lines. The various fields relate to basalts, A-, I- and S-type granites, as well as the various porphyry (W, Sn, Mo, Cu) deposits. The arrows show the trajectory of decompression fluids in ore deposits.

The internal mechanics of a magma chamber remains relatively simple as long as crystallinity remains low (Vigneresse et al., 1996). It pertains to a two-phase material, i.e. a solid suspension into a viscous melt. The segregation of the melt out of its source region (Rabinowicz and Vigneresse, 2004) and its ascent into veins is controlled by its intrinsic viscosity (η) and the ambient stress field (σ) (Fig. 1). Studies on magma chambers beneath volcanoes provide a reasonable description of the involved structures and processes (Cashman and Giordano, 2014; Cashman et al., 2017).

An exact description of the mechanical response of the magma chamber to ongoing crystallization is still lacking. To add more complexity, a magma chamber usually results from different episodes of melting (Fig. 1) at variable rates in the source region, i.e. discontinuous inputs of a melt of variable composition. Consequently, the physical and chemical parameters of the magma cannot be reconstructed from a continuous chemical evolution (Annen, 2009; Lee et al., 2014).

2.1.3. The magmatic volatile phase (MVP)

The exsolution of a MVP from the melt occurs during first and second boiling (Candela, 1989). First boiling takes place during magma ascent because volatiles solubility in the melt is a strong function of pressure. Its volume remains of little importance (Edmonds and Woods, 2018). By contrast, second boiling occurs during crystallization when the magmatic volatile species reach saturation and escape the melt. It occurs under constant pressure and decreasing temperature (Candela, 1989). It is the major step of MVP exsolution.

The resulting MVP can be sampled and analyzed from fluid inclusions and volcanic gases (Roedder, 1971; Giggenbach, 1987; Wallace, 2001; Bodnar et al., 2014). Its composition includes H_2O, CO_2, H_2S/H_2SO_4, HCl, HF in decreasing order of concentration and many metals

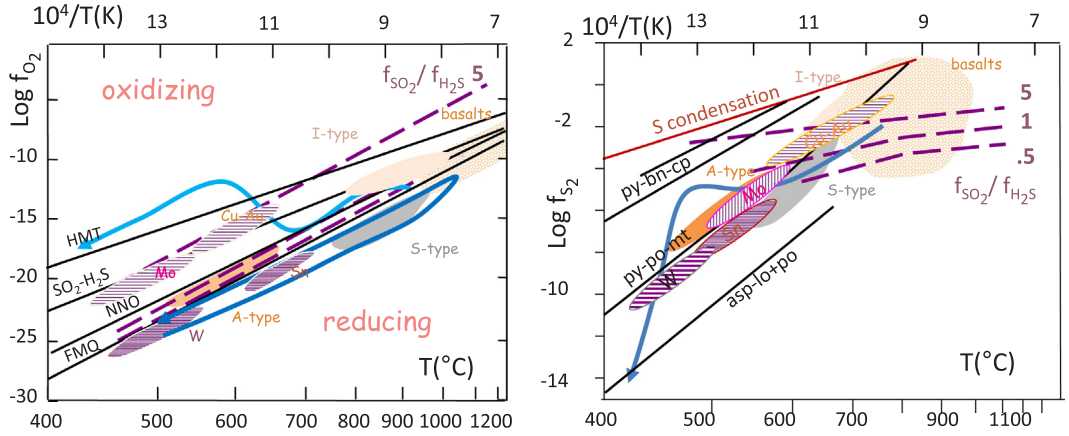

Fig. 4. Composition of the gas phase during eruptive and passive degassing on the Etna volcano from 2001 to 2007 (redrawn from Aiuppa, 2009). The eruption starts with SO_2 rich degassing, passing progressively to HCl enriched gas, whatever the eruption is active or passive. The ratio HF/HCl approximatively follows a value of 0.2 that remains all along eruption.

(Burnham, 1997; Carroll and Webster, 1994). Water can reach up to nearly 98 wt% of the MVP.

Sulphur forms a H_2S/SO_2 redox pair that buffers the magma's fO_2, dismuting at lower temperature, favoring SO_2 (Fig. 3). In a volcanic environment, SO_2 is the dominant component to start outgassing (Fig. 4).

Halogens (F, Cl, Br, I) are other important components of melts and MVPs. Fluorine is the most soluble (up to 10 wt%) in silicate melts (Carroll and Webster, 1994), the highest values being observed in alkaline magmas (Bailey, 1977). Fluorine generally remains in the residual melt (Edgar et al., 1996). Degassing starts with S and Cl, leaving F in the melt as shown for the Etna (Aiuppa, 2009). The ratio HF/HCl is about 0.2 all along degassing (Fig. 4). Br and I are in lower concentration in magmas. There is a ca. 2–3 orders of magnitude difference for Cl/Br and Br/I ratios between melts and MVP (Bureau et al., 2000; Kendrick et al., 2012). Owing to their large ionic radius, Br and I preferentially partition into the MVP rather than in the melt. Light and incompatible elements such as Li, Be, B are also considered as volatiles since they easily escape from the silicate melt. Noble gases and other volatiles may be considered as chemically insignificant (Wallace and Anderson, 2000).

Mechanical instabilities develop as soon as the solid phase forms a mush (> 50% crystals). Indeed, the solid phase restricts the motion of both the MVP and residual melt, yielding to a three-phase system. The MVP is still more mobile than the melt, but its motion is largely slowed by the high tortuosity of the mush. It leaves time to chemical instabilities to develop, giving more time for metals to diffuse from the melt into the MVP.

2.1.4. The explosive stage

When the system mechanically locks due to advanced melt crystallization, the ultimate possibility for the MVP is to escape the magma chamber by fracturing its mush (Fig. 1). It corresponds to what is observed during explosive volcanic eruptions. The corresponding three-phase system shows a highly non linear rheology, with two non-Newtonian contrasting behaviors. Shear thinning, i.e. viscosity decrease with increasing strain rate, results from crystal size reduction and shear localization. In consequence, gas bubbles segregate into weak shear bands. Conversely shear thickening, i.e. viscosity increase with strain rate, becomes dominant when the mush induces internal flow blockage due to crystal interlocking (Pistone et al., 2013). When the gas phase is fully locked, pressure builts up before explosion. Conversely, when the gas phase is activately removed, even at low rate, the system continues to slowly crystallize.

When the MVP is strongly tapped within the magma chamber or when the MVP has no more strength to overcome rock hydraulic fracturing, crystallization develops unidirectional solidification textures (UST) (Shannon et al., 1982). UST show rhythmic textures, either parallel or contorted, reflecting periods of fluctuating volatile overpressure. UST develop as crenulate layers with euhedral, dendritic or branching crystals (plumose feldspars) or intergrowths of quartz and alkali-feldspars layers. Such structures indicate the preferential mineral growth in one direction from a solid substrate, also known as comb-like crystals. UST are often associated with late dykes and aplites rich in volatiles (Breiter, 2002; Jargalan and Fujimaki, 2003). Commonly, they show quartz and feldspar precipitation, indicating fast diffusive elements such as F, Li and P (Gardien et al., 2016). Minor commonly zoned fluorite, sulfide, and REE oxides are also observed (Hönig et al., 2010). Crystal zoning in plagioclases and alkali-feldspars, as alternate repetition of mineral layers (Hönig et al., 2010) could be explained by oscillatory crystallization close to eutectic composition where element saturation repeatedly occurs (Bogoch et al., 1997). Their composition, rich in Rb, Cs, Sn, Zn, attests the presence of an abundant MVP rich in halogens (Breiter, 2002). Such structures are common in Mo- or Sn-bearing porphyry deposits. The violent release of the MVP is attested by brecciation (Landtwing et al., 2002) characteristic of high strain rates (γ°) and metals precipitation (Landtwing et al., 2010), (Fig. 1). They result in violent expulsions of large blocks of solidified magma, as well as a generalized fragmentation of the volcanic edifice into smaller pieces (Alidibirov and Dingwell, 1996; Papale, 1999).

Series of localized pulses of magmatic and hydrothermal activity are associated with this stage of high strain rate. In the Cu-Mo-Au deposit of Agua Rica, Argentina, a polystage brecciation is associated with a high sulfidation epithermal event. It is followed by phreatomagmatic diatremes, and a final stage of metal enrichment (Landtwing et al., 2002). The process repeats several times, as indicated by the multiple stocks observed, e.g. 1–2 at Henderson, Colorado (Carten et al., 1988), 6 at Zaldivar-La Escondida (Padilla-Garza et al., 2004), and 4 in the Indio Muerto District, El Salvador, Chile (Gustafson et al., 2001). They may be separated by a few 10 to 100 kyr, as in the Yerington batholith, Nevada (Schöpa et al., 2018).

2.1.5. The alteration stage

The final fate of the MVP is to induce the large alteration pattern that develops within and around an intrusion. The very first stage of alteration that characterizes porphyry deposits is an extensive mineralization with K-silicate assemblages of alkali feldspar-biotite-anhydrite-chalcopyrite-bornite or chalcopyrite-pyrite (Aranacibia and Clark, 1966; Gustafson and Hunt, 1975; Dilles and Einaudi, 1992; Williamson et al., 2016). With alteration, stable isotopes fractionate as shown by their respective δD and $\delta^{18}O$ values. The latter decreases and finally takes over $\delta^{18}O$, indicating the incorporation of more meteoric water

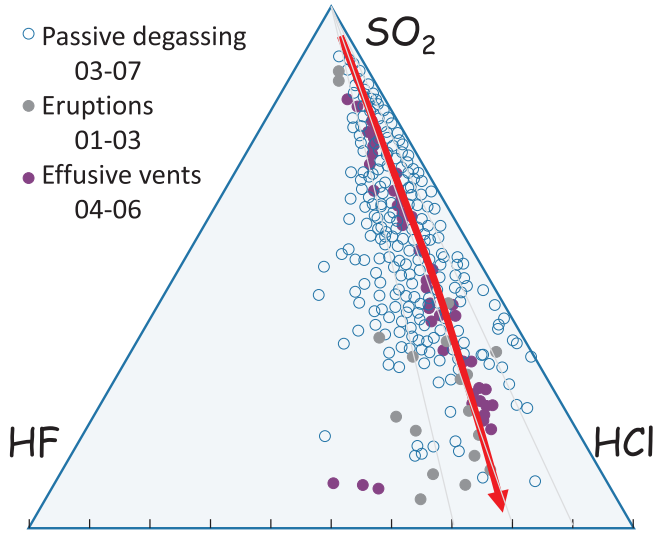

Fig. 5. Oxygen ($\delta^{18}O$) and hydrogen (δD) isotopes differentiating magmatic from meteoritic sources. Also indicated the fields for I-, A- and S-type granites, basalts, and metamorphic rocks. The successive alteration zones porphyry deposits (magmatic, potassic, phyllic, propylitic and argilic) indicate the progressive mixing of meteoritic into magmatic waters. Those are indicated by lines for meteoritic waters and the field of kaolinite, indicating oxidizing alteration.

(Fig. 5) (Taylor, 1974).

The alteration stage, although it does not strictly participate to the magma chamber evolution, is important since it is the place of metals precipitation from the hydrothermal fluids. Because it represents the best indicator of the underlying ore (Williamson et al., 2016; Ripley and Li, 2018), it constitutes an interesting tool for exploration (Vigneresse, 2019).

2.1.6. Consequences on magma chamber evolution

The initial stages of the magma chamber evolution, as ascent and emplacement, are mostly controlled by physical processes (temperature, buoyancy, strain). They consist of a two-phase system, i.e. viscous melt and either a gas or a solid phase.

The magma chamber is the place of chemical processes like elements diffusion and partitioning. Successive discontinuous inputs disturb a single continuous chemical and physical evolution, implying instabilities. Physical instabilities are mostly linked with the brutal change in temperature brought by a new hotter magma input. However, the effects are limited by the enthalpy effect that rapidly consumes the heat excess. In addition, the volume of the new magma input remains much smaller by at least one order of magnitude, so its spatial effects are restricted, whereas its time scale remains restricted (Bachmann and Bergantz, 2006).

A gas sparging model has been proposed, that examines the microphysics during rejuvenation of a mush (Parmigiani et al., 2014). The model fails to estimate how much enthalpy is consumed ahead of the melting front, but supports the idea of a thermomechanical reactivation of the mush. It also confirms the dominant effect of the latent heat in buffering the mush motion (Huber et al., 2009). Conversely, the supercriticality of the MVP intrinsically implies highly non-linear behaviour (Norton and Dutrow, 2001), having effects on the solubilities of metals into the MVP.

2.2. Physico-chemical preliminaries to a model for metals concentration

Field observations, coupled with geochronology and geochemistry document physico-chemical interactions between melts, solids and fluids during the magmatic stage. Basically, the concentration of metals occurs by transfer and transport from the melt to the MVP. Consequently, metals transport is ruled by the competition between their diffusion (into the melt and from the melt towards the MVP) and their advection (by the melt and the MVP).

2.2.1. The silicate melt

The melt is commonly described chemically, distinguishing between S-type and I-type granites (Chappell and White, 1977, 2001) to which is added the A-type (Eby, 1992). It basically separates oxidized and reduced granites, as well as alkaline rocks (Fig. 3).

The structure of silicate melts is dominated by groups of SiO_4 tetrahedra (T). Other cations perturb these structures by either building new bonds between silica tetrahedral (T) or by breaking them. Most cations act as network modifiers (Hudon and Baker, 2002). Adding metal oxides strongly contributes to form non-bridging oxygens (NBO) (Mysen, 1988).

The relative proportion of NBO/T determines the degree of polymerisation of the melt (Mysen, 1988). Indeed, when NBO/T = 0, the melt is entirely polymerised and higher values (up to 2) correspond to the gradually more depolymerised structure. Granitoids present NBO/T values ranging 0.198 for S-type and 0.22 for I-type granites, whereas A-type granites range 0.10–0.27. It has consequences on their viscosity since values of NBO/T varying from 2.0 to 0.1 correlate with a viscosity increase by 5 orders of magnitude (Mysen, 1988).

Magma rheology describes the relation between strain (γ) and shear stress (τ). When time is considered, then strain rate (γ°) develops in response to stress. For partially molten rocks (PMR), the magma rheology should take into consideration: 1) the amount of the solid phase (Φ) and/or gas phase (β); 2) the intrinsic viscosity η_s, η_m and η_g of each phase (solid, melt and gas respectively); 3) the strain rate (γ°). Changing the relative contents of the three phases alters the rheology of the whole material. Owing to its inherent large range, the strain response to stress usually plots in a log-log diagram. Considering the time dependent effects, i.e. the strain rate, rather than strain is preponderant to examine instabilities.

Structures observed in PMR and strain partitioning between phases contradict the assumption of a homogeneous response and rule out any description of a PMR by any averaging or effective property. Subsequently, 3D ($\Phi - \eta - \gamma^{\circ}$) or ($\Phi - \tau - \gamma^{\circ}$) diagrams (Vigneresse, 2008) yielded new insights onto the rheology of PMR, by showing evidence for two thresholds bracketing a specific domain in which instabilities develop (Vigneresse et al., 1996). Such instabilities were attributed to the non-linear distribution of the phases and the rheological contrast between them (Burg and Vigneresse, 2002). Adding a third gaseous phase does not simplify the problem since gas bubbles deform much more easily than the melt and its solid network. The rheology of such a multiphase material has recently been reviewed and commented for instability developments in intrusions (Vigneresse, 2015). Here only a brief summary is provided in Appendix A.

As a summary of the rheology of three-phase materials, a diagram can be constructed that takes into account the above results. It has been slightly modified from Fig. 4 of Vigneresse (2015) to explicit the role of the mush. The selected coordinates are the inverse of the effective viscosity for the magma (η) (i.e. with its three phases) and the solid phase content (Φ). The system is quite hybrid in that it incorporates the effect of the MVP into the melt. This represents an approximation of less than 10% in volume. The choice of the inverse of the effective viscosity, or the logarithmic value of the viscosity changed of sign ($-\log_{10} \eta_{eff}$), allows plotting the viscosity of the melt, independently of the strain rate and the corresponding viscosity of the solid phase, or matrix, according to the strain rate. It is computed from the power law (Eq. (2) in appendix), as the effective, or instaneous viscosity of the solid phase, according to the strain rate. It varies from about 10^{10} Pa.s under a strain rate of $10^{-4}\,s^{-1}$ to about 10^{16} Pa.s for a strain rate of $10^{-12}\,s^{-1}$ (Fig. 6). Experimental values incorporating melt and gas (Caricchi et al., 2012; Pistone et al., 2013) are also plotted on this diagram.

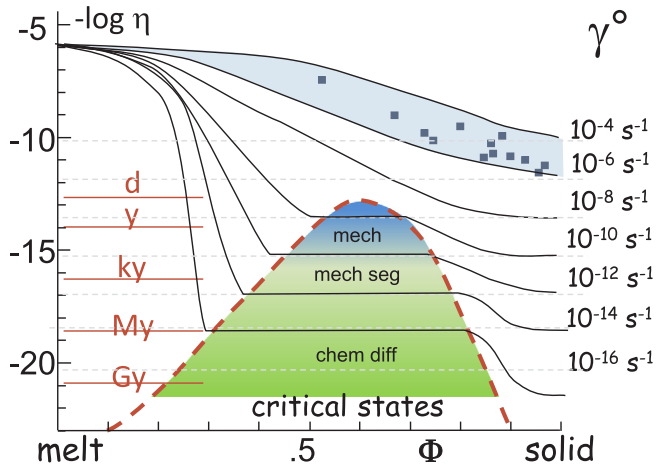

Fig. 6. The inverse of viscosity plotted in a logarithmic scale as a function of the melt percentage (Φ) of a partially molten rock, from the melt to the matrix. All curves are redrawn from a previous diagram (Vigneresse, 2015) but they incorporate the notion of a mush and individualize instabilities. Experimental values (Rutter and Neumann, 1995; Champallier et al., 2008) are reported as black squares and grey field respectively. The curves of equal ambient shear strain rate (γ°) are drawn according to laboratory experiments (about $10^{-4.5}\,s^{-1}$) to bulk geological scale ($10^{-16}\,s^{-1}$). The corresponding estimated time for duration of the process are scaled from day to Gyr. The value of $10^{-11}\,s^{-1}$ corresponds to the high strain rate estimated for granite emplacement (Mamtani, 2010). The curves go through a zone of critical states in which instabilities develop, first mechanical (mech), progressively overcome by chemical differentiation (chem diff). In between, the strain rate leading to melt segregation through fluid sparging, i.e. mechanical/chemical processes is indicated.

Unfortunately, the high strain rates used for experiments do not consider instabilities that develop at much lower strain rates. A critical region in which instabilities develop appears under strain rates lower than $10^{-10}\,s^{-1}$. This occurs for a viscosity contrast larger than 10^{10} between the melt and the solid phase (Fig. 6). The limiting value of $10^{-11}\,s^{-1}$ corresponds to the high strain rate estimated for granite emplacement (Mamtani, 2012).

2.2.2. *The fate of metals*

Common metals are initially within the melt in minor proportions. They can partition into the MVP ruled quantitatively by $K^{mvp/melt}$, or into the minerals cristallized from the melt ruled by the $K^{mineral/melt}$ value).

Metals incorporation into crystallized minerals is function of their ability to enter a crystalline lattice (Blundy and Wood, 2003). Such values are commonly experimentally measured, or theoretically predicted either from crystallography and elastic energy of the crystal network (Nagasawa, 1966; Blundy and Wood, 2003) or from thermodynamics (Vigneresse, 2007). However, once they have integrated a crystalline network, elements become inert during the life time of a magma chamber.

Metals may also partition from the melt toward the MVPThe segregation of metals within the MVP is documented by numerous experimental and field mesaurements. In particular, fluid inclusions rich in metals documents temperatures above 600 °C, and high temperature volcanic fumaroles have proven metal enrichment up to several orders of magnitude relative to solidified lavas. Metals partitioning toward the MVP is a matter of equilibrium in chemical potential between the phases.

Metals are considered as bases with chemically hard metals, such as Sn and W and chemically soft metals as Cu, Au or Ag (Vigneresse, 2012). The components added to the MVP make it more attractive to different bases. Halogen-bearing fluids mostly attract Sn in the Erzgebirge, Germany or in Southeast Asia (Breiter et al., 1999; Schwartz et al., 1995; Romer and Kroner, 2018). Conversely, S-bearing MVP attracts soft chemical metals such as Cu, Au and Ag as observed in most porphyry deposits in Chile or along the Pacific coast, e.g. El Teniente or Bajo de la Alumbrera (Cannell et al., 2005; Harris et al., 2005) or Mo for instance in the Mole granite (Cauzid et al., 2007).

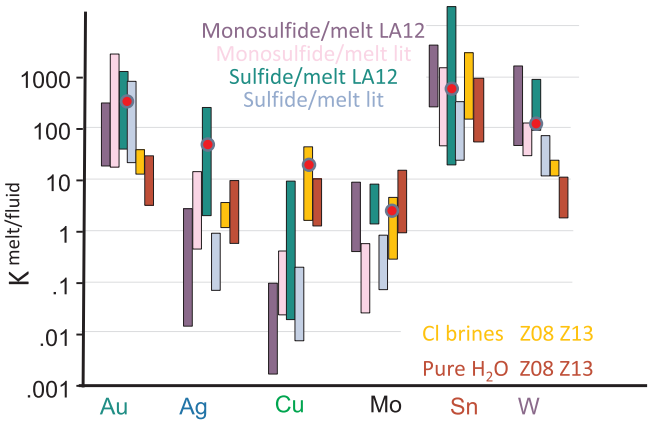

Fig. 7. Compilation of partition coefficients between melt and MVP for metals (Cu, Mo, W, Sn, Au, Ag) involved in porphyry-type deposits. Data are selected from the literature, and from specific papers (Zajacz et al., 2008; 2013 as Z08, Z13; Li and Audétat, 2012 as LA12). The dots indicate the selected values for computation.

For the MVP, partition coefficient values are measured from fluid inclusions, either directly from the field or in synthetic experiments (Heinrich et al., 1999; Ulrich et al., 1999; Audétat and Pettke, 2003; Rusk et al., 2004; Zajacz et al., 2008; Seo et al., 2009; Campos et al., 2009) (Fig. 7). Partitioning of metal from the melt into the MVP is described as a dynamical process controlled by numerous parameters. They include melt composition, through the aluminium silica index, the degree of polymerization of the melt as NBO/T, its redox condition and temperature. In addition, the components of the MVP (Cl, F, and S) have also effects on the attractivity of the MVP for metals.

A tentative summary of such partitioning is presented in unscaled diagrams (Fig. 8) considering different metals (Cu, Mo, W, Sn, Au and Ag) and corresponding conditions of the MVP (Keppler and Wyllie, 1991; Migdisov and Williams-Jones, 2013; Linnen et al., 1995, 1996; Zajacz et al., 2008; Li and Audétat, 2012; Zajacz, 2015). The diagrams ares unscaled since the various experiments summarized have been carried out under different conditions precluding direct comparison. The variations in partitioning commonly spread one order of magnitude for a given composition of the MVP (Fig. 7). When considering all ambient conditions, the variation can reach about 4 orders of magnitude (e.g. for Mo, or W (Fig. 7).

The partition coefficient directly relates to the difference in chemical potential before equilibrium between melt and MVP that may be approached by usual chemical descriptors (cf Appendix B). Since chemical descriptors commonly scale in eV, the equivalence is 1 eV = 96.49 kJ/mole to fit usual scaling in geochemistry.

Electronegativity, or chemical potential changed of sign (Pearson, 1963) ranges about 6.9–8.3 eV for the fluid phase, depending on the water content (χ = 7.5 eV). Addition of CO_2, by about 10% the H_2O volume content (Burnham, 1997), reduces this value at about 7.37 eV (Fig. 9a). A simulation of a composite MVP has been realized, adding halogens and sulfide or sulfate (Fig. 9a.). Adding Cl and F increases its electronegativity, whereas S, sulfide (6.4 eV) or sulfate (7.2 eV), reduces it (Vigneresse et al., 2014). The changes are buffered by the large relative amount of H_2O. By comparison the melt indicates values ranging 6.0–7.0 eV, with quartz presenting the highest electronegativity (7.12 eV). Metals show electronegativity as a function of their valency with values 12–18 eV for Me^{+}, 16–32 eV for Me^{2+}, and 28–49 eV for Me^{3+} (Pearson, 1988). For copper, several compounds, oxides, sulfides,

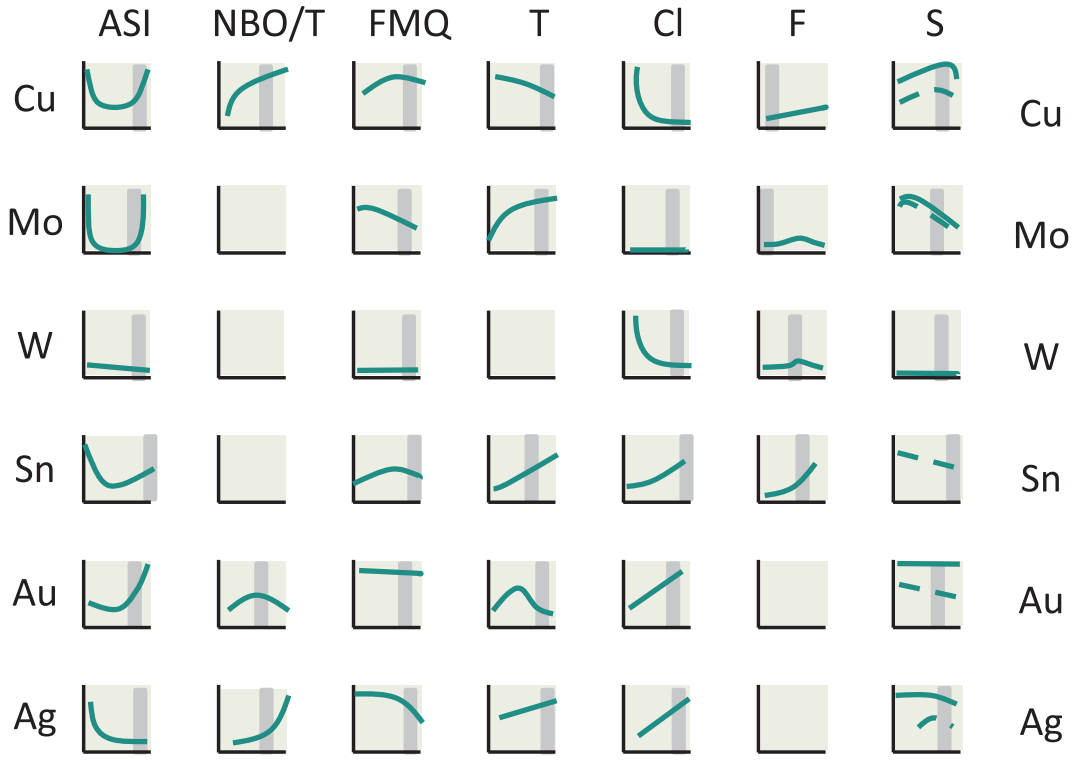

Fig. 8. Non-scaled variations of partition coefficients between melt and MVP for metals, function of the magma (aluminium silica index, polymerization, redox, temperature, content in halogens (Cl and F) and undifferentiated S species. Data are from the literature (Keppler and Wyllie, 1991; Linnen et al., 1995, 1996; Zajacz et al., 2008, 2013; Li and Audétat, 2012; Migdisov and Williams-Jones, 2013). In case of no data, the diagram is empty. The estimated field of dioritic to granitic magmas is also shown.

sulfites or sulfates, with Cu^{+} and Cu^{2+}, as well as oxides and sulfides of Mo^{4+} and Mo^{6+} (Vigneresse et al., 2014) have also been tested (Fig. 9b). They show quasi equivalent chemical gradient with the MVP or the silicate melt. But $CuCl_2$ has the closest chemical potential with Cl. Bonding with ligands (Cl, S) reduces the difference, making them more compatible within the MVP. Considering common metals, the gradient in chemical potential increases, it makes high valency metals less compatible with the MVP. Other volatile elements such as Li^{+} (5.39 eV), Be^{2+} (9.3 eV) and B^{3+} (8.3 eV) present low electronegativity values according to their charge. Such values are close to that of the MVP, making them being considered as volatile elements. Chemical hardness implies that harder fluid components, with halogens and few S, attract more specifically Sn and W (Vigneresse, 2006). A 3D diagram showing the variation in energy (dE) computed (see Appendix B) from Eq. B (5), indicates the position of a MVP, with SO_3 added, with respect to other Cu salts (Fig. 10). The energy change defines a valley, the bottom of which is indicated by a dashed line, corresponds to nul energy exchange. Close to, but on the uphill side, with lower hardness

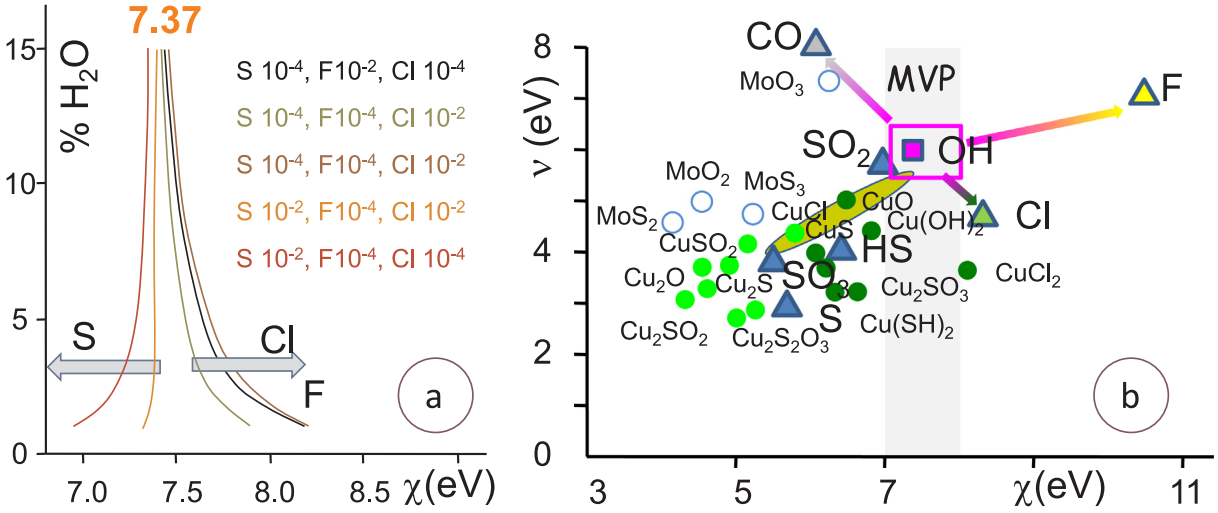

Fig. 9. Major chemical descriptors of the MVP as components (Cl, F or sulfides/sulfates) are added. The descriptors are the electronegativity (χ), i.e. the chemical potential changed of sign, and hardness (ν), its derivative with respect to a charge change. Chemical reactions evolve according to a principle of maximum hardness. The MVP evolution, mainly H_2O, is indicated in a box, with its ampliation in the diagram (a). Arrows indicate the trend when CO, F, Cl and S are added to the MVP. Metals oxides and S-compounds are represented with blue open circles (Mo) and green for Cu^{+} and Cu^{2+} (darker plain circles). The zone of silicate melts is also indicated. (For interpretation of the references to colour in this figure legend, the reader is referred to the web version of this article.)

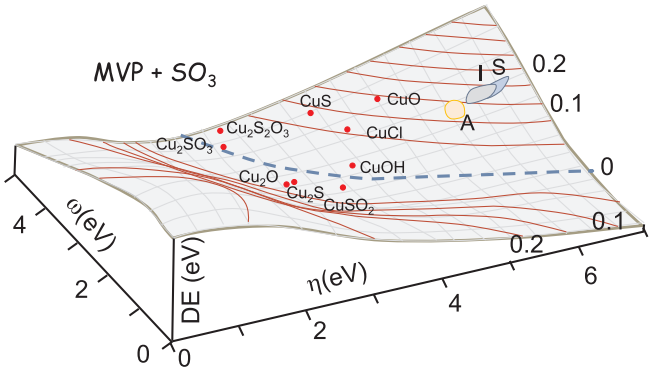

Fig. 10. 3D view of the energy exchange (dE) for a MVP with SO_3 added with spatial coordinates the chemical descriptors (ω and ν). The bottom of the valley is indicated by a dashed line. Surface with isolines of energy exchange are indicated as level lines on the topography. The valley defines two surfaces uphill, the one on the left, i.e. with smaller hardness (ν) is the preferential place for elements to joint the MVP, according to a reaction toward maximum hardness. Conversely, the opposite surface uphill is the place where the melt, represented by sectors with granites (A-, I-and S-type) are plotted. The lower energy required, the positive values of partition coefficients on the uphill side qualitatively demonstrate the role of chemical descriptors in determining the elements able to joint the MVP rather than the melt.

values, Cu salts are posted, susceptible to enter the MVP. They have a not too different chemical potential, and are on the good side, i.e. according to the maximum hardness principle, and having partition coefficient larger than unit (see Appendix B). They may easily enter the MVP.

2.2.3. Elements diffusion

Diffusion is the capacity of a system to re-equilibrate a chemical gradient. This commonly occurs without any bulk motion of the surrounding material, which would be considered as advection. The elements motion is always from the highest to the lowest, e.g. the hot toward the cold, or concentrate toward dilute. It can be a thermal re-equilibration between a cold and a warmer region. In rocks the thermal diffusivity is nearly constant, at about 10^{-6} m^2/s (Fig. 11). Material bulk motion may be considered as the diffusion of a momentum, the product of mass and velocity of this object. However, the diffusive process depends on the ambient material. In a solid, self-diffusion occurs by atoms motion when the chemical potential is constant everywhere (Lesher, 2010). Diffusion and viscosity are intimately linked through the Stokes-Einstein relationship that considers self-diffusion in a viscous medium. It corresponds to the drag force applied on the gas

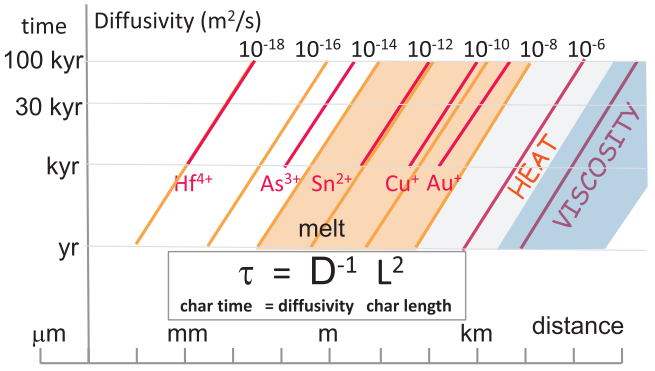

Fig. 11. Changes of the characteristic diffusion length in a granitic magma chamber in a fully molten state. The considered elements (heat and melt) and metals (Au, Cu, Sn, As, Hf) are placed as a fuction of their diffusivity. The coordinates are scaled in length from mm to km, whereas the time scales as from yr to 100 kyr, the life time of a magma chamber.

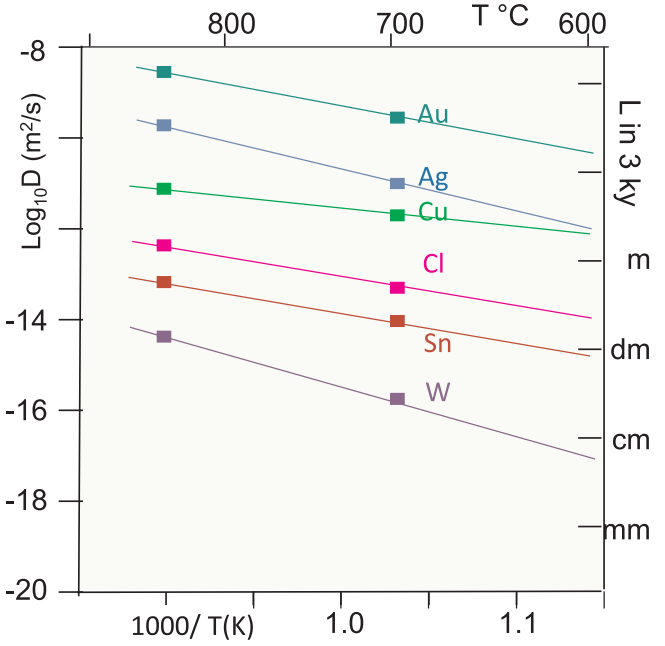

Fig. 12. Metals diffusivity in silicate melts at temperatures 900–600 °C. Data are selected from Jambon (1982), Zhang et al., (2010) and Lesher (2010). The slope of the curves is function of the activation energy.

bubble by the viscous melt (Mungall, 2002).

The quantitative and time aspects of diffusion are ruled by the Fick's laws according to the gradient of concentration in the system. The quantity that relates the flux to the concentration gradient is the diffusivity coefficient (D_i) (Fig. 11). In solids, diffusivities are low, below 10^{-18} m^2/s. In viscous melts, metal diffusivity values range 10^{-11} to 10^{-16} m^2/s (Zhang et al., 2010). Conversely in gases, metal diffusivity is about 10^{-5} m^2/s (Zhang, 2010).

Values for metal diffusivity have been selected from the literature (Jambon, 1982; Von der Gönna and Rüssell, 2000; Benne and Rüssell, 2005; Kaufmann and Rüssell, 2010; Zhang et al., 2010). They plot as a function of temperature in the range 600–900 °C. They show a quite parallel trend in that range of temperature, but 6 orders of magnitude separate Au^+ from W^{4+}, the slowest (Fig. 12). As it occurs for viscosity, diffusivity values also vary with the nature and structure of the silicate melt, i.e. with their polymeric structure. Such values have been estimated from various felsic and mafic melts, at temperatures ranging 600–900 °C, depending on the melt composition. The linear nature of the Arrhenius law can thus be interpolated, resulting in the temperature range corresponding to a crystallizing magma chamber (Fig. 12). Metal diffusivity depends on the ionic radius of elements and on the respective valence of ions, but the activation energy ranges 100–200 kJ/mole (Jambon, 1982). The higher the activation energy, the more dependent on temperature is the property. In a mush, the solid crystalline framework develops tortuosity (Boudreau, 1996) slowing down the residual melt motion.

2.3. MVP motion

In a viscous melt free of crystals, the ascent velocity is controlled by Stokes ascent velocity. It basically depends on the shear rate (Bagdassarov et al., 1994). The velocity ascent (Ug) of a gas bubble results from a competition between the density difference (Δρ) and the melt viscosity (μ). A bubble of radius 1 mm presents an ascent velocity of about 1 m/s in a melt of viscosity 10^6 Pa.s.

The shape of a rising bubble in a fluid is an oblate ellipsoid with the short axis close to the direction of the tangential velocity of the bubble along its path. However, the ascending bubble induces a wake behind

it, consisting in two threads with vorticity of opposite sign (Shew et al., 2006). The amplitude of the wake depends on the size of the bubble, being quite smaller, in relation with the Reynolds number. It determines the instability development during the bubble path. For very small bubbles, the path is rectilinear. Instability development may lead to a spiraling, or helical path (de Vries et al., 2002) as observed on the field (Vigneresse, 2015).

The case of a mush profoundly differs from a crystal-free viscous fluid. For highly crystalline mush ($\Phi > 0.5$) the solid phase dominates magma rheology. Crystals form a loose framework in which the melt is still able to flow in the interstitial spaces, but its motion is hampered by tortuosity (Zalc et al., 2004). The gaseous phase can be considered as a minor phase. At very high crystallinity values ($\Phi > 0.75$) the quasi locked framework of crystals strongly reduces the motion of the solid network (Vigneresse et al., 1996). The motion of melt and the gas through a tortuous porosity drastically changes in character. Analytical modelling through the equations of fluid motion and of mass conservation (Eulerian description) is no more adapted to account for such conditions. Indeed, numerous instabilities develop due to non-linear interactions betwwen phases in presence. Many specific textures develop within the crystallizing melt (Žák et al., 2007; Clarke et al., 2013; Vigneresse, 2015).

2.4. Lifetime of an intrusion

The time scale during which ore deposits are generated links to the multiple ore centers observed in the field. Each has its own life, i.e. with specific enrichment in one metal, its own chemical aspect, i.e. specific MVP composition, and probably a specific magma composition, i.e. depending of the mixture between new magma inputs. All those observations link with the duration of the evolving magma chamber.

Determining the exact time and duration of an igneous intrusion is hampered by the lack of precise dating, due to the successive magma inputs. Observation and age dating of the successive ore bodies indicate a generally longer process for porphyry-type intrusions compared to barren granites. It may reflect a longer lasting process due to the hydrothermal circulation.

Detailed chronology of the magmatic-hydrothermal system at El Teniente, Chile suggests a long-lived event lasting nearly 1.0 My (Maksaev et al., 2004; Cannell et al., 2005). More detailed analyses indicate that El Teniente could have formed over a period of 0.9 My, between 5.28 ± 0.10 and 4.37 ± 0.12 Ma (Klemm et al., 2007). Longer intrusive periods have been reported with 3 major sequences in the Yerington batholiths, Nevada along 1 Myr (Schöpa et al., 2018) or even 4 episodes along 5 Myr in the Qulong batholiths, Tibet (Li et al., 2018). Such long lasting events remain difficult to bracket, owing to the generally large uncertainties on different geochronological methods (Chiaradia et al., 2013; Mercer et al., 2015). A compilation based on 24 Cu- and Cu-Mo porphyry deposits shows that duration of ore genesis ranges 0.2–4.1 My (Fig. 13). Considering the possibility of multiple ore bodies would certainly reduce the time span of each of them. It suggests that ore generation during magmatic episodes lasts longer than the time estimates of barren granitic emplacement or volcanic activity.

The time span for barren granitic intrusions may be constrained from several methods (Crisp, 1984; Petford et al., 2000; White et al., 2006), but they are hardly comparable. Precise zircon ages on a single intrusion are still scarce. The Tuolumne batholith, Sierra Nevada, CA, (Paterson et al., 2011), consider the different mineral facies of the batholiths, with their adjacent lobes (Memeti et al., 2010). Thermal modelling of the cooling of an intrusion (Yoshinobu et al., 1998; Annen, 2009) constrains the boundaries between mineral facies. The development of the seven recognized different mineral facies span in total between 94.6 and 85.1 Ma, providing a median duration age of 1.1 My. According to the time for a facies to fully crystallize before the next intrusion, as shown by the sharp contact between them, would restrict the time life of a pluton to some several hundreds of thousand years

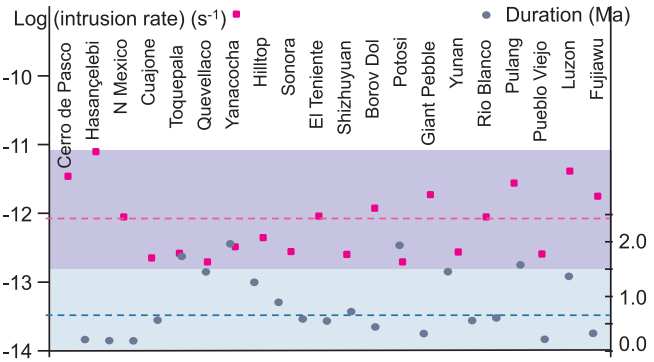

Fig. 13. Estimated rates of ore bodies emplacement (squares) and duration (circles) expressed as a rate, according to an estimate strain ($\gamma = 1$). The different porphyry bodies are: Cerro de Pasco, Peru (Baumgartner et al., 2009; Bissig et al., 2003); El Teniente, Chile(Spencer et al., 2015), Hasançelebi, Turkey (Kuþcu et al., 2011); Northern Mexico (Barra et al., 2005); Southern Peru (Simmons et al., 2013);Yanacocha, Peru (Longo et al., 2010); Nevada (Kelson et al., 2008); Sonora, Mexico (Valencia et al., 2008); El Teniente, Chile (Klemm et al., 2007; Cannell et al., 2005); Shizhuyuan (Lu et al., 2003); Borov Dol (Lehmann et al., 2013); Potosi (Rice et al., 2005); Giant Pebble Alaska (Lang et al., 2013); Yunan (Wenchang et al., 2011; Lu et al., 2013); Rio Blanco, Chile (Deckart et al., 2005); Pulang (Wenchang et al., 2011); Luzon (Hollings et al., 2011); Pueblo Viejo, Dominican Republic (Kirk et al., 2014); Fujiawu (Li et al., 2013).

(Yoshinobu et al., 1998).

To allow a comparison with the other processes involved, the duration of the magmatic events should be transcribed to rates (i.e. from yr to s^{-1}). This can be effectively estimated, assuming a strain of $\gamma = 1$ during intrusion (Fig. 13). Comparison between existing data remains difficult. The used units are often a rate of volume intrusion per time unit. But such volume estimates are based on an equivalent sphere (Bellon et al., 1974; Pelletier, 1999), an estimated volume (Petford et al., 2000) or even tonnage (Sinclair, 2007). The the volume is compared to a given time unit, in year units or even seconds. The magma input rates are of the order of 1 m^3/s (Petford et al., 2000) to 400 km^3/My (Paterson et al., 2011), i.e. a rate ranging over 3 orders of magnitude. An average value for the duration of a single intrusion is less than 100 ky (Petford et al., 2000; Schoene et al., 2012). It corroborates volume rates estimates (Crisp, 1984) and data collected to infer self-similarity between magmatism and volcanism (Pelletier, 1999). Simulations on magma chambers associated with volcanoes indicate an even higher magma input rates (0.01 km^3/yr, i.e 0.3 m^3/s) for short-lived magma reservoirs that would erupt rapidly after being recharged (Menand et al., 2015). Volcanic magma chambers display an evolution time, ranging 0.008–0.1 km^3/yr (Zellmer et al., 2005). Such rates of volume intrusion ranging 0.01–1 m^3/s, correspond to a rate of displacement over 1 km of 10^{-12}–10^{--10} s^{-1}, assuming a strain of $\gamma = 1$. The difference by about one order of magnitude between porphyry and barren intrusions (Fig. 13) appears significant, whatever the uncertainty would be on the specific datations (Chiaradia, 2014).

3. Building a quantitative model for metals concentration

Because metals segregation takes place within the melt and the MVP, ore generation may be reformulated as a competition between metal diffusion toward the MVP, followed by its transport in the MVP, i.e. advection. The viscosity of the MVP is at least 6 orders of magnitude lower than that of the melt. Thus ore generation even simplifies into a competition between advection and diffusion in the melt. Such a situation is common in physics of heat and mass transfer. It is determined for each element by a dimensionless number, the Péclet number (Pe), ratio of the rate of advection to the rate of diffusion (Bergman et al., 2011). Nevertheless, the process must be qualitatively and

quantitatively described. In the first case a Lagrangian approach takes into account the microphysics or melt-MVP interactions, whereas an Eulerian approach quantifies the proceses.

The suggested formalism is adapted from the model of gas sparging in a mush (Huber et al., 2012). The choice of a mush, with crystallinity > 50% is necessary for two reasons. Firstly, a significant amount of MVP must be present, i.e. implying second boiling. Secondly, the high crystallinity implies large tortuosity that slows down melt motion. When both prerequisites are not completed, the system turns to a barren intrusion, i.e. metals have not enough time to diffuse and stay within the solidifying melt. The mush is mechanically nearly locked, within a quasi rigid framework (Vigneresse et al., 1996). Channels of viscous melt infiltrate within the solid framework while the more mobile MVP bubbles can easily be distorted to lubricate melt motion. Metals are within this mobile material and can diffuse toward the MVP.

3.1. Qualitative approach

The system requires an Eulerian description to solve the mass and heat transfer for the melt and the MVP. But before going to hard computing, it is often recommended to use dimensionless number to characterize the type of flow, and subsequent development of instabilities (Manneville, 1991). Five numbers characterize the motion of a multiphase viscous fluid and its interactions with strain rate, temperature and geometry, namely, the Reynolds (Re), Stefan (St), Péclet (Pe), Capillary (Ca) and Bond (Bo) numbers (Fig. 14).

The Reynolds number (Re) is the ratio of inertial forces to viscous forces. Adopting η as the viscosity of the fluid, with density ρ_m, and flowing along a length L, with a shear rate of γ°, the Reynolds number is expressed as

$$Re = \rho_m \gamma^\circ L^2/\eta \quad (1)$$

The major controlling parameters are the flow velocity (i.e. the shear rate) and the characteristic length of the flow. For a low Reynolds number (Re < 5), the flow is laminar, and it becomes turbulent for high values (R > 10^4). In between the flow is intermediate, i.e. it may present local departures from a steady laminar flow. The term in $\gamma^\circ L^2$ is the flow velocity U_m (Burgisser and Bergants, 2011), allowing the use of a more sensitive parameter. Assuming the viscosity η of the melt is 10^6 Pa.s, the kinematic viscosity ($\nu = \eta/\rho$) must be considered (Huppert et al., 1986). The shear rate is of the order of 10^{-6}–10^{-10} s^{-1}, corresponding to a velocity of 0.1 cm/s for a 1 km long flow to 0.1 m/s for a flow along 0.1 km. The Reynolds number is of order 10–10^{-2}. Consequently, the melt flow is in the range between laminar to intermediate (Fig. 14), thus susceptible of local non steady state behaviours (Holmes-Cerfon and Whitehead, 2011). Reaching the turbulent state supposes increasing the shear rate (or the velocity of intrusion) by 1–2 orders of magnitude, or decreasing the viscosity by the same amount (Bergantz, 2000).

The second number or Stefan number (St) is the ratio of the sensible heat to the latent heat, indicating the heat loss through melting or cooling (Fig. 14). It has importance during magma recharge that would imply heat loss through melting. It scales as the ratio of specific heat (c) versus latent heat of fusion (L_f), the whole multiplied by the change in temperature with respect to melting temperature ($T - T_m$).

$$St = c\,(T - T_m)/L_f \quad (2)$$

When considering the involved minerals, such as quartz, plagioclase, K-feldspar and biotite, their melting enthalpy does not vary significantly, with values of 302, 302, 308 and 453 kJ/kg respectively (Spray, 1992; Navrotsky, 1995), making biotite more sensitive. The bulk magma presents a heat capacity of about 1200–1480 J/kg/K whereas the latent heat of melting ranges 300–420 kJ/kg depending on the bulk composition, the more mafic requiring more energy (Bohrson

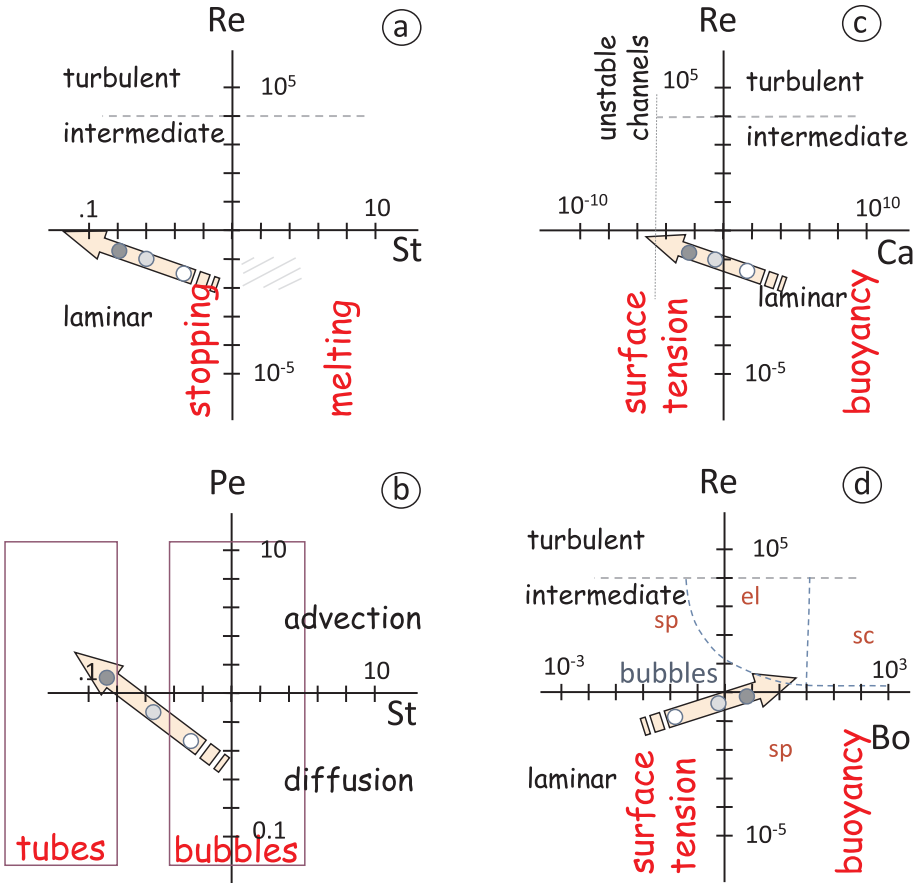

Fig. 14. Stability diagrams using non-dimensional number to identify the type of flow. The Reynolds number, ratio of inertial to viscous forces, determines the transition from laminar to turbulent flows. Conversely, the Stefan number examines the heat carried by the magma and latent heat required for fusion. It limits melt flows from stopping. The Péclet number is the ratio of advection to diffusion. The next dimensionless numbers are the Bond and Capillary numbers. The first distinguishes between spherical bubbles (sp) flow driven by surface tension or by buoyancy under the form of ellipsoids (el) and spherical caps (sc). At last the Capillary number is the ratio of the shear stress imposed by the motion to surface tension. It distinguishes flows in tubes, progressively becoming unstable, and forming isolated spherical to sigmoïdal bubbles. The respective dominant character of the flow is plotted in each field. On each diagram, the estimated values for a magma at 600 ± 50 °C (melt, MVP, solid) are computed, from open to full circles, assuming the nature of the flow, shown by an arrow.

and Spera, 2001). Thus values for the Stefan numbers require distinguishing felsic and mafic intrusions with a coefficient α depending on magma composition.

$$St = \alpha\, 10^{-3}\Delta T \quad \text{with } \alpha = \ 4.0 \text{ (felsic) or } 3.5 \text{ (mafic)} \tag{3}$$

Assuming that ΔT, the departure from the melting temperature, is of the order of 100–200 °C, then a common value of St would be 0.35–0.80. It is still less than 1.0, that would push ahead the melting front (Huber et al., 2008).

The next dimensionless number is the Péclet number (Pe), ratio of the rate of metal advection to the rate of metal diffusion, or equivalently of convection to diffusion. It requires defining the pore size (δ) and the radius of the gas bubble (R) to compute the average velocity (Ug) of the pore fluid through a magma chamber of a given height (H). The MVP and melt have a density contrast expressed as ρ_m/ρ_g. The motion of the gaseous phase must take into account bubbles deformability that basically depends on the shear rate (Bagdassarov et al., 1994). It is a competition between the density contrast and the melt viscosity (η) following the Stokes ascent velocity. In a viscous melt free of crystals, the ascent velocity is controlled by the melt viscosity and is of the order of 1 m/s for a bubble of 1 mm in diameter (Bagdassarov et al., 1994). In case of high tortuosity, the velocity slows down to 0.1 m/s (Zalc et al., 2004). On the other hand, diffusion is ruled by the metal diffusivity (D_i) and the geometry of the melt and gas bubble. Because the involved parameters present scales many orders of magnitude, e.g. from mm (bubble scale) to km (magma chamber height), it is not easy to assign an exact Péclet number (Pe_i) for each element. It seems better to scale it relative to an average diffusivity. Using an advective motion about 0.1 m/s, a pore size of 10^{-4} m, a 1 km for the height of the magma chamber, and a magma viscosity of 10^6 Pa.s, valid for porphyry-type magmas, the Pe_i values scale as

$$Pe \sim 10^{-14}/D_i \tag{4}$$

with diffusivity values in m^2/s (Fig. 12). Thus for diffusivity values higher than $10^{-13}\,m^2/s$, the associated Péclet number is small, assuming a diffusive flux. Conversely for low diffusivities, commonly below $10^{-15}\,m^2/s$, the flux is advective.

The two next numbers address the motion of a gas phase into a viscous material (Fig. 14). The capillary number Ca is the ratio of shear stresses that deform bubbles to the surface tension stresses that tend to keep bubbles spherical. It characterizes bubbles deformation under shear stress, until splitting into smaller ellipsoidal or sigmoidal smaller bubbles (Frank et al., 2006; Komrakova et al., 2014). For increasing Ca, bubbles deform to adopt a sigmoidal shape (Liu et al., 2018)

$$Ca = \eta\dot{\gamma}^{\circ}R/\Gamma \tag{5}$$

in which Γ is the surface tension, R the bubbles diameter and η the suspending fluid viscosity with density ρ. The whole is under shear rate $\dot{\gamma}^{\circ}$. For low Ca, such as at low viscosity or high shear rate, surface tension plays an important role. In case of silicate melts, in which Ca is usually < 1 bubbles may coalesce into small tubes with increasing Reynolds number, i.e. with decreasing viscosity (Fig. 14).

Another dimensionless value, the Bond number (Bo) compares the gravity forces (Δρ g) applied to a bubble of radius (R) to surface tension (Γ).

$$Bo = \Delta\rho\, g\, R^2/\Gamma \tag{6}$$

Hence assuming values for bubble diameter (R = 1 mm), surface tension Γ averages about 0.1 N/m (Mungall and Su, 2005), and viscosity μ of the magma 10^6 Pa.s, values for Ca are in the range of $10^4\,\dot{\gamma}^{\circ}$, thus resulting in Ca ≪ 1 in natural conditions, with shear rate of the order of 10^{-10} to $10^{-13}\,s^{-1}$. Capillary forces dominate in melt flowing in a magma chamber flow (L = 5 km) (Rust et al., 2003). At moderate Reynolds number, with increasing Bond number, bubbles deform, from spherical to ellipsoidal. Above a threshold for Bo values approximately 50, the bubbles adopt a spherical cap shape (Gupta and Kumar, 2008; Amaya-Bower and Lee, 2010). At higher Reynolds number (10^4) the regime becomes turbulent and bubbles split in smaller ones (Fig. 14). In a silicate melt, the Bond number is very low, in the range of 10^{-6}, indicating that surface tension dominates over buoyancy (Fig. 14).

The cross-plot of the five numbers provides a qualitative estimate of the flow type existing in a magma chamber. Using the required geometrical and physical values characterizing MVP and melt indicates that the magma flow is laminar, dominated by the amount of the viscous melt. Relative to the MVP, diffusion occurs in bubbles before being advected through tubes of connected bubbles, with a dominant role of surface tension. The different numbers have been estimated to infer a variation in temperature by about ± 50 °C during cooling around 600 °C. The resulting numbers do not point toward a drastic change in the flow regime (Fig. 14).

The respective values of these non-dimensional numbers can be compared, defining fields of stability for the flow. Hence, the Reynolds number characterizes a laminar flow versus an intermediate to turbulent flow. Whereas the magma is usually within the field of laminar flow, the introduction of bubbles increases the Reynolds number and leads to intermediate flow regime when bubbles get connected, as in pegmatites for instance. The Stefan number determines the stopping of the magma or its advance through ongoing melting. Since it links with surface tension, it is important to determine the advance of bubbles. A specific Péclet number for each metal controls the change from diffusion to advection, i.e. the change of metal transport from bubbles to tubes of connected bubbles (Fig. 14). They provide a parametric control on the motion of the bulk magma with its three components.

Once the type of flow has been identified, a Lagrangian description of the system is necessary to simulate the transport of the melt through the mush. Hence, the Eulerian description cannot efficiently describe the micro-physics acting at the bubble and pore size. The simulation requires a Lattice Boltzman Method (Aidun and Clause, 2010; Parmigiani et al., 2011). The method solves the plain Navier-Stokes equations for incompressible fluids in multiphase environments (Chopard and Droz, 1998). It also encompasses advection-diffusion, as well as thermal problems, thus allowing examining heat and/or enthalpy effects (Huber et al., 2008). These reactions affect the porous media modifying local permeability or/and phases saturation. Mass transport by flows in multiphase porous media is ruled by pressure gradients, buoyancy, viscous and capillary forces. Their internal competition determines the flow type, leading to capillary instabilities (Parmigiani et al., 2009).

The Lattice Boltzman Method examines the three-phase system by discretizing a volume into nodes, to which a given state is assigned. Each node represents one of the three phases (solid, viscous, gas) that interacts with the surrounding nodes (Fig. 15). In a 2D representation, such neigbouring nodes are 6, but 24 in a 3D model, increasing the computation time. The numerical code is an open source parallel Lattice Boltzmann solver (Palabos, 2010). The synthetic porous media matrix is represented by about 20,000 crystals with various shapes and sizes, and it is modeled on a grid with 200 × 200 × 300 lattice nodes. The mean pore radius is about 10 grid nodes. The crystalline porous matrix is built through a nucleation and growth algorithm (Hersum et al., 2005).

In a first attempt (Hersum and Marsh, 2006), the magma was represented by a basaltic melt, the size and shape of the forming minerals being constrained. The model tested a variety of kinetic models for nucleation and crystal growth especially for plagioclase and clinopyroxene. No gas phase was present. The onset of a finite yield strength is a percolation threshold for both the crystalline network (Φ > 0.78) and melt. The porous melt flow is localized into high flux channels (Hersum et al., 2005).

In a more recent attempt (Parmigiani et al., 2011), the simulation examines the behavior of the melt and gas phase within a high crystallinity mush. When bubbles nucleate, they displace the gas or the more viscous melt (Fig. 15). Three major flow regimes are commonly observed (Paterson, 1981). They are i) compact displacement (CD)

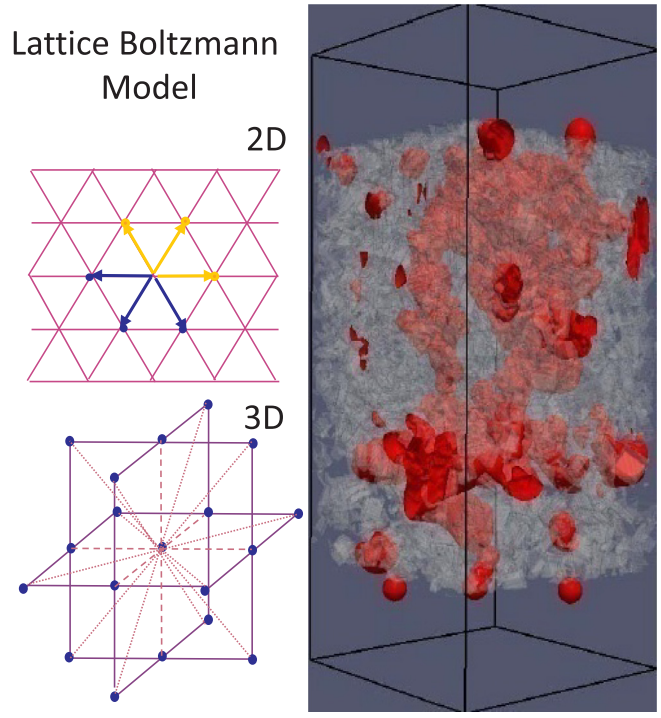

Fig. 15. Lattice Boltzman Method (LBM) for simulating gas-melt interactions in a mush. The computational schemes, in 2D along a hexagonal grid and in 3D along a cubic square grid are represented. The central node interacts with its neighbouring cells. The 3D model indicates at each node of the grid its occupation by the melt, a crystal (grey) or a gas MVP (red). The figures are adapted from simulation (Parmigiani et al., 2011). (For interpretation of the references to colour in this figure legend, the reader is referred to the web version of this article.)

(Lenormand et al., 1988); ii) capillary fingering (CF) or invasion percolation (Wilkinson and Willemsen, 1983); and iii) viscous fingering (VF). They form in horizontal planes when the gravity effects are negligible (2D situation). They also develop in vertical planes when gravity is involved (3D case). The evolution from one pattern to another is similar to a phase transition. The result is a progressive change in the system, evolving from a tapped gas phase consisting in non connected bubbles that form a lid, up to reach enough volume. When reaching a critical gas saturation (CGS), bubbles get connected, and form vertical tubes that rapidly escape from the mush (Fig. 15).

A critical gas saturation is also observed in a productive oil reservoir when the gas pressure is too low to activate oil motion implying the loss of recovering the remaining oil (Handy, 1958). The CGS is the minimum gas pressure required to establish a continuous gas flow through a porous medium. It scales as the inverse of Bond number, whereas the invasion front width scales as its inverse square (Løvoll et al., 2005). The very low value of the Bond number for a silicate-rich magma (about 10^{-6}) corresponds to a nearly constant value of the CGS close to 20%. Numerical simulations using invasion percolation methods indicate values for the CGS close to 30% (Du and Yortsos, 1999). Commonly assumed values are about 20–25% gas (Bear, 1988). Once overcoming the CGS, the gaseous phase switches from a bubbly structure to connected tubes, corresponding to an invasion percolation (Wilkinson and Willemsen, 1983; Lenormand et al., 1988). It corresponds to degassing cascades in a shear-thinning fluid (Vidal et al., 2011). Interactions between trains of bubbles and the melt lead to complex interactions between bubbles. Three regimes of bubbles ascent are identified that depend on the flux of degassing. For a low flux, bubbles are not connected, and at high flux they form open channels. A transitional state occurs between the two states. It suggests that the transition is an effect of the fluid rheology (Vidal et al., 2011). The flux of ascending bubbles is intermittent (Divoux et al., 2009).

The model allows examining the effects of the undimensional numbers that control the multiphase flow (Fig. 14). As the Péclet number increases (Fig. 16), the MVP shape changes from a more or less continuous lid to a structure dominated by vertical tubes. It also corresponds to a decrease in the Stephan number due to the heat exchange between the melt and the MVP. The small decease in Stephan number is indicative of the heat consumed through melting of the adjacent mush. It remains very limited, and does not affect the bulk process of fluid sparging. Nevertheless, the aspect ratio, defined as the equivalent radius of the tube (R) to its length (L) varies linearly with the Péclet number (Fig. 16). It thus follows the ratio of advective versus diffusive heat transport (Parmigiani et al., 2014). The variation in shape of the MVP simultaneous with the Stephan number (Fig. 17) indicates a

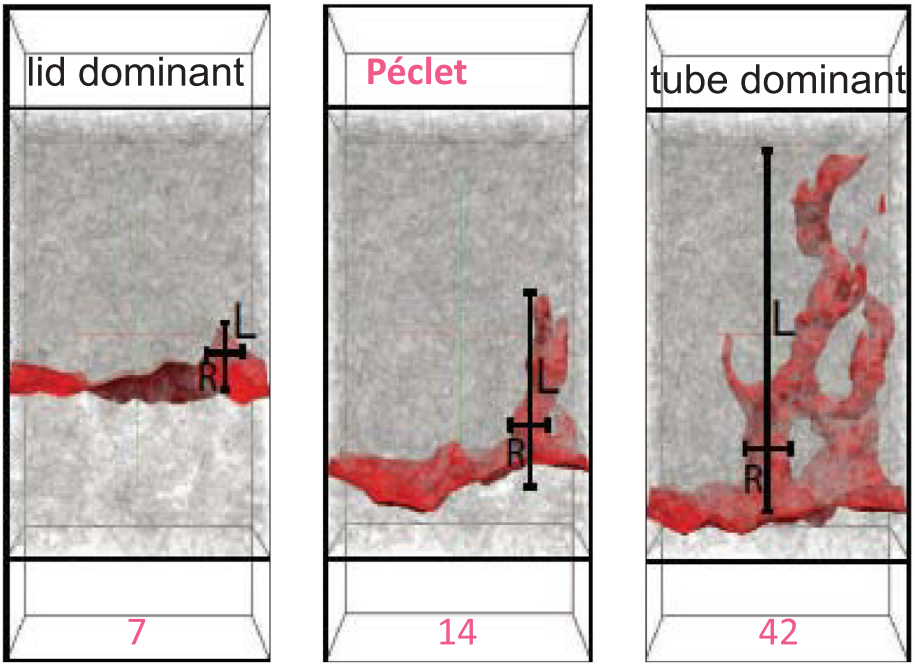

Fig. 16. Influence of Péclet number (values at the bottom of the box) in a 3D simulation on a hexagonal grid. With increasing Pe, the MVP shifts from a thin lid of thickness (L) to connected vertical tubes of height L and diameter R. It demonstrates the progressive development of advection (in tubes) versus diffusion (within the lid). The figures are adapted from the numerical simulation (Parmigiani et al., 2011).

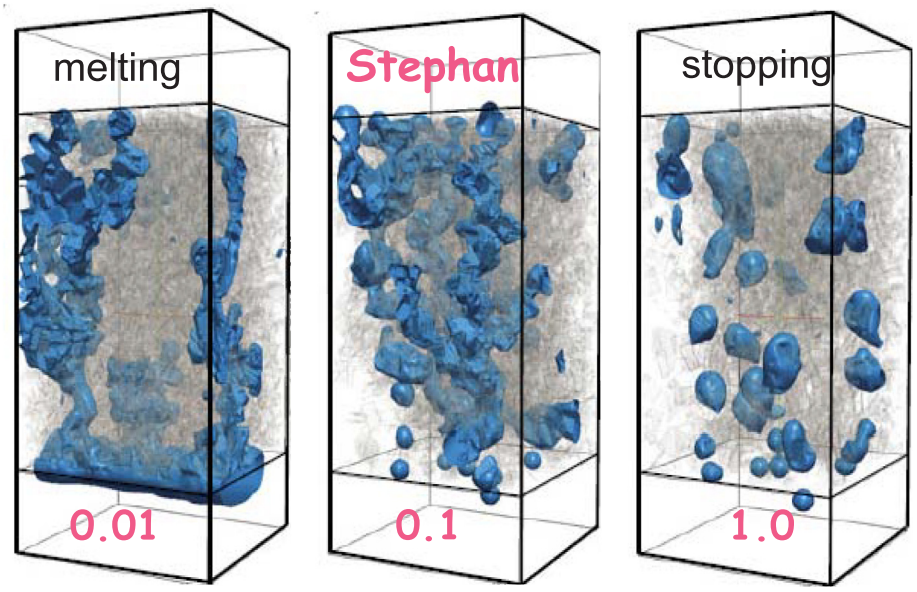

Fig. 17. Influence of Stefan number (values at the bottom of the box) on the MVP structure in a 3D simulation on a hexagonal grid. For high values of Stephan number, bubbles are individualized. In contrast, with decreasing Stephan number, i.e. with temperature decrease, bubbles coalesce forming tubes. The progression of the system (Fig. 14), as indicated in the text, is from moderate St, high Pe toward low St and higher Pe. The figures are adapted from the numerical simulation (Parmigiani et al., 2011).

progressive increase of the vertical tubes over a stopping lid, or non-connected bubbles. It is also coherent with the predictions of the diagrams implying the variations in undimensional numbers (Fig. 14). The development of a MVP lid for small Péclet numbers (Fig. 16) is coherent with the presence of a supercritical fluid, i.e. with a limited surface tension. It correlates with the variations of the capillary number and the Reynolds number (Fig. 14). But as the MVP looses surface tension because of its supercritical character, the flow becomes unstable, and switches to channels. In fact, this must be replaced in terms of stress induced by the MVP. The equivalent Bond number increases with the ongoing flow, making the buoyancy forces dominant. The structure shifts from horizontal lid to vertical tubes.

3.2. Quantitative approach

An Eulerian simulation allows computing the mass balance between the initial metal content within the melt, and its late concentration into the MVP. For each involved metal, the enrichment factor is a combination of element partitioning and the type of flux. It is easiest to compute a relative enrichment in one element by comparing elements together. Here Cl is taken as a reference (Huber et al., 2012). Hence, Cl participates to the MVP and its diffusivity ($10^{-12.5}$ m^2/s) (Zhang et al., 2010) makes its Péclet number close to the switch between advective and diffusive fluxes.

The enrichment factor $E_{Me\text{-}Cl}$ strongly depends on the value of the Péclet number for the considered metal, i.e. it depends on whether the MVP flux is advective or diffusive. The enrichment factor incorporates the diffusivities with a coefficient (c) and a power law (b) coefficient, numerically adjusted (Huber et al., 2012)

$$E_{Me-Cl} = (K_{Me}/K_{Cl})\,[1+(c\,Pe_{Cl})^b/(1 + (c\,Pe_{Me})^b] \quad (7)$$

Two situations characterize the enrichment as a function of the flux. For low Péclet numbers, saturation occurs rapidly, yielding a minimal value of this metal in the MVP. In this case, i.e. for fast diffusive elements, the minimum enrichment ($E_{Me\text{-}Cl}|_{min}$) factor is the ratio of the partition coefficients. Indeed, the diffusive process is fast enough for the two phases to reach equilibrium.

$$E_{Me-Cl}|_{min} = K_{Me}/K_{Cl} \quad (8)$$

Conversely, when the flux becomes advective and takes over a slower diffusive process, i.e; when the Péclet number for this metal becomes higher than unity, the enrichment factor follows a power law function of the Péclet number scaled as $1 + (cPe)^b$, with two coefficients (b and c) that can be numerically estimated (Huber et al., 2012). The power coefficient (b), is numerically estimated at 1.456.

For high values of both Péclet numbers ($\gg$1), the second term of the equation converges toward the ratio of the two Péclet numbers, i.e. to the ratio of diffusivity values. Thus, only the second term of the equation (i.e. the power law in Péclet number), remains with the coefficient b.

$$E_{Me-Cl}|_{max} = (K_{Me}/K_{Cl})\,(D_{Me}/D_{Cl})^{1.456} \quad (9)$$

The above equation stands for a granitic magma with viscosity of 10^6 Pa.s, as it occurs in porphyry-type deposits.

The computed enrichment in metal should be taken as provisional numbers, in that sense that the most important is the order of magnitude, rather than their exact value (Vigneresse, 2019). Their values are first computed relative to the Cl content into the MVP (Table 1). An enrichment factor of 4 orders of magnitude is easily reached for Au and Ag. The low enrichment factor for Sn and W may reflect the absence of F in the MVP when selecting the partition coefficient values. The threshold is delineated between 10^{-13} and 10^{--15} m^2/s, corresponding to the change between low and high Péclet numbers for elements, i.e. a change from diffusive to advective flux.

It provides insights to the development of the process, but the large variations observed in the values of K and D (Figs. 7 and 12), summarized in Fig. 18, still induces uncertainties. The maximum possible enrichment value requires determining the total volume of the intrusion, which is rarely known with sufficient precision. However, assuming a 10 × 10 × 5 km intrusion, the intrusion totalizes 500 km^3 in volume. Using an average Cu content of 20 ppm in the source, the bulk

Table 1
Selected partitioning coefficients and diffusivity values at 600 °C for various elements. In addition, the enrichment factors (Eqs. (8) and (9)) are computed, showing the fate of metals in the MVP.

Element	K_i	$\log_{10}D_i$	E_{min}	E_{max}
Cl	27	−12.5	1.00	0.00
Cu	440	−10.1	16.3	8620.3
Mo	8		0.30	
W	12	−13	0.44	0.10
Sn	10	−12.8	0.37	0.09
Au	500	−9.2	18.5	63420.5
Ag	90	−9.5	3.3	860.8
As	2	−15	0.07	0.00
Pb	3	−12	0.11	0.03

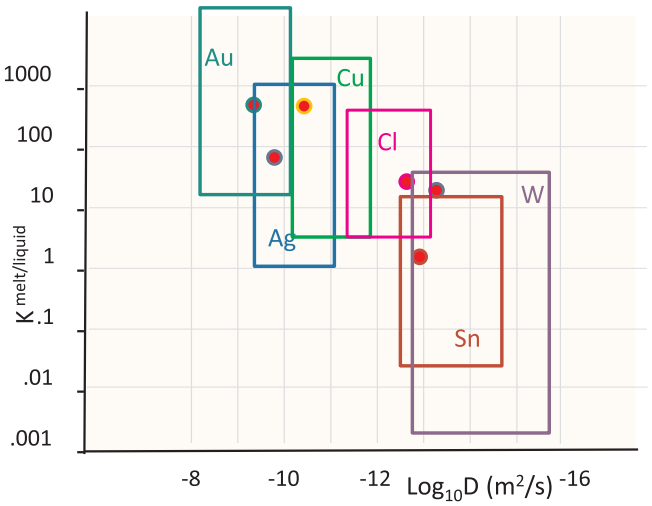

Fig. 18. Diagram summarizing the diffusion and partitioning of metals leading to form ore deposits. The respective values are indicated by a box, showing the large spread of the values. Source and values are dialed, in the text, and on Fig. 7 for partitioning, and Fig. 12 for diffusivity. The circles indicate the final selected values during the computation.

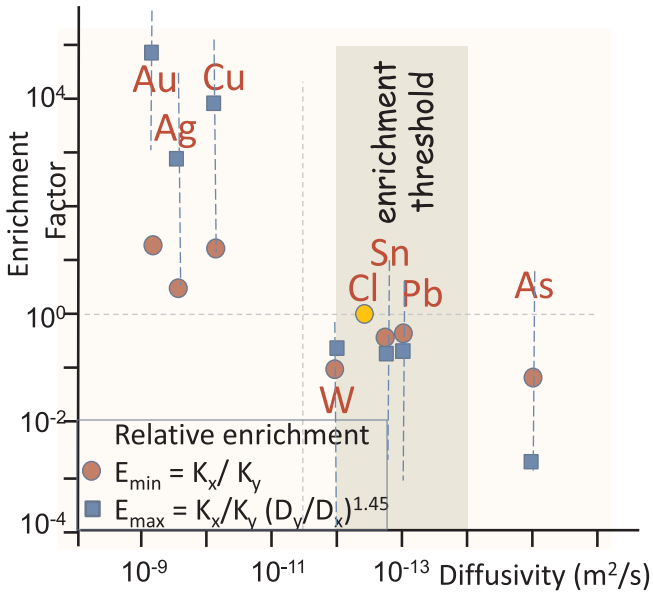

Fig. 19. Metal enrichment according to the diffusivity values for Au, Ag, Cu, W, and Sn, with Cl taken as a reference. Enrichment for Pb and As are also indicated, but their low diffusivity or low partitioning does not result in activating a transport through MVP. The enrichment factor is computed from the values of the partition coefficients and diffusivity (see text). An estimated error bas is indicated by a dashed line. It roughly mimics the spread in the partition coefficients values. Nevertheless, a factor of 3–5 orders of magnitude is easily reached for fast diffusing metals.

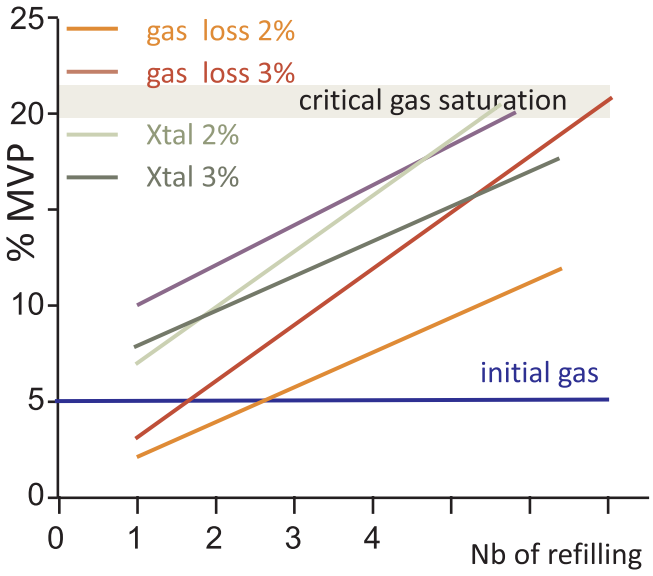

Fig. 20. Relative percentage of the MVP as a function of the successive recharge in magma. The number of magma recharge is indicated, in different situations, with 2 or 3 wt% of gas reinjected into the system when 10% of MVP is already present. A situation is shown in which 2% of the initial MVP can escape the sytem, or when crystallizing magma (Xtal) increases by 3%.

amount of Cu is 145 MT, large enough to form any copper deposit (Sinclair, 2007). In this case the enrichment shoud be around 10^6.

The second limiting constraint is the null, or poor enrichment. Hence if the model well describes the enrichment process, it should also explain why the intrusion remains barren, or eventually with the initial metal abundance.

Diffusivity values have been selected at 600 °C, the temperature of a consolidated mush, within a granitic or equivalent melt (Von der Gönna and Rüssell, 2000, Benne and Rüssell, 2005; Kaufmann and Rüssell, 2010; Zhang et al., 2010). In a similar way, metal partitioning coefficients have been selected from the literature (Li and Audétat, 2012; Lukanin and Dernov-Pegarev, 2010; Zajacz et al., 2008, 2013). From this compilation (Fig. 7), values have been considered within varying conditions (S, or halogens content into the MVP). Boxes indicate the range of variations, for both partitioning and diffusion. The spread is quite large for partitioning, extending on nearly 4 orders of magnitude (Fig. 18). Nevertheless, the spread in diffusion remains lower, extending over 2 orders of magnitude. The selected values are provided in Table 1. No values are provided or Mo, since it was impossible to find an estimate of its diffusivity.

The estimated relative enrichment factors are computed from both formulas indicating the minimum (Eq. (8)) and maximum values (Eq. (9)). Enrichment factors show the estimated values for each considered metal (Fig. 19). The spread of the initial values in partition coefficient values, about 4 orders of magnitude, implies an error bar of about ± 2 orders of magnitude.

3.3. Time aspects

One important aspect of the model comes from the progressive building of the magma chamber by successive intrusions. It is not a so trivial assumption as it may explain the observed multiple ore deposit centers within a massif. It also bears importance in the building of a MVP large enough to overcome the CGS. It has also consequences on the final ore grade, in that sense that the model is able to reach an optimum enrichment cycle as demonstrated by statistical simulations (Chelle-Michou et al., 2017).

3.3.1. Successive magma inputs for the MVP to complete the CGS

The completion of a critical gas saturation represents about 20% in volume of gas (Bear, 1988). Obviously, such an amount can hardly be reached during one single intrusion, since the amount of MVP hardly reaches 7–10%, even in water-rich magmas. Successive magma inputs, i.e. a longer time, are necessary to reach an adequate critical volume of MVP (Fig. 20).

A rough estimate can start with an initial MVP content of about 5% in each new magma input. The volume of the new input is estimated at 10% of the total volume of the final magma chamber, and to facilitate the computation, it affects locally 10% of the total magma. Thus locally, the total MVP is inflated by the 5% of the new fluids released by the

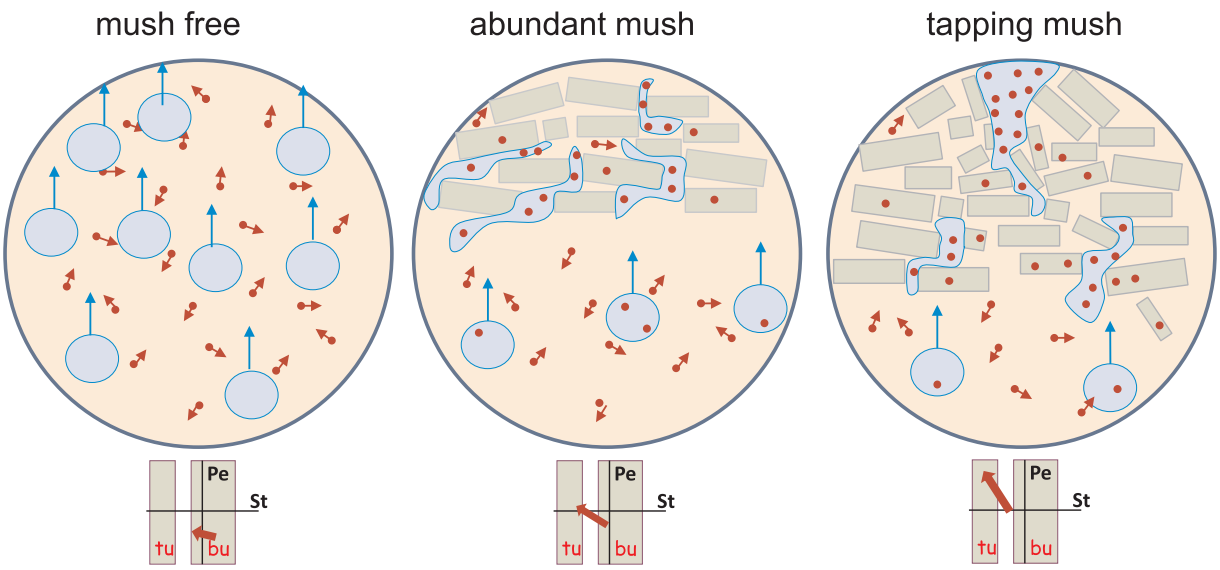

Fig. 21. Schematic model of ore formation developing on three major stages for each cycle. A mush free magma corresponds to a melt in which MVP exsolves (large bubbles) moving upward (arrows). Metals (small circles) diffuse within the melt (small arrows), and may incorporate the first formed crystals (rectangles), becoming inert due to their diffusivity in solids. Another possibility for metals is to enter the MVP, thus being carried by buoyancy, or even stay into the melt. With ongoing crystallization, a mush forms, tapping the melt and MVP. Due to the cooling, the Stephan number decreases whereas the Péclet number slowly increases. Tubes (tu) take progressively over bubbles (bu). At last, pressure accumulates under the taping mush. Explosive brecciation leads to release of the metal-rich MVP.

new magma input. Five situations are explored (Fig. 20). The simplest situation assumes refilling and MVP exsolution without any loss due to gas escape or volume change due to crystallization. The MVP increases by about 5% during each magma refilling, the curve is linear with recharge and 4 new magma inputs are required (Fig. 20). Two other models assume gas escape of 2 and 3% in between magma refilling. They develop without change in crystallinity. The resulting curves show a slower increase in MVP with slope 2 and 3 respectively. In the higher gas escape rate, up to 10 episodes of refilling are necessary. The introduction of partial crystallization, 2 and 3% respectively, between magma refilling episodes results in linear slopes of about 2 or 3, similar to those of gas escape, but at higher values (Fig. 20). A minimum of 5 refilling episodes is required. Non-linear increase of the MVP develops when the crystallization affects the whole magma chamber, i.e. the intial and new magma, whereas the gas escape only affects the intial magma. Nevertheless, the total number of magma inputs always needs many smaller inputs of magma.

3.4. Metals enrichment is cyclic

The process of metal enrichment within the MVP is cyclic corresponding to MVP exsolution, tapping up to reach the CGS and escape. Thus, a competition develops, not only between metal diffusion and advection, but also between magma crystallization and refilling. The cycle mimics the process of magma degassing (Cashman and Giordano, 2014; Girona et al., 2015). Hence volcanic eruptions are better described by the successive tapping of multiple melt lenses stored within a crystalline mush. The resulting outgassing of each lens opens pathways that are periods of quiescence, followed by bursts of gas.

The metal enrichment follows a diffusive process, ruled by the Fick law, i.e. an exponential increase of the metal concentration with time. It is of common use to introduce a characteristic length (L) and time (τ) to describe the process (Fig. 11).

$$L = (D\tau)^{1/2} \quad (10)$$

The characteristic length scales as 0.6 m/yr to 6 km/Myr, for values of metal diffusivity (D) in the melt ranging 10^{-8} to 10^{-16} m^2/s. Such values assume conversion of time units from years to seconds (1 yr = $31.576 \cdot 10^6$ s). It should be compared to the different characteristic lengths for diffusive (heat, magma motion, elements diffusion in melt and solids) processes (Fig. 9). For common metals, the characteristic length ranges from metric to kilometric in a period of 1–30 ky. The later corresponds to the time scale for each magma pulse. Assuming that 3–4 magma inputs are required to reach the critical gas saturation level, the total time left for diffusion is about 100 kyr.

Ore genesis is quite analogue to the charge and discharge of an electric capacitor, or better said, it mimics the self-charge or self-discharge of a capacitor-like junction, or transistor. The difference is that a capacitor presents an exponential discharge, with a time constant, since it occurs within an electric circuit, i.e. by charge displacement (advection). In contrast, self-discharge occurs spontaneously, with a discharge due to charge diffusion that follows an error function value, which is not actually a true exponential.

The respective evolution of the melt and its MVP makes their evolution dual to each other in terms of metal content. Metals are charged into the MVP whereas they are discharged from the melt. Metal enrichment thus follows the same additional law as electric capacitors. When the capacitors are placed in parallel, i.e. develop at the same time, the result is a sum of the respective capacitance. It corresponds to increase the distance between the planes of a capacitor, thus decreasing its total capacitance. In contrast, when in series, the resulting inverse of the bulk capacitance is the sum of the inverse of individual ones. It corresponds to increasing the surface of the plates of the capacitor, i.e. to increase the total capacitance. Obviously, the occurrence of several cycles of ore genesis indicates a development in parallel, although the difference in metal abundance could reflect a serial process. The analogy could be of importance in experimenting analogue models of ore generation.

4. Toward a new paradigm

The proposed model, not only offers new insights into ore genesis, but it opens new perspectives for ore targeting and future scientific research.

The proposed model for ore generation (Fig. 21) suggests that the metal enrichment, about 3 to 4 orders of magnitude, takes place during the magmatic stage, before the hydrothermal circulation. The latter, that obviously leads to a strong alteration of the surroundings of the

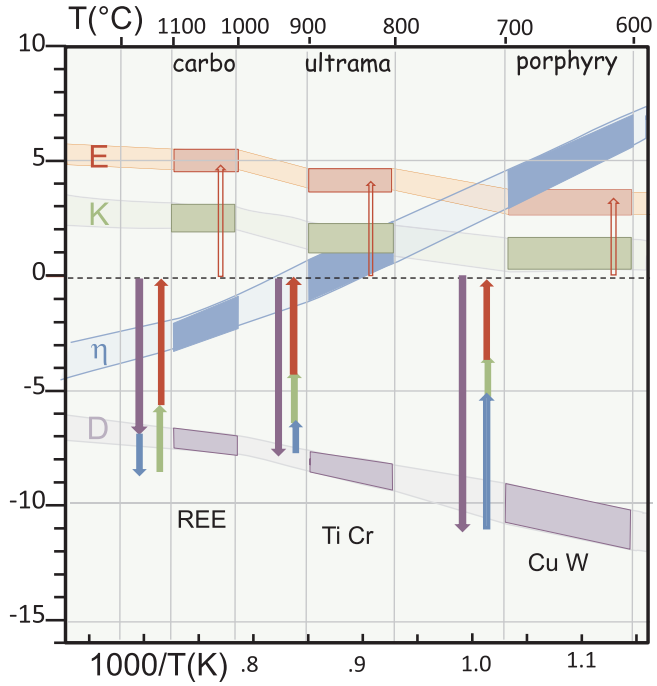

Fig. 22. Reconstructed diagram showing the $\log_{10}$ values of diffusivities (D), viscosity (η) and partition coefficients (K) between metals and MVP, sulfide and CO_2, respectively explaining ore generation in porphyry, ultramafic and carbonatitic magmas. The temperature is that of the mush, about 200 °C less than the melt. The enrichment factor is taken as the sum of diffusivity, viscosity and partitioning (Eq. (12)). In logarithmic units it is always larger than 3.

intrusion, is the place of metals precipitation. It is the consequence of a delayed time for the MVP to escape the magma chamber, owing the high crystallinity of the mush. This in turn supposes that the evolution of the magma chamber spans a long time, rejuvenated by new magma (and associated MVP). The whole process also shows a hierarchy of the controlling factors (see Fig. 22).

4.1. A three stages process

The whole process of ore generation develops during three major stages (Fig. 21). In absence of the first formed crystals, only two phases are present, the melt and an exsolved MVP. Metals are within the melt and diffuse toward the MVP. The process develops at low Péclet number, leading to bubbles formation. Because of their intrinsic buoyancy, MVP rapidly ascend and do not leave time for metals to diffuse, up to reach concentration into the MVP. With ongoing cooling, a mush forms that slows down the motion of the MVP. Tubes progressively take over bubbles, decreasing the Stephan number, whereas the Péclet number slowly increases. Metals still diffuse into the melt, being incorporated either to the MVP, or into yet formed crystals, where they become inert because their diffusivity increases too much, according to the lifetime of the magma chamber. At last, the growing mush taps the MVP, whereas diffusion still concentrates metals into MVP. With the increasing pressure, the mush cannot held the MVP, brecciation occurs that liberates the metals rich fluids (Fig. 21). Accordingly, the Péclet number increases, and fluid advection carry metals before they precipitate to form ore veins.

4.2. Metal enrichment

The present model quantifies the enrichment in any metal. The formulation mostly depends on the Péclet numbers associated with the considered metal, leading to two extreme cases. One corresponds to the initial case of no advection. It is simply the ratio of the partition coefficients of the metal toward the MVP. The real enrichment occurs after advection, and incorporates the gain realized through diffusion, modulated by the initial abundance of the considered metal. In this case, a threshold discriminates fast diffusive metals, only able to reach enrichment by several orders of magnitude.

4.2.1. Hierarchising the controlling factors

Previous suggesrion for the formation of porphyry deposits should be re-examined in the light of the present model, and in that sense it constitutes a new paradigm. Although the importance of the magmatic stage has been already formulated (Hedenquist and Lowenstern, 1994; Williams-Jones and Heinrich, 2005; Audétat and Simon, 2012), the quantification of the enrichment had not been modeled. It had been observed, looking at the metal content in the melt and fluid inclusions, and partly explained through experimental determination of the partition coefficients (Li and Audétat, 2012; Zajacz et al., 2008, 2013). This supposes a long and tedious, but necessary, experimental determination of such values, taking into account the various factors modifying elements partition.

The quantification also invalidates the other suggestions for enrichment that do not achieve the 3–4 orders of magnitude. Among them, the source enrichment in the mantle (Arndt et al., 2005), the remobilisation of a previous deposit (Marshall and Gilligan, 1987) or the mobilization of an external source have been suggested. Such processes hardly reach the 1–2 orders of magnitude (Arndt, 2013). Indeed, the initial abundance of any metal in a granitic melt can easily reach some millions of tons of the same metal in a magma chamber. The case of so-called specialized granites (Štemprok, 1982), interpreted as resulting from a chemical differentiation, with metals remaining in an evolved melt supposes metal concentration from a kilometric-sized magma chamber into a very small domain. The concentration from ppm to % requires volume shrinking by about 20 and by still one order of magnitude more when passing from ppb to % levels. This seems unrealistic, especially when considerin giant ore deposits.

Other factors have been suggested to explain the formation of ore deposits. Among them, the tectono-magmatic conditions, leading to the so-called ore provinces (Richards, 2003) represent a puzzling problem. The large scale tectonics, controls the magmatism at plate boundaries, and partly within plates. Consequently, the magmatism above subduction zones is partly controlled by the plate boundary conditions. In particular, when the mid-oceanic ridge is involved into the subduction, it leads to specific thermal conditions, manifested by adakitic magmatism (Martin, 1999; Martin et al., 2005). The link of Au- or Cu- deposits with such adakitic magmatism has been suggested (Oyarzun et al., 2001; Reich et al., 2003). However, the correlation between Au and adakitic magma is not a causal relation. It is not the fact that the magma is adakitic that yields Au deposits, since many other adakitic intrusions are barren. Similarly, the transition between changing boundary conditions (e.g. ridge subduction, slab rollback, etc) commonly considered as relevant to tectonic environment (Richards, 2009, 2013) should be considered as modifiers of the process parameters, but not as the main cause of metal enrichment.

The conditions at plate boundaries, where magmatism develops, do not control the mineralization process, but they obviously control the type of mineralization, mainly through the redox conditions of the magma, distinguishing between reduced and oxidized porphyry bodies (Cao et al., 2014). The type of magma and associated MVP in turn, control the metal that will potentially concentrate into a deposit (Cu, Au, Ag, W) in case of oxidized magmas, and Sn, Mo and HFSE in case of reduced, more felsic magmas. The link between magma specialization for one metal and redox conditions has long been advocated (Thompson et al., 1999). Redox conditions are critical in controlling ore formation since they control the type of magma during ore genesis. Indeed, the redox conditions separate the reduced ilmenite-bearing granitoids from oxidized magnetite-bearing granitoids (Ishihara, 1977, 2004). The redox consitions also differs for alkaline magmas (Fig. 3).

Oxidized magmas are classically observed in subduction zones or in post-subduction magmatic belts. They are genetically related to the magnetite-series I-type granitoids. They contain oxidized minerals such as magnetite, hematite and anhydrite, high SO_3 in apatites, leading to sulphate-bearing minerals including primary anhydrite. They show high oxygen fugacity (f_{O2}) about 2–3.4 log units above the FMQ buffer (Fig. 3), ranging between the hematite–magnetite (HM) and nickel-nickel oxide (NNO) oxygen buffers, most exceeding NNO + 2 (Richards, 2003). Such high oxygen will ensure that sulfate is the exclusive sulfur species in the melt (Carroll and Rutherford, 1987; Nadeau et al., 2010), and that it significantly increases sulfur solubility in the melt (Jugo, 2009; Jugo et al., 2005). Most Cu-porphyry deposits belong to this category, with examples at Chuquicamata (Parada et al., 1987), El Teniente, both in Chile (Vry et al., 2010), Santa Rita, New Mexico (Jacobs and Parry, 1979; Audétat et al., 2004).

In contrast, reduced magmas are observed in the continental crust in convergent settings and are genetically associated with ilmenite S-type granites. They are characterized by the presence of pyrrhotite and absence of anhydrite and hematite, and low SO_3 (< 450 ppm) in apatite. Their oxygen fugacity (fO_2) is commonly 0.5–3.0 log units below the fayalite-magnetite-quartz (FMQ) buffer as indicated by the assemblage K-feldspar-biotite-ilmenite-quartz (Fig. 3). Such magmas usually present high F content, and are associated with the development of Sn ore bodies. Such examples include the Variscan granites from Cornwall (Bray and Spooner, 1983) and Bohemia (Breiter et al., 2005). Nevertheless, some reduced porphyry copper deposits are also observed (Rowins, 2000). They are related to ilmenite-series, but reduced, I-type granitoids. They lack primary hematite and anhydrite, but contain abundant pyrrhotite. Such examples include the Catface (Smith et al., 2012) and the Baogutu (Cao et al., 2015) Cu deposits. To conclude about the redox conditions, it appears more effective to use the associated components of the MVP, manifested primarily in biotite and apatite composition, to infer the underlying metals (Vigneresse, 2019).

The link with local tectonics has also been advocated, as indicating a link between porphyry deposits and regional fault patterns (Behn et al., 2001; Richards, 2003). The problem is similar to the association between granitic plutons and faults, with arguments that the magma ascent is easier within fault planes. However, detailed gravity survey inversions have demonstrated the absence of link between granitic root zones and adjacent faults (Vigneresse, 1995). A fault is by definition a zone in which constraints accumulate, up to rupture. When a fault zone also serves as a conduit for magma, the melt lubricates the fault, releasing the constraints. Conversely, and this is clearly indicated by gravity inversion, a fault will control the wall of the plutons in the upper crust (e.g. Mortagne, Brittany, France) (Guineberteau et al., 1987). Stated differently, the rate of faulting is largely faster that the emplacement of a pluton, but the rejuvenation of faults often leads to dismember porphyry bodies (e.g. La Escondida, Chile) (Padilla-Garza et al., 2004). In contrast, faulting and fracturing may provide open spaces for metals to precipitate.

4.2.2. Re-examining the controlling factors

Having identified the factors controlling the formation of an ore body, they can now be hierarchized. A competition between advection and diffusion controls metal enrichment, pointing to a time-dependent factor (i.e. the rate under which the processes develop). The fastest rate dominates over the slow ones. One identified parameter is crystallization whereas the other is the rate to which the different inputs of magma, including their MVP, refill the magma chamber. In case of a dominantly felsic magma chamber, the refilling can be done through felsic or mafic magmas. Both magmas profoundly differ in their MVP component and volume. Refilling by a mafic magma leads to effusive processes. Conversely, refilling with felsic magmas is more dramatic, since it can lead to explosive eruptions (Eichelberger et al., 2000) due to a larger water content. However, such dichotomy develops through large refilling of the magma chamber, as observed in volcanoes. When the volume of refilling is low, or when the MVP volume remains moderate, outgassing has time to develop through bubbles instabilities (Shields et al., 2014). As a result, the metal concentration by diffusion also remains low, eventually leading to low grade ore.

The fluid sparging model is a competition between advection and diffusion, but also between partitioning and viscosity, although these processes rely on very different grounds. The firsts are a matter of process, whereas the later are a matter of quantities. Obviously, the process controls the quantity. Metals diffusivity values are the second controlling factor. Magma viscosity appreas to be a third factor (Eq. (4)). The competition between the rates of the different proceses also points to their non-linearity, i.e. variations. This differs from the mineral system as stated previously.

4.3. A preliminary note of caution

Before suggesting a global model for ore generation related to an intrusion, some caution should be formulated, owing to the actual level of knowledge and basic assumptions.

4.3.1. Lack of data from the field

One striking point coming out from the literature on economic geology is the lack of data on the state of the magma chamber. Surprisingly, many studies on deposits lack even a bulk chemical description of the magma, although the associated parameters (e.g. isotopic composition, age) are described in detailed. The physical parameters associated with the melt (viscosity, temperature) are often omitted. For the associated MVP, few datasets provide the full content in the three or four major components (CO_2, F, Cl, S). Conversely, studies on isotopic characters ($\delta^{18}O$, δD, $\delta^{34}S$) are examined, mainly to determine the fluids origin, internal or external to the magma. Some studies even ignore the magmatic stage, focusing on the late hydrothermal effects.

In a single deposit, several orebodies are often identified, but there is only a few hierarchical classification between them (e.g. in age, or temperature) or correlation between the MVP components such as relatice age determination or even the metal grade. Nevertheless, the respective enrichment factors differ from one orebody to another in the same intrusion, indicating that the time left for diffusion has been different for each orebody.

The internal structure of a magma chamber is also still poorly known by lack of direct observation. The usual model of a big blob of magma that evolves through chemical differentiation is certainly obsolete, as well as the continuous evolving magma generation (Hildreth and Moorbath, 1998), exemplified by the Bishop Tuff magmatic body, known as the Standard Model. The processes of magma generation and segregation are discontinuous (Vigneresse, 2008), so that a magma chamber is incrementally built. Its structure must also be discontinuous. Recently, revisiting the Bishop Tuff magma body, the body has been interpreted as being zoned (Gualda and Ghiorso, 2013) as already stated at the Fish Canyon, Colorado (Bachmann et al., 2002; Bachmann and Bergantz, 2008). A nice cartoon illustrates what now is thought about a magma chamber (Cashman and Giordano, 2014), representing zones of melt abundant (i.e. crystal poor) with intermediate “layers” of mushy magma (i.e. crystal rich). Such zoning is also predicted from chemical evolution of large magma chambers (Solano et al., 2012). During degassing, the MVP derives from any of such crystal-rich and crystal-poor zones, i.e. adding variation in pressure. Indeed, the total height of a magma chamber, about 4–6 km, induces variation in pressure byabout 100 MPa, or 1 kbar. The major effect would be on the MVP components solubility into the melt, hence on the composition of the MVP.

4.3.2. Lack of experimental data

The lack of experimental data for the physical parameters is the most important factor assuming a sparging model to other ore deposits.

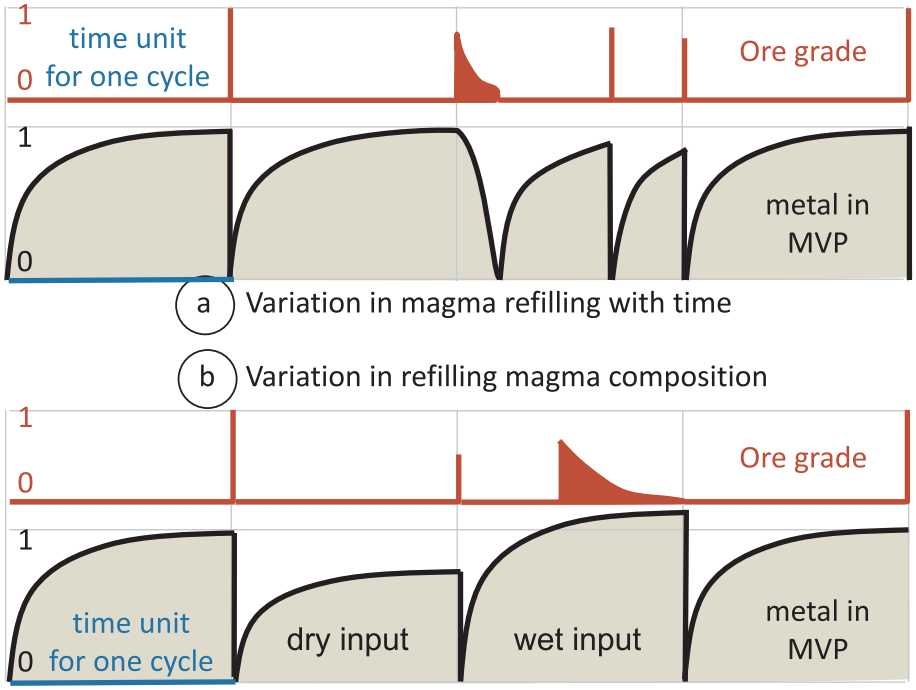

Fig. 23. Schematic non-scaled conceptual evolution of the melt and associated MVP in case of magma refilling with time (a) and a variable fluid content (b). The diagrams for melt and MPV are dual to each other and behave as the charge and decharge of a capacitor. The scale in time is the ideal time for a cycle to achieve optimum completion. In case of delayed recharge, the MVP and its metals slowy outgases. Conversely, when the time interval beween recharge is small, diffusion has no time to reach optimum enrichment. When the MVP varies in abundance, in case of a dry or wet input (b), the result is a low-grade deposit, with eventual progressive degassing, after reaching the CGS.

The present model assumes coefficient for partitioning metals between the MVP and the melt. As seen earlier (Fig. 8), the coefficients vary with the magma (ASI, NBO/T, redox) and the MVP components (H_2O, F, Cl, S). This is valid for each considered metal. Though a precise value is not immediately needed, a range of variation would be important to infer in a very first step the most effective controlling parameter.

The other cruel lack of data relates to the physical parameters of the magma, with its composition. It mainly concerns viscosity and metals diffusivity in the melt. For magma viscosity estimates, some general relationships do exist (Mungall, 2002; Giordano et al., 2008). There are poorly adapted to carbonatites. Similarly, data on metals diffusion in silicate melts is lacking, in spite of an extensive compilation (Zhang et al., 2010). With such a data set, it would be interesting to compute Péclet numbers for each metal-melt couple.

4.3.3. Implications for a global scheme

The lack of observations and experimental data for the physical parameters is an important factor before a global scheme can be constructed. Nevertheless, the actual data set indicates a huge gap between metal enrichment values when considering the causal parameters (Section 4.2). It results that the magnitude of enrichment bears more significance than its exact value (Vigneresse, 2019).

4.4. Toward a global model

The suggested model of fluid sparging (Huber et al., 2012) has been basically elaborated for a magma chamber evolving in crustal conditions, focusing on porphyry-type deposits, with their associated metals (Cu, Au, Ag, Mo, W, Sn). The formulations highlighted the major problem reltative to ore generation, i.e. the metal enrichment factor (Vigneresse, 2019). Having identified the controlling parameters leading to metal enrichment, it seems interesting to generalize the model to any intrusion type.

4.4.1. Individualizing the factors of enrichment

In the present model, metal enrichment is defined according to a Péclet number and a metal partitioning between melt and MVP, the composition of both being those of a porphyry-type deposit. It highligths three major components that could be individualized, namely the metal diffusivity within a given melt, the melt properties and the metal partitioning between melt and MVP. The two former points relate to the definition of an individual Péclet number separating diffusion from advection. The last point relates to the difference in chemical potential between metals and the MVP composition.

In the original approach (Huber et al., 2012), the enrichment factor is computed relative to the behavior of Cl (Eqs. (7) and (9) in the present paper). A global model should get rid of a relative value, assuming that the order of magnitude only bears importance. The Péclet number in its actual form (Eq. (4)) compares the metal diffusivity within a given melt to the motion of this melt through advection. Therefore, it is valid only for a given couple metal-magma type, assuming the other parameters such as temperature being constant. Since the Péclet number incorporates both metal diffusivity and melt viscosity, their effects should be individualized.

$$Pe \sim 10^{-8}/D_i/\eta \quad (11)$$

The value of paritioning should also take into account the difference in chemical potential between the melt and metal. Consequently, the enrichment factor E_{Me} writes as a direct function of metal partitioning ($K^{Me/mvp}$), inverse function of metal diffuvity (D_i) and inverse function of melt viscosity (η). Since the three parameters present an exponential inverse dependance on temperature such as exp (E_0/RT), with E_0 an activation energy and the perfect gas constant (R = 8.31 J/K/mole), the enrichment factor for a metal (Me) writes as a sum of three factors using a logarithmic scale.

$$\log_{10}E_{Me} = (\log_{10}K^{Me/mvp} - \log_{10}D_i - \log_{10}\eta) \quad (12)$$

A further step would involve taking into account the different effects (temperature, chemistry, melt structure, cf Fig. 8) on partitioning and diffusion to identify, and reassembly such effects into the preceding equation (Eq. (12)). This step is obviously out of scope of the present paper.

4.4.2. Generalizing to other intrusions

A tentative diagram (Fig. 23) illustrates the metal enrichment for porphyry, ultramafic and carbonatitic magmas. The considered metals are Cu and W, Ti and Cr, and REE in the three cases. For porphyry-type deposits, the assumed mush develops at about 600 °C and slightly

above, with a melt viscosity about 10^6 Pa.s. (Giordano et al., 2008). The MVP is essentially composed of S and Cl, the remaining F phase stays in the melt (Vigneresse, 2019). Metal diffusivity values range 10^{-14} to 10^{-11} m^2/s at such temperatures (Zhang et al., 2010). Metal partitioning between a S-rich MVP and melt is about 30–100 when dealing with Cu to Au (Zajacz, 2015).

Ultramafic magmas intrude the crust at higher temperature 1200 °C, resulting in a mush around 900 °C. Their viscosity is around 1 Pa.s (Persikov et al., 2015). The considered metal (Ti, Cr) diffusivities at such temperature range 10^{-9} to 10^{-10} m^2/s. The associated MVP is still mostly aqueous, and does not really acts in segregating metals, because of the low partition coefficients (< 50). However, another immiscible phase, represented by sulfides develops, that increase the partitioning (150). Because its chemical potential is much lower than an aqueous MVP, and consequently with the melt, it has more potential for having higher partition coefficients.

It would explain the V, Ti, Ni, PGE deposits associated with ultramafic rocks and as found in Tomtor Siberia (Kravchenko and Pokrovsky, 1995), or Kola peninsula (Barnes et al., 2001)

At last, carbonatitic magmas represent another possible application. The involved MVP becomes CO_2 dominant, with an eventual dolomitic phase scavenged from the surrounding. Again it forms an immiscible phase playing a similar role as the halogen and S-rich MVP in granodioritic magmas. The chemical potential of such CO_2 rich phase is quite different from the melt, thus leading to higher partitioning values (about 200). Similarly, the viscosity of the melt (10^{-2} Pa.s) implies diffusivity values of the order of 10^{-9} m^2/s (Mungall, 2002).

It would explain REE rich ore such as in the giant Maoniuping Sichuan, China (Liu et al., 2018), or Bayan Obo deposits (Yuan et al., 1992; Fan et al., 2016), or Tsagaan Tsahir in Mongolia (Jargalan and Fujimaki, 2003).

4.5. The importance of rates

All provided numbers (Table 1) should be considered as rough estimates, owing to the error bars on the values of K and D (Fig. 18). The partition coefficient values (K) vary by about 2 orders of magnitude, depending on the composition of the MVP. The variation reaches 4 orders of magnitude for W. Diffusivity values also vary according to the temperature and chemistry of the melt. An error bar of ± 1 order of magnitude is estimated (Fig. 18). For temperature variations, the energy activation of diffusivity results in about 1 order of magnitude variation for a change of 100 °C in the melt.

4.5.1. The different rates, melt and MVP as dual evolution

All motions are controlled by non-linear velocities resulting from gradients. The acting forces ruling elements motion are essentially chemically-driven gradients (Fig. 1). For diffusion, it is a concentration gradient. For partitioning the driving force is a chemical potential gradient. Conversely, the driving force for bulk motions is mechanical (Fig. 1). It consists in buoyancy and stress for the melt and the MVP within the mush. Obviously, chemical and mechanical forces do not have similar amplitude and length of attraction, inducing a supplementary gradient between acting forces. It is fully obvious that the system may become rapidly unstable, with positive and negative retroacting loops. It partly explains why numerical models have not yet been developed, using usual Eulerian formulation. The microphysical approach (Parmigiani et al., 2014) perfectly illustrates this situation for understanding a mushy behavior. Consequently, new analogue models should be developed that take into account both non-linear behaviors and unusual growth of one element.

4.5.2. Playing with rates

The analogy with capacitor remains an analogy, i.e. it does not act as what happens really. However, it merits attention, since it could explain how the present model could also apply to barren intrusions. All conditions for optimal balance between diffusion and advection are not reached, leading to low-grade deposits. This is a crucial point, since barren and ore deposits are often observed in intrusions sharing similar chemical, historical and tectonic conditions, at a quite similar time. This indicates local effects, i.e. internal processes acting in a single intrusion, rather than regional controlling factors.

The previous analogy immediately gives important insights on the influence of cycles in ore generation (Fig. 23). Both the metal content within the MVP and its release as ore are estimated in a diagram scaled in time units required for a cycle of diffusion/advection. The metal enrichment, whatever the metal, follows an exponential increase within the MVP. When reaching the CGS, the advection process starts and delivers ore, with a given, if possible optimum grade (Fig. 23). This is the basic cycle of the process, taken as one time unit, and repeated with new magma infill.

Varying the time frequency of the cycles bears consequences on ore generation (Fig. 23a). First, a too long time interval, f.i. between magma recharges results in metal concentration that is not necessarily higher, because the exponential process may reach saturation. The MVP volume may still increase, but when reaching the CGS, advection liberates the MVP at a slow decreasing rate, resulting in low ore grade. Conversely, when the refilling rate increases, the optimum metal concentration is not fullfiled. The delivered MVP presents lower ore grade (Fig. 23a).

Another situation may develop, when magma refilling occurs with wetter or dryer magma (Fig. 23b). The optimum cycle is similar to the previous case, in the adequate time limit. In case of refilling at the adequate frequency, but with less MVP exsolution, the MVP has not reached the required CGS at the end of the time. A limited amount of ore only is evacuated (Fig. 23b). Conversely, if the new magma input is wetter, the MVP rapidly reaches the CGS, but without the optimum metal concentration. The ore grade is lower, and may be its decreases progressively with time, until a new refilling occurs (Fig. 23b).

4.5.3. Implications of the different rates

The discussion about the different rates of intrusion and/or metal enrichment suggests that some kind of hierarchy establishes between the various processes, physical and chemical, that develop within a magma chamber. Going back to Fig. 6, it illustrates the rheological response of the three phase magma to strain rate. In its initial form, it represents the inverse of viscosity for a crystallizing magma. The solid phase follows a power law in strain rate, i.e. its effective viscosity depends on the applied strain rate. This strain rate (γ°) can easily be converted in usual rate, i.e. in s^{-1} units, assuming a strain ($\gamma = 1$).

First the experimental studies, either with a varying solid phase (Φ) or gaseous phase (β) (Pistone et al., 2013; Champallier et al., 2008) are carried out at a too rapid strain rate, about 10^{-4} or 10^{-5} s^{-1}, to let time for instabilities. The magma chamber reacts as a single phase, slightly altered by the other ones.

At lower strain, 10^{-11} to 10^{-13} s^{-1}, the magma settles, as recorded by the developing fabrics, and under local higher strain rates by local instabilities (Vigneresse, 2015). Those induce mineral segregation, compositional banding and biotite-rich schlierens. Magma veining and vertical motion of melt-rich magma also develop with increasing strain rate. However, the controlling factor is commonly viewed as mechanical, though mineral segregatation has also chemical implications.

Ore bearing porphyry deposits document a lower strain rate, 10^{-12} to 10^{-14} s^{-1}, indicated by the time lag of their formation (Fig. 13). It also corresponds to mechanical instabilities, as manifested by the switch from a bubble-rich to tubes for the MVP flow. But the major implication is the metals segregation into the MVP, according to diffusion. A threshold value (η D) of 10^{--9} is suggested for determining the enrichment factor, that could correspond to the onset of the chemical versus the mechanical influence (Mungall, 2002). Therefore, the diagram of instabilities could illustrate the progressive change from mechanical to chemical instabilities. The magma evolution at much

slower rate, $10^{-14}\,s^{-1}$, would be the place of gentle chemical evolution, i.e. the usual chemical differentiation. Estimate rates of magma differentiation from zoned tuff yield values about 10^{-14} to $10^{--15}\,s^{-1}$ (Zellmer et al., 2005; Bachmann and Bergantz, 2008). At still a larger sacle, mantle differentiation during the early evolution of the earth is estimated to take 10^7 to 10^8 years, thus representing rates of 10^{-15} to $10^{--16}\,s^{-1}$ (Hofmann, 1988).

5. Conclusions

The different elements or physical phases that form in a magma chamber, i.e., the silicate melt, the formed crystals and the volatiles or MVP are examined for their physical and chemical properties. Their relative proportion continuously evolves during the magma chamber evolution, with strong variations during magma refilling. It suggests that time is also an important parameter that could influence the formation and genesis of ore as observed in porphyry-type deposits. A dynamic model is presented that develops through metals segregation and concentration into the MVP by diffusion from the melt. Provided a high crystallinity mush exists, it taps the MVP into non-connected bubbles, allowing time for diffusion to develop. After successive magma recharges, with the associated MVP, a critical gas saturation level is overcome and vertical tubes form that rapidly transport the metal-rich MVP to the surface by advection. The composition of the MVP, with water, CO_2, halogens and S, contributes to preferentially segregate metals according to their chemical affinities. This is controlled by the chemical descriptors, according to the chemical potential of elements. It is also constrained by mineral assemblages involving the MVP components (e.g. biotites, apatites). The enrichment factor of different metals (Cu, Au, Ag, Mo, W, Sn) is computed and reach the expected 3 to 4 orders of magnitude. In addition to the competition between diffusion and advection, another competition develops between magma crystallization and recharge, thus pointing to the different rates of the involved processes. Pardoxically, magma recharge, MVP advection and ore deposition are all rapid process compared to elements diffusion, while metal segregation and magma crystallization require slower processes. The presence of a mush slows down melt and MVP motions, inducing a competition between fast and slow processes. Nevertheless, a fast refilling of the magma chamber, coupled with a long lasting intrusive period are required to form ore deposits. In all other cases, the model predicts a barren intrusion.

Acknowledgements

The present paper issued after a long work (JLV) done on granite generation, followed by studies on the rheology of partially molten rocks with Jean-Pierre Burg and students (ETH Zurich). Then, the idea was to examine why metals concentrate to yield economic ore deposits. Such a reorientation of research benefited from financial support from CREGU, Nancy. A long 6 months stay at the AIST Tsukuba, Japan, with Sunsho Ishihara and colleagues introduced me to the links between granites and ores. Chemical studies were facilitated by a stay granted by the Center for Theoretical Studies (CTS) at the Indian Institute of Technology Kharagpur (IITK), India. There Pratim K. Chattaraj introduced me to the complexity of theoretical chemistry. A stay granted by CONICYT, with Eduardo Campos (U. Catolica del Norte, Antofagasta), introduced me to porphyry deposits. Intense and fruitful discussions with Olivier Bachmann (U. Washington, Seattle, now at ETH Zurich) and Chris Huber (Georgia Tech, Atlanta) resulted in the conception of the model of fluid sparging, benefiting from the numerical skill of Andréa Parmigiani (U. Genève) for settling the Lattice Boltzmann model. All of them are warmly acknowledged for their discussions and encouragements.

Declaration of interest

JLV built the model and wrote the first version of the paper. Many inputs to the text were provided by LT and AR. They declare not having any commercial or associative interest that could represent conflicts of interest in connection with the present work.

Appendix A

Structures observed in PMR and strain partitioning between phases contradict the assumption of a homogeneous response and rule out any description of a PMR by any averaging or effective property. Subsequent 3D ($\Phi - \eta - \gamma^\circ$) or ($\Phi - \tau - \gamma^\circ$) diagrams (Vigneresse, 2008) yielded new insights onto the rheology of PMR, by showing evidence for two thresholds bracketing a specific domain in which instability develops (Vigneresse et al., 1996). Such instabilities were attributed to the non-linear distribution of the phases and the rheological contrast between them (Burg and Vigneresse, 2002). Adding a third gaseous phase does not simplify the problem since gas bubbles deform much more easily than the melt and its solid network. Indeed, the first experiments with gas bubbles content indicated a moderate decrease in effective, i.e. equivalent mean viscosity (Bagdassarov and Dingwell, 1992). Interactions of deformation with partial melting or crystallization point to the importance of the rate along which melt remains segregated within its matrix (Misra et al., 2014). The rheology of such a multiphase material has recently been reviewed and commented for instability developments in intrusions (Vigneresse, 2015).

A silicate melt is commonly Newtonian under natural conditions, i.e. it shows linearity between strain rate and stress. The constant viscosity (η) is given by

$$\eta = \tau/\gamma^\circ \quad \text{(A1)}$$

Viscosity values can be estimated by the chemical composition of the melt (Hui and Zhang, 2007; Giordano et al., 2008). At 700–900 °C, the viscosity of a granitic melt is 10^6–10^8 Pa.s and 10^3–10^6 Pa.s for a basalt (Clemens and Petford, 1999). At very high strain rates ($\gamma^\circ > 10^{-4.5}\,s^{-1}$), the viscosity decreases (Webb and Dingwell, 1990) with increasing strain rate (shear thinning), but such strain rates are rarely observed in nature. Additional components to the usual 10 major oxides (e.g. water, halogens and other volatiles) commonly reduce melt viscosity although their respective effect is not always appreciated in numerical models (Bartels et al., 2013).

The matrix, or the solidified melt, can be considered as a solid rock, thus following a power law rheological behaviour (Kohlstedt et al., 2000).

$$\gamma^\circ = \tau^n A \exp(-Q/RT) \quad \text{(A2)}$$

The constants A and n, and Q the activation energy, are determined experimentally. R is the perfect gas constant (8.31 J/K/mole) and T is the temperature. In most rocks, n is close to 3, reflecting dislocation creep. Adopting experimentally derived values for amphibolites (Kirby and Kronenberg, 1987) as a proxy for PMR of granitic composition provide values for log A = −4.9 and Q = 243 kJ/mole. Therefore, the solid phase presents a viscosity around 10^{16} Pa.s at the temperature of crystallization of the magma. For a melt with an average activation energy of 400 kJ/mole, the melt viscosity increases by 2 orders of magnitude for a temperature decrease of 100 °C (Mysen, 1988). The large difference (about 10 orders of magnitude) in viscosity between the melt and the solid phase is the cause for numerous instabilities (Vigneresse and Burg, 2000). They reflect the role of the strain rate during a magma chamber evolution. They are also the two end-members charcterising a magma chamber evolution (Fig. 6).

With ongoing crystallization, the volume of the solid phase (Φ) increases, altering the effective magma viscosity. At Φ of about 50%, the solid crystalline framework reaches a rigidity threshold (RPT) above which global motion of the mush becomes restricted (Vigneresse et al., 1996). Tortuosity values, close to 1–1.5 up to Φ of about 50%, increases to about 3.5–4.5 when Φ approaching 75% which corresponds to the particle locking threshold (PLT) (Vigneresse et al., 1996). The solid crystalline framework develops tortuosity (Boudreau, 1996) slowing down the residual melt motion. Tortuosity also alters diffusion by an inverse square law (Van Brakel and Heertjes, 1974; Shen and Chen, 2007).

Wetting participates to gas bubble motion, especially in a dense mush. However, the concept of wetting angle is only valid at equilibrium, i.e. without external stress. In other conditions, wetting angles show anisotropy, making measurements irrelevant. The wetting angle and morphology of crystals are critical for bubble nucleation (Hurwitz and Navon, 1994). Fe-Ti oxides are very efficient nucleation sites, but in contrast, feldspar and quartz crystals are poorly observed in contact with bubbles. Bubbles grow very close to the feldspar grains, but they are never observed wetting their surface (Hurwitz and Navon, 1994; Pistone et al., 2012). As a consequence, feldspar grains slow down the motion of gas within a mush. The fact that the MVP is supercritical also renders surface tension ineffective.

The rheology of bubbly viscous fluids, i.e. a two-phase material, is complex and depends on the interaction between surface tension and shear rate. The effective viscosity slightly decreases with the amount of gas phase ($\beta < 0.15$). For high shear rate, surface tension controls bubbles shape. Nevertheless, for sufficiently large strains the effective viscosity of a suspension is greater than unity (Manga and Loewenberg, 2001). In a viscous fluid, free of solid phase, surface tension usually dominates the saturated water pressure by a factor 1.5–2 (Bagdassarov et al., 2000; Mangan and Sisson, 2000) and thus takes over bubble nucleation. Once formed, bubbles growth is controlled by diffusion of volatiles, though it has to overcome the viscous resistance of the melt (Gardner et al., 1999). The viscosity of the MVP is estimated at 10^{-3} Pa.s, and it depends on the strain rate, with a threshold occurring at strain rate of $0.03\,s^{-1}$ (Forien et al., 2011).

The rheological properties of three-phase mixtures have not been intensively investigated although experiments using a Paterson gas apparatus (Paterson and Olgaard, 2000) allow examining high temperature behavior of mixtures with any of the three phases (Caricchi et al., 2007; Forien et al., 2011; Pistone et al., 2012). Nevertheless, the strain rate in torsion is limited to high values ($5{\cdot}10^{-6}\,s^{-1}$ to $4{\cdot}10^{-3}\,s^{-1}$) whereas crystallinity (Φ) ranges 0.0 to 0.65 and gas phase β ranges from 0.02 to 0.12 (Caricchi et al., 2012).

As expected in bubble-free experiments, the relative viscosity increases with crystallinity (Caricchi et al., 2007). The presence of a third gaseous phase results in shear thickening at moderate crystallinity ($\Phi < 0.44$) whereas shear thinning is observed at higher crystallinity ($\Phi > 0.55$). The addition of a gas phase slightly reduces the effective viscosity, but the effect is quite moderate. A β value of 0.10 results only in a reduction by 0.1 order of magnitude of the viscosity (Pistone et al., 2012). Individual bubbles shape show an unexpected change from shear thickening to shear thinning that correlates with strong stretching, and break up similar to bubble boudinage. In case of low crystallinity, initial oblate shape of the bubbles switches to a prolate shape. In the first case, the initial shape leads to bubble coalescence and outgassing, inhibited in the case of a prolate shape (Shields et al., 2014).

The specific case of high crystallinity mush ($\Phi = 0.65$ and $\beta = 0.09$) is characterized by accentuated shear thinning. It results from crystal size reduction and shear banding, associated with strain partitioning for melt and bubbles and bubbles break-up, whereas small gas loss induces a small amount of shear thickening (Pistone et al., 2013). Shear banding and fractures develop preferentially during high crystallinity experiments, enabling outgassing (Shields et al., 2014).

Appendix B

Partitioning of elements from the melt toward the MVP is ruled by the coefficients of partition ($K^{melt/MVP}$) stating that the free energy should be equally dstributed at equilibrium between the components. It supposes that the chemical potential of each component should be equal, after having exchanged enough charges. The chemical potential of any elements can be computed from its chemical descriptors, i.e. electronegativity and hardness (Vigneresse et al., 2011). Basically electronegativity (χ), or the chemical potential (μ) changed of sign (Pearson, 1963), is the first derivative of the energy with respect to charge change. Hardness (ν) is the second derivative, i.e. the first derivative of the electronegativity. A third descriptor, or electrophilicity (ω) is often used, combination of the two previous (Chattaraj et al., 2006). In these references units are in eV, with the equivalence 1 eV = 96.49 kj/mole. A full review with applications to Earth Sciences is available (Vigneresse and Truche, 2018).

$$\chi = -\mu = -dE/dN \tag{B1}$$

$$\nu = 0.5\, d^2E/dN^2 = 0.5\, d\chi/dN \tag{B2}$$

$$\omega = 0.5 * \chi^2/\nu \tag{B3}$$

Commonly, electronegativity is the derivative to the energy curve, equivalent to velocity. It indicates places of greater stability when it becomes large (i.e. lower potential value). Hardness, its derivative, is the tangential component of acceleration. It is also analogous to the radius of curvature of the energy curve. In a similar way, the inverse of electrophilicity is the second derivative of the inverse of the energy. It is the analogous to the normal acceleration of a dynamic motion (i.e. analogue to the radius of the osculating circle) (Fig. B1). All chemical reactions follow the two principles of maximum hardness (MHP) and minimum electrophilicity (mPP), assuming least energy consumption (Chermette, 1999).

Chemical reactions are places of charge (dN) and energy (dE) exchanges between elements A and B. Those are quantified from the variation of their respective descriptors (Morell et al., 2009).

$$dN = (\chi_A - -\chi_B)/(\nu_A + \nu_B) = d\chi/(2\nu_A + d\nu) \tag{B4}$$

$$dN = (\chi_A - -\chi_B)^2/2(\nu_A + \nu_B) = d\chi^2/2(2\nu_A + d\nu) \tag{B5}$$

At this stage, it seems important to use the two previous descriptors as coordinates for building a diagram that could be analogous to a mapping of the derivatives of the potential. By analogy with potential maps for evolution trends, those diagrams with coordinates [η − ω] are called fitness landscape diagrams (Das et al., 2013; Vigneresse et al., 2014). Both coordinates are in similar units (eV), and the chemical potential is readily drawn on them. However, the interest is to have coordinates to map other chemical elements, as well as their physical of chemical properties. It thus provides new insights to chemical reactions. By analogy with a landscape, the chemical potential could be represented as a succession of highs and lows (e.g. mountains and valleys), whereas the coordinates could indicate the velocity required to travel, either on foot or on vehicle, through the landscape. The corresponding charge and energy exchange would be the fuel and energy consumptions.

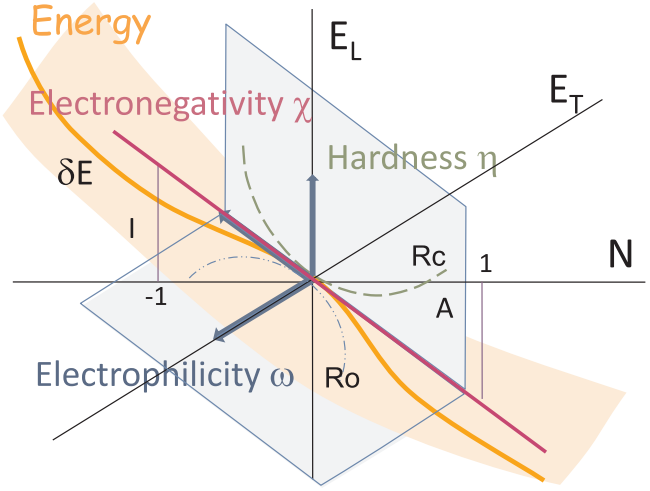

Fig. B1. Geometric representation of the energy surface as a function of the number (N) of electrons within the system. The chemical descriptors are the tangent (electronegativity, χ) as the first derivative (velocity), and the components of the second derivative (acceleration), the tangential component, or radius of curvature (hardness, ν) and the normal component (electrophilicity, ω), similar to the osculating circle.

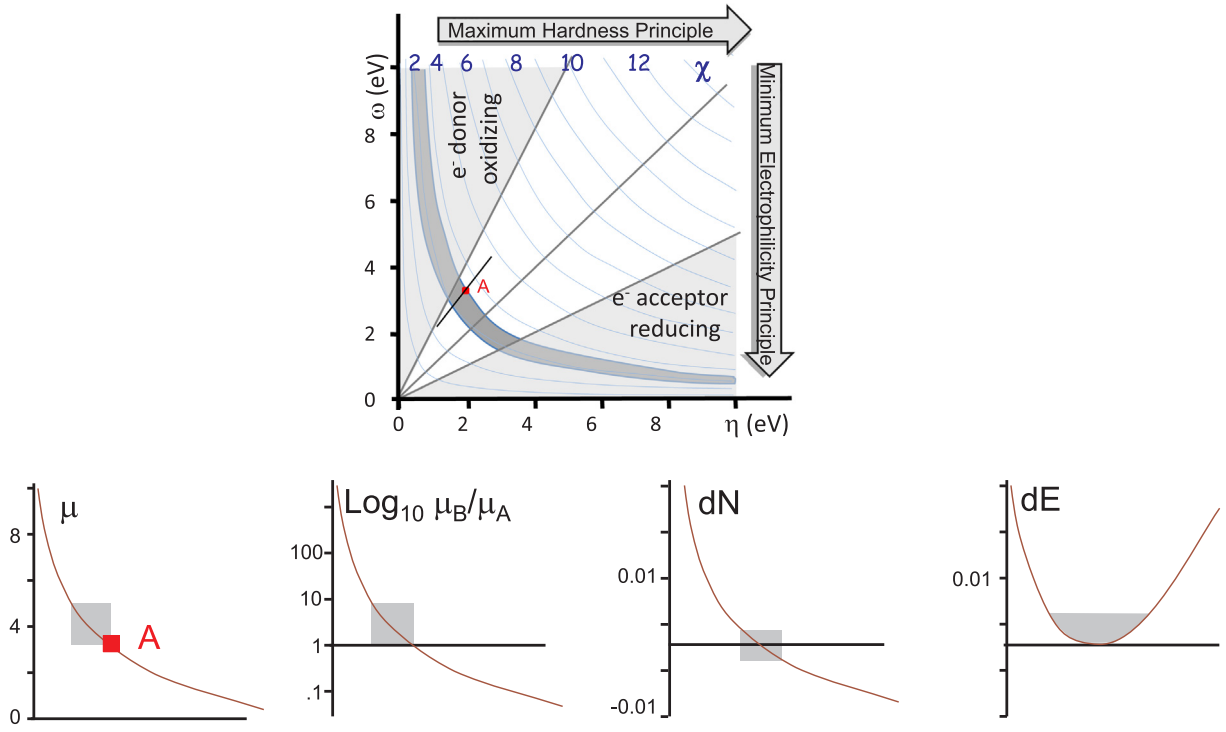

Fig. B2. Schematic representation, not to scale, of the changes in energy and charge, i.e. in chemical potential during a chemical reaction. The reaction occurs between an element A, mapped on a [ν – ω] diagram, on which the chemical potential, or electronegavity (χ) changed of sign is plotted. The successive changes are vertical cross sections along the trend marked by a solid black line. The chemical potential follows a hyperbolic decrease. Normalized with respect to μ, the curve, in log scale, is similar to a scalingof the partition coefficient ($K^{B/A}$). The charge (dN) and energy (dE) exchange profiles determine the lateral range of variation in elements descriptors. According the maximum hardness principle (MHP), the range of possible elements to react with element A is indicated on the map by a darker zone. Also indicated the zones of oxidizing and reducing reactions are limited by lines of maximum charge exchange ($\chi/\nu = 1$ and 2).

The representations of the charge and energy exchanges during a reaction (Fig. B2) both follow a hyperbola on horizontal mapping. In the vertical section, the charge exchange follows a hyperbola, whereas the energy exchange surface is a paraboloid. Chemical reactions develop according to minimum energy exchange, i.e. in the deep part of the valley. A cross section of this valley is easily scaled in chemical potential, following a hyperbolic descent. Scaled in logarithms, with respect to the lower point of the valley, i.e. the value of the chemical potential of one reactant (μ_A), the curve indicates the ratio of the chemical potentials (μ_B/μ_A), i.e. the values of the partition coefficients ($K^{B/A}$) between the two elements. According the the two principles of MHP and mPP, the fitness landscape indicates which elements would preferentially react with element A (Fig. B2). The application to MVP and Cu with different ligands is shown on Fig. 10.

References

Aidun, C.K., Clause, J.R., 2010. Lattice-Boltzmann method for complex flows. Annu. Rev. Fluid Mech. 42, 439–472.

Aiuppa, A., 2009. Degassing of halogens from basaltic volcanism: insights from volcanic gas observations. Chem. Geol. 263, 99–109.

Alidibirov, M., Dingwell, D.B., 1996. Magma fragmentation by rapid decompression. Nature 380, 146–148.

Amaya-Bower, L., Lee, T., 2010. Single bubble rising dynamics for moderate Reynolds number using Lattice Boltzmann Method. Comput. Fluids 7, 1191–1207.

Annen, C., 2009. From plutons to magma chambers: thermal constraints on the accumulation of eruptible silicic magma in the upper crust. Earth Planet. Sci. Lett. 284, 409–416.

Aranacibia, O.N., Clark, A.H., 1966. Early magnetite-amphibole-plagioclase alteration-mineralization in the Island copper porphyry copper-gold-molybdenum deposit, British Columbia. Econ. Geol. 91, 402–438.

Arndt, N., Lesher, C.M., Czamanske, G.K., 2005. Mantle-derived magmas and magmatic Ni-Cu-(PGE) deposits. Econ. Geol. 5–24.

Arndt, N.T., 2013. The lithospheric mantle plays no active role in the formation of orthomagmatic ore deposits. Econ. Geol. 108, 1953–1970.

Audétat, A., Pettke, T., 2003. The magmatic-hydrothermal evolution of two barren granites: a melt and fluid inclusion study of the Rito del Medio and Cañada Pinabete plutons in northern New Mexico (USA). Geochim. Cosmochim. Acta 67, 97–121.

Audétat, A., Pettke, T., Dolejš, D., 2004. Magmatic anhydrite and calcite in the ore-forming quartz-monzodiorite magma at Santa Rita, New Mexico (USA): genetic constraints on porphyry-Cu mineralization. Lithos 72, 147–161.

Audétat, A., Pettke, T., Heinrich, C.A., Bodnar, R.J., 2008. The composition of magmatic-hydrothermal fluids in barren and mineralized intrusions. Econ. Geol. 103, 877–908.

Audétat, A., Simon, A.C., 2012. Magmatic controls on porphyry copper genesis. Econ. Geol. Special Publ. 16, 553–572.

Bachmann, O., Bergantz, G.W., 2006. Gas percolation in upper-crustal silicic crystal mushes as a mechanism for upward heat advection and rejuvenation of near-solidus magma bodies. J. Volcanol. Geoth. Res. 149, 85–102.

Bachmann, O., Bergantz, G., 2008. Deciphering magma chamber dynamics from styles of compositional zoning in large silicic ash flow sheets. Rev. Mineral. Geochem. 69, 651–674.

Bachmann, O., Dungan, M.A., Lipman, P.W., 2002. The Fish Canyon magma body, San Juan volcanic field, Colorado: rejuvenation and eruption of an upper crustal batholithic magma chamber. J. Petrol. 43, 1469–1503.

Bagdassarov, N.S., Dingwell, D.B., 1992. A rheological investigation of vesicular rhyolite. J. Volcanol. Geoth. Res. 50, 307–322.

Bagdassarov, N.S., Dingwell, D.B., Webb, D.L., 1994. Viscoelasticity of crystal-bearing and bubble-bearing rhyolite melts. Phys. Earth Planet. Inter. 83, 83–99.

Bagdassarov, N.S., Dorfmann, A., Dingwell, D.B., 2000. Effect of alkalis, phosphorus, and water on the surface tension of haplogranite melt. Am. Mineral. 85, 33–40.

Bailey, J.C., 1977. Fluorine in granitic rocks and melts: a review. Chem. Geol. 19, 1–42.

Barnes, S.J., Melezhik, V.A., Sokollov, S.V., 2001. The composition and mode of formation of the Pechenga nickel deposits, Kola Peninsula, northwestern Russia. Canad. Mineral. 39, 447–471.

Barra, F., Ruiz, J., Valencia, V.A., Ochoa-Landín, L., Chesley, J.T., Zurcher, L., 2005. Laramide porphyry Cu-Mo mineralization in Northern Mexico: age constraints from Re-Os geochronology in molybdenite. Econ. Geol. 100, 1605–1616.

Bartels, A., Behrens, H., Holtz, F., Schmidt, B.C., Fechtelkord, M., Knipping, J., Crede, L., Baasner, A., Pukallus, N., 2013. The effect of fluorine, boron and phosphorus on the viscosity of pegmatite forming melts. Chem. Geol. 346, 184–198.

Baumgartner, R., Fontboté, L., Spikings, R., Ovtcharova, M., Schaltegger, U., Schneider, J., Pahe, L., Gutjahr, M., 2009. Bracketing the age of magmatic-hydrothermal activity at the Cerro de Pasco epithermal polymetallic deposit, Central Peru: a U-Pb and $^{40}Ar/^{39}Ar$ study. Econ. Geol. 104, 479–504.

Bear, J., 1988. Dynamics of Fluids in Porous Media. Elsevier, New York, pp. 761.

Behn, G., Camus, F., Carrasco, P., 2001. Aeromagnetic signature of porphyry copper systems in Northern Chile and its geologic implications. Econ. Geol. 96, 239–248.

Bellon, H., Pelletier, B., Westercamp, D., 1974. Geochronometric data relative to volcanisms of Martinique. Comptes Rendus Hebdomadaires de l'Académie des Sciences, Paris D279, 457–460.

Benne, D., Rüssell, C., 2005. Diffusivity and incorporation of tin in $Na_2O/CaO/Al_2O_3/SiO_2$ melts. J. Non-Cryst. Solids 351, 1283–1288.

Bergantz, G.W., 2000. On the dynamics of magma mixing by reintrusion: implications for pluton assembly processes. J. Struct. Geol. 22, 1297–1309.

Bergmann, T.I., Incropera, A.S., Lavine, F.P., DeWitt, D.P., 2001. Fundamentals of Heat and Mass Transfer. John Wiley & Sons, New York, pp. 1072.

Bissig, T., Clark, A.H., Lee, J.K.W., von Quadt, A., 2003. Petrogenetic and metallogenetic responses to Miocene slab flattening: new constraints from the El Indio-Pascua Au–Ag–Cu belt, Chile/Argentina. Miner. Deposita 38, 844–862.

Bloom, M.S., 1981. Chemistry of inclusion fluids; stockwork molybdenum deposits from Questa, New Mexico, Hudson Bay Mountain and Endako, British Columbia. Econ. Geol. 76, 1906–1920.

Blundy, J., Wood, B.J., 2003. Partitioning of trace elements between crystals and melts. Earth Planet. Sci. Lett. 210, 383–397.

Bodnar, R., Lecumberi-Sanches, P., Moncada, D., Steele-MacInnis, M., 2014. Chapter 13.5 In: Treatise on Geochemistry. Elsevier, pp. 119–142.

Bogoch, R., Bourne, J., Shirav, M., Harnois, L., 1997. Petrochemistry of a Late Precambrian garnetiferous granite, pegmatite and aplite, Southern Israel. Mineral. Magn. 61, 111–122.

Bohrson, W.A., Spera, F.J., 2001. Energy-constrained open system magmatic processes II: application of energy-constrained assimilation– fractional crystallisation (EC-AFC) model to magmatic systems. J. Petrol. 42, 1019–1041.

Boudreau, B.P., 1996. The diffusive tortuosity of fine-grained unlithified sediments. Geochim. Cosmochim. Acta 60, 3139–3142.

Bray, C.J., Spooner, E.T.C., 1983. Sheeted vein Sn-W mineralization and greisenization associated with economic kaolinization, Goonbarrow china clay pit, St. Austell, Cornwall, England; geologic relationships and geochronology. Econ. Geol. 78, 1064–1089.

Breiter, J., Förster, H.J., Seltmann, R., 1999. Variscan silicic magmatism and related tin-tungsten mineralization in the Erzgebirge-Slavkovský les metallogenic province. Miner. Depos. 34, 505–521.

Breiter, K., 2002. From explosive breccia to unidirectional solidification textures: magmatic evolution of a phosphorus and fluorine-rich granite system (Podlesí, Krušné Hory Mts., Czech Republic). Bull. Czech Geol. Survey 77, 67–92.

Breiter, K., Müller, A., Leichmann, J., Gabašová, A., 2005. Textural and chemical evolution of a fractionated granitic system: the Podlesí stock, Czech Republic. Lithos 80, 323–345.

Bureau, H., Keppler, H., Métrich, M., 2000. Volcanic degassing of bromine and iodine: experimental fluid/melt partitioning data and applications to stratospheric chemistry. Earth Planet. Sci. Lett. 183, 51–60.

Burg, J.P., Vigneresse, J.L., 2002. Non-linear feedback loops in the rheology of cooling-crystallising felsic magma and heating-melting felsic rock. Special Publication 200 In: Drury, M. (Ed.), Deformation Mechanisms, Rheology and Tectonics. Geological Society of London, pp. 275–292.

Burgisser, A., Bergantz, G.W., 2011. A rapid mechanism to remobilize and homogenize highly crystalline magma bodies. Nature 471, 212–215.

Burnham, C.W., 1997. Magmas and hydrothermal fluids. In: Barnes, H.L. (Ed.), Geochemistry of Hydrothermal Ore Deposits **3**. John Wiley and Sons Inc, New York, pp. 63–123.

Campos, E.A., Touret, J., Nikogosian, I., Delgado, J., 2002. Overheated, Cu-bearing magmas in the Zaldívar porphyry-Cu deposit, Northern Chile. Geodynamic consequences. Tectonophysics 345, 229–251.

Campos, E.A., Wijbrans, J., Andriensen, P.A.M., 2009. New thermochronologic constraints on the evolution of the Zaldívar porphyry copper deposit, Northern Chile. Miner. Depos. 44, 329–342.

Candela, P.A., 1989. Felsic magmas, volatiles, and metallogenesis. In: Whitney, J.A., Naldrett, A.J. (Eds.), Ore Deposition Associated with Magmas. Reviews in Economic Geology, pp. 223–233.

Cannell, J., Cooke, D.R., Walshe, J.L., Stein, H., 2005. Geology, mineralization, alteration, and structural evolution of the El Teniente porphyry Cu-Mo deposit. Econ. Geol. 100, 979–1003.

Cao, M., Qin, K., Li, G.M., Evans, N.J., Jin, L.Y., 2015. In situ LA-(MC)-ICP-MS trace element and Nd isotopic compositions and genesis of polygenetic titanite from the Baogutu reduced porphyry Cu deposit, Western Junggar, NW China. Ore Geol. Rev. 65, 940–954.

Caricchi, L., Annen, C., Rust, A., Blundy, J., 2012. Insights into the mechanisms and timescales of pluton assembly from deformation patterns of mafic enclaves. J. Geophys. Res. B 117, B11206. https://doi.org/10.1029/2012JB009325.

Caricchi, L., Burlini, L., Ulmer, P., Gerya, T., Vassalli, M., Papale, P., 2007. Non-Newtonian rheology of crystal-bearing magmas and implications for magma ascent dynamics. Earth Planet. Sci. Lett. 264, 402–419.

Carroll, M.R., Rutherford, M.J., 1987. The stability of igneous anhydrite: experimental results and implications for sulphur behavior in the 1982 El Chichon trachyandesite and other evolved magmas. J. Petrol. 28, 781–801.

Carroll, M.R., Webster, J.D., 1994. Solubilities of sulphur, noble gases, nitrogen, chlorine, and fluorine in magmas. In: Carroll, M.R., Holloway, J.R. (Eds.), Volatiles in Magmas, Reviews in Mineralogy, pp. 231–279.

Carten, R.B., Geraghty, E.P., Walker, B.M., Shannon, J.R., 1988. Cyclic development of igneous features and their relationship to high-temperature hydrothermal features in the Henderson porphyry molybdenum deposit, Colorado. Econ. Geol. 83, 266–296.

Cashman, K.V., Giordano, G., 2014. Calderas and magma reservoirs. J. Volcanol. Geoth. Res. 288, 28–45.

Cashman, K.V., Sparks, R.S.J., Blundy, J.D., 2017. Vertically extensive and unstable magmatic systems: a unified view of igneous processes. Science 355, eaag3055. https://doi.org/10.1126/science.aag3055.

Castro, A.I., Moreno-Ventas, I., de la Rosa, J.D., 1991. H-type (hybrid) granitoids: a proposed revision of the granite-type classification and nomenclature. Earth-Sci. Rev. 31, 237–253.

Cauzid, J., Phillipot, P., Martinez-Criado, G., Ménez, B., Labouré, S., 2007. Contrasting Cu-complexing behaviour in vapour and liquid fluid inclusions from the Yankee Lode tin deposit, Mole Granite, Australia. Chem. Geol. 246, 39–54.

Champallier, R., Bystricky, M., Arbaret, L., 2008. Experimental investigation of magma rheology at 300 MPa: from pure hydrous melt to 76 vol. % of crystals. Earth Planet. Sci. Lett. 267, 571–583.

Chappell, B.W., White, A.J.R., 1977. Two contrasting types of granites. Pac. Geol. 8, 173–174.

Chappell, B.W., White, A.J.R., 2001. Two contrasting granite types: 25 years later. Aust. J. Earth Sci. 48, 489–499.

Chattaraj, P.K., Sarkar, U., Roy, D.R., 2006. Electrophilicity index. Chem. Rev. 106, 2065–2091.

Chelle-Michou, C., Rottier, B., Caricchi, L., Simpson, G., 2017. Tempo of magma degassing and the genesis of porphyry copper deposits. Sci. Rep. 7, 40566. https://doi.org/10.1038/srep40566.

Chermette, H., 1999. Chemical reactivity indexes in density functional theory. J. Comput. Chem. 20, 129–154.

Chiaradia, M., 2014. Copper enrichment in arc magmas controlled by overriding plate

thickness. Nat. Geosci. 7, 43–46.
Chiaradia, M., Schaltegger, U., Spikings, R., Wotzlaw, J.F., Ovtcharova, M., 2013. How accurately can we date the duration of magmatic-hydrothermal events in porphyry systems? -An invited paper. Econ. Geol. 108, 565–584.
Chopard, B., Droz, M., 1998. Cellular Automata Modeling of Physical Systems. Cambridge University Press, Cambridge, pp. 341.
Clarke, D.B., Grujic, D., McCuish, K.L., Sykes, J.C.P., Tweedale, F.M., 2013. Ring schlieren: description and interpretation of field relations in the Halifax Pluton, South Mountain Batholith, Nova Scotia. J. Struct. Geol. 51, 193–205.
Clemens, J.D., 1990. The granulite-granite connexion. In: Vielzeuf, D., Vidal, P. (Eds.), Granulites and Crustal Evolution. Kluwer Academic Publisher, Amsterdam, pp. 25–36.
Clemens, J.D., Petford, N., 1999. Granitic melt viscosity and silicic magma dynamics in contrasting tectonic settings. J. Geol. Soc. London 156, 1057–1060.
Crerar, D.A., Susak, N.J., Borcsik, M., Schwartz, S., 1978. Solubility of the buffer assemblage pyrite + pyrrhotite + magnetite in NaCl solutions from 200 to 350°C. Geochim. Cosmochim. Acta 42, 1427–1437.
Crisp, J.A., 1984. Rates of magma emplacement and volcanic output. J. Volcanol. Geotherm. Resour. 20, 177–211.
Crocket, J.H., Teruta, Y., 1977. Palladium, irridium, and gold content of mafic nd ultraafi rock drilled from the Mid-Atlantic Ridge, Leg 37, Deep Sea Drilling Project. Can. J. Earth Sci. 14, 777–784.
Das, R., Vigneresse, J.L., Chattaraj, P.K., 2013. Redox and Lewis acid–base activities through an electronegativity-hardness landscape diagram. J. Mol. Model. 19, 4857–4864.
de Vries, A.W.G., Biesheuvel, A., van Wijngaarden, L., 2002. Notes on the path and wake of a gas bubble rising in pure water. Int. J. Multiph. Flow 28, 1823–1835.
Deckart, K., Clark, A.H., Celso, A.A., Ricardo, V.R., Bertens, A.N., Mortensen, J.K., Fanning, M., 2005. Magmatic and hydrothermal chronology of the Giant Río Blanco porphyry copper deposit, Central Chile: implications of an integrated U-Pb and $^{40}Ar/^{39}Ar$ database. Econ. Geol. 100, 905–934.
Dilles, J., Einaudi, M.T., 1992. Wall-rock alteration and hydrothermal flow paths about the Ann-Mason porphyry copper deposit, Nevada; a 6-km vertical reconstruction. Econ. Geol. 87, 1963–2001.
Divoux, F., Bertin, E., Vidal, V., Géminard, J.C., 2009. Intermittent outgassing through a non-Newtonian fluid. Phys. Rev. E 79, 056204. https://doi.org/10.1103/PhysRevE.79.056204.
Du, C., Yortsos, Y.C., 1999. A numerical study of the critical gas saturation in a porous medium. Transp. Porous Media 35, 205–225.
Eby, G.N., 1992. Chemical subdivision of the A-type granitoids: petrogenetic and tectonic implications. Geology 20, 641–644.
Edgar, A.D., Pizzolato, L.A., Sheen, J., 1996. Fluorine in igneous rocks and minerals with emphasis on ultrapotassic mafic and ultramafic magmas and their mantle source regions. Mineral. Magn. 60, 243–257.
Edmonds, M., Woods, A.W., 2018. Exsolved volatiles in magma reservoirs. J. Volcanol. Geoth. Res. 368, 13–30.
Eichelberger, J.C., 1975. Origin of andesite and dacite: evidence of mixing at Glass Mountain in California and at other circum-Pacific volcanoes. Geol. Soc. Am. Bull. 86, 1381–1391.
Eichelberger, J.C., Chetkoff, D.G., Dreher, S.T., Nye, C.J., 2000. Magmas in collision: rethinking chemical zonation in silicic magmas. Geology 28, 603–606.
Fan, H.R., Yang, K.F., Hu, F.F., Liu, S., Wang, K.Y., 2016. The giant Bayan Obo REE-Nb-Fe deposit, China: controversy and ore genesis. Geosci. Front. 7, 335–344.
Forien, M., Arbaret, L., Burgisser, A., Champallier, R., 2011. Experimental constrains on shear-induced crystal breakage in magmas. J. Geophys. Res. B 116, B08217. https://doi.org/10.1029/2010JB008026.
Frank, D., Funfschilling, D., Mioux, N., Li, H.Z., 2006. Bubbles in a viscous liquid: lattice Boltzmann simulation and experimental validation. J. Fluid Mech. 546, 113–122.
Gardien, V., Rabinowicz, M., Vigneresse, J.L., Dubois, M., Boulvais, P., Martini, R., 2016. Long-lived interaction between hydrothermal and magmatic fluids in the Soultz-sous-Forêts granitic system (Rhine Graben, France). Lithos 246–247, 110–127.
Gardner, J.E., Hilton, M., Carroll, M.R., 1999. Experimental constraints on degassing of magma: isothermal bubble growth during continuous decompression from high pressure. Earth Planet. Sci. Lett. 168, 201–218.
Giggenbach, W.F., 1987. Redox processes governing the chemistry of fumarolic gas discharges from White Island, New Zealand. Appl. Geochem. 2, 143–161.
Giordano, D., Russell, J.K., Dingwell, D.B., 2008. Viscosity of magmatic liquids: a model. Earth Planet. Sci. Lett. 271, 123–134.
Girona, T., Costa, F., Schubert, G., 2015. Degassing during quiescence as a trigger of magma ascent and volcanic eruptions. Sci. Rep. 5. https://doi.org/10.1038/srep18212.
Goldschmidt, V.M., 1954. Geochemistry. Oxford University Press, Oxford, pp. 730.
Gualda, G.A.R., Ghiorso, M.S., 2013. The Bishop Tuff giant magma body: an alternative to the Standard Model. Contrib. Miner. Petrol. 166, 755–775.
Guineberteau, B., Bouchez, J.L., Vigneresse, J.L., 1987. The Mortagne granite pluton (France) emplaced bypull-apart along a shear zone: structural and gravimetric arguments and regional implication. Geol. Soc. Am. Bull. 99, 763–770.
Gupta, A., Kumar, R., 2008. Lattice Boltzmann simulation to study multiple bubble dynamics. Int. J. Heat Mass Transf. 21–22, 5192–5203.
Gustafson, L.B., Hunt, J.P., 1975. The porphyry copper deposit at El Salvador, Chile. Econ. Geol. 70, 857–912.
Gustafson, L.B., Orquera, W., McWilliams, M., Castro, M., Olivares, O., Rojas, G., Maluenda, J., Mendez, M., 2001. Multiple centers of mineralization in the Indio Muerto District El Salvador, Chile. Econ. Geol. 96, 325–350.
Halter, W.E., Bain, N. Becker, Heinrich, C.A., VonQuadt, A., Clark, A.H., Sasso, A.M., Bissig, T., Tosdal, R.M., 2004. From andesitic volcanism to the formation of a porphyry Cu-Au mineralizing magma chamber: the Farallón Negro Volcanic Complex, northwestern Argentina. J. Volcanol. Geoth. Res. 136, 1–30.
Handy, L.L., 1958. A laboratory study of oil recovery by solution gas drive. AIME Trans. 213, 310–315.
Harris, A.C., Golding, S.D., White, N.C., 2005. Bajo de la Alumbrera copper-gold deposit: stable isotope evidence for a porphyry-related hydrothermal system dominated by magmatic aqueous fluids. Econ. Geol. 100, 863–886.
Harris, A.C., Kamenetsky, V.S., White, N.C., Steele, D.A., 2008. Volatile phase separation in silicic magmas at Bajo de la Alumbrera porphyry Cu-Au deposit, NW Argentina. Resour. Geol. 54, 341–356.
Hattori, K.H., Keith, J.D., 2001. Contribution of mafic melt for porphyry deposits; evidence from Pinatubo and Bingham. Mineral. Dep. 36, 799–806.
Hedenquist, J.W., Lowenstern, J.B., 1994. The role of magmas in the formation of hydrothermal ore deposits. Nature 370, 519–527.
Heinrich, C.A., Günther, D., Audétat, A., Ulrich, T., Frischknecht, R., 1999. Metal fractionation between magmatic brine and vapor, determined by microanalysis of fluid inclusions. Geology 27, 755–758.
Hersum, T., Hilpert, M., Marsh, B., 2005. Permeability and melt flow in simulated and natural partially molten basaltic magmas. Earth Planet. Sci. Lett. 237, 798–814.
Hersum, T.G., Marsh, B.D.I., 2006. Igneous microstructures from kinetic models of crystallization. J. Volcanol. Geoth. Res. 154, 34–47.
Hildreth, W., Moorbath, S., 1998. Crustal contributions to arc magmatism in the Andes of central Chile. Contrib. Miner. Petrol. 98, 455–489.
Hofmann, A.W., 1988. Chemical differentiation of the Earth: the relationship between mantle, continental crust, and oceanic crust. Earth Planet. Sci. Lett. 90, 297–314.
Hollings, P., Wolfe, R., Cooke, D.R., Waters, P.J., 2011. Geochemistry of Tertiary igneous rocks of Northern Luzon, Philippines: evidence for a back-arc setting for alkalic porphyry copper-gold deposits and a case for slab roll-back? Econ. Geol. 106, 1257–1277.
Holmes-Cerfon, M.C., Whitehead, J.A., 2011. Instability and freezing in a solidifying melt conduit. Phys. D 240, 131–139.
Hönig, S., Leichman, J., Novák, M., 2010. Unidirectional solidification textures and garnet layering in Y-enriched garnet-bearing aplite-pegmatites in the Cadomian Brno batholith, Czech Republic. J. Geosci. 55, 113–129.
Huber, C., Bachmann, O., Manga, M., 2009. Homogenization processes in silicic magma chambers by stirring and mushification (latent heat buffering). Earth Planet. Sci. Lett. 283, 38–47.
Huber, C., Bachmann, O., Vigneresse, J.L., Dufek, J., Parmigiani, A., 2012. A physical model for metal extraction and transport in shallow magmatic systems. Geochem. Geophys. Geosyst. 12. https://doi.org/10.1029/2012GC004042.
Huber, C., Parmigiani, A., Chopard, B., Manga, M., Bachmann, O., 2008. Lattice Boltzmann model for melting with natural convection. Int. J. Heat Fluid Flow 29, 1469–1480.
Hudon, P., Baker, D.R., 2002. The nature of phase separation in binary oxide melts and glasses. I. Silicate systems. J. Non-Cryst. Solids 303, 299–345.
Hui, H., Zhang, Y., 2007. Towards a general viscosity equation for natural anhydrous and hydrous silicate melts. Geochim. Cosmochim. Acta 71, 403–416.
Huppert, H.E., Sparks, R.S.J., Whitehead, A., Hallworth, M.A., 1986. Replenishment of magma chambers by light inputs. J. Geophys. Res. B91, 6113–6122.
Hurwitz, S., Navon, O., 1994. Bubble nucleation in rhyolitic melts: experiments at high pressure, temperature, and water content. Earth Planet. Sci. Lett. 122, 267–280.
Ishihara, S., 1977. The magnetite-series and ilmenite-series granitic rocks. Min. Geol. 27, 293–305.
Ishihara, S., 2004. The redox state of granitoids relative to tectonic setting and earth history: the magnetite–ilmenite series 30 years later. Trans. Royal Soc. Edinburgh Earth Sci. 95, 23–33.
Jacobs, D.C., Parry, W.T., 1979. Geochemistry of biotite in the SantaRita porphyry copper deposit, New Mexico. Econ. Geol. 74, 860–887.
Jambon, A., 1982. Tracer diffusion in granitic melts: experimental results for Na, K, Rb, Cs, Ca, Sr, Ba, Ce, Eu to 1300 C and a model of calculation. J. Geophys. Res. B87, 10797–10810.
Jargalan, S., Fujimaki, H., 2003. Origin and solidification age of Baidrag batholith, Tsagaan Tsahir Uul, Mongolia. J. Mineral. Petrol. Sci. 98, 93–103.
Jugo, P.J., 2009. Sulphur content at sulphide saturation in oxidized magmas. Geology 37, 415–418.
Jugo, P.J., Luth, R.W., Richards, J.P., 2005. An experimental study of the sulphur content in basaltic melts saturated with immiscible sulphide or sulphate liquids at 1300 °C and 1.0 GPa. J. Petrol. 46, 783–798.
Kaufmann, J., Rüssell, C., 2010. Diffusion of copper in soda–silicate and soda–lime–silicate melts. J. Non-Cryst. Solids 356, 1158–1162.
Kelson, C.R., Crowe, D.E., Stein, H.J., 2008. Geochemical and geochronological constraints on mineralization within the Hilltop, Lewis, and Bullion mining districts, Battle Mountain-Eureka Trend, Nevada. Econ. Geol. 103, 1483–1506.
Kendrick, M.A., Kamenetsky, V.S., Phillips, D., Honda, M., 2012. Halogen systematics (Cl, Br, I) in Mid-Ocean Ridge Basalts: a Macquarie Island case study. Geochim. Cosmochim. Acta 81, 82–93.
Keppler, H., Wyllie, P.J., 1991. Partitioning of Cu, Sn, Mo, W, U, and Th between melt and aqueous fluid in the systems haplogranite-H_2O- HCl and haplogranite-H_2O- HF. Contrib. Miner. Petrol. 109, 139–150.
Kirby, S.H., Kronenberg, A.K., 1987. Rheology of the lithosphere. Rev. Geophys. 25, 1219–1244.
Kirk, J.D., Ruiz, J., Kesler, S.E., Simon, A., Muntean, J.L., 2014. Re-Os age of the Pueblo Viejo epithermal deposit, Dominican Republic. Econ. Geol. 109, 503–512.
Kishima, N., Sakai, H., 1984. A simple gas analytical technique for Dickson-type hydrothermal apparatus its application to the calibration of MH, NNO and FMQ oxygen buffers. Geochem. J. 18, 19–29.

Klemm, L.M., Pettke, T., Heinrich, C.A., Campos, E., 2007. Hydrothermal evolution of the El Teniente deposit, Chile: porphyry Cu-Mo ore deposition from low-salinity magmatic fluids. Econ. Geol. 102, 1021–1045.
Kohlstedt, D.L., Bai, Q., Wang, Z.C., Mai, S., 2000. Rheology of partially molten rocks. In: Bagdassarov, N., Laporte, D., Thompson, A.B. (Eds.), Physics and Chemistry of Partially Molten Rocks. Kluwer, Dordrecht, pp. 3–28.
Kolb, J., 2008. The role of fluids in partitioning brittle deformation and ductile creep in auriferous shear zones between 500 and 700 °C. Tectonophysics 446, 1–15.
Komrakova, A.E., Shardt, O., Eskin, D., Derksen, J.J., 2014. Lattice Boltzmann simulations of drop deformation and breakup in shear flow. Int. J. Multiph. Flow 59, 24–43.
Kravchenko, S.M., Pokrovsky, B.G., 1995. The Tomtor alkaline ultrabasic massif and related REE-Nb deposits, northern Siberia. Econ. Geol. 90, 676–689.
Kuþcu, Ý., Yilmazer, E., Güleç, N., Bayir, S., Demirela, G., Gençalioðlu, Kuþcu G., Sezerer Kuru, G., Kaymakçi, N., 2011. U-Pb and ^{40}Ar-^{39}Ar geochronology and isotopic constraints on the genesis of copper-gold-bearing iron oxide deposits in the Hasançelebi District, Eastern Turkey. Econ. Geol. 106, 261–288.
Landtwing, M.R., Dillenbeck, E.D., Leake, M.H., Heinrich, C.A., 2002. Evolution of the breccias-hosted porphyry Cu-Mo-Au deposit at Agua Rica, Argentina: progressive unroofing of a magmatic hydrothermal system. Econ. Geol. 97, 1273–1292.
Landtwing, M.R., Furrer, C., Redmond, P.B., Pettke, T., Guillong, M., Heinrich, C.A., 2010. The Bingham Canyon porphyry Cu-Mo-Au deposit. III. Zoned copper-gold ore deposition by magmatic vapor expansion. Econ. Geol. 105, 91–118.
Lang, J.R., Gregory, M.J., Rebagliati, C.M., Payne, J.G., Oliver, J.L., Roberts, K., 2013. Geology and magmatic-hydrothermal evolution of the Giant Pebble porphyry copper-gold-molybdenum deposit, Southwest Alaska. Econ. Geol. 108, 437–462.
Laznica, P., 1999. Quantitative relationships among giant deposits of metals. Econ. Geol. 94, 455–473.
Lee, C.T.A., Lee, T.C., Wu, C.T., 2014. Modeling the compositional evolution of recharging, evacuating, and fractionating (REFC) magma chambers: implications for differentiation of arc magma. Geochim. Cosmochim. Acta 143, 8–22.
Lehmann, S., Barcikowski, J., von Quadt, A., Gallhofer, D., Peytcheva, I., Heinrich, C.A., Serafimovski, T., 2013. Geochronology, geochemistry and isotope tracing of the Oligocene magmatism of the Buchim–Damjan–Borov-Dol ore district: implications for timing, duration and source of the magmatism. Lithos 180–181, 216–233.
Lenormand, D., Touboul, E., Zarcone, C., 1988. Numerical models and experiments on immiscible immiscible displacements in porous media. J. Fluid Mech. 189, 165–187.
Lesher, C.E., 2010. Self-diffusion in silicate melts: theory, observations and applications to magmatic systems. Rev. Mineral. Geochem. 72, 269–309.
Li, X., Hu, R., Rusk, B., Xiao, R., Wang, C., Yang, F., 2013. U-Pb and Ar–Ar geochronology of the Fujiawu porphyry Cu–Mo deposit, Dexing district, Southeast China: implications for magmatism, hydrothermal alteration, and mineralization. J. Asian Earth Sci. 74, 330–342.
Li, Y., Audétat, A., 2012. Partitioning of V, Mn Co, Ni, Cu, Zn, As, Mo, Ag, Sn, Sb, W, Au, Pb, and Bi between sulphide phases and hydrous basanite melt at upper mantle conditions. Geochim. Cosmochim. Acta 75, 1673–1692.
Li, Y., Selby, D., Condon, D., Tapster, S., 2018. Cyclic magmatic-hydrothermal evolution in porphyry systems: high-precision U-Pb and Re-Os geochronology constraints on the Tibetan Qulong porphyry Cu-Mo deposit. Econ. Geol. 112, 141–1440.
Linnen, R.L., Pichavant, M., Holtz, F., 1996. The combined effect of f_{O2} and melt composition on SnO_2 solubility and tin diffusion in haplogranitic melts. Geochim. Cosmochim. Acta 60, 4965–4976.
Linnen, R.L., Pichavant, M., Holtz, F., Burgess, S., 1995. The effect of f_{O2} on the solubility, diffusion, and speciation of tin in haplogranitic melt at 850°C and 2 kbar. Geochim. Cosmochim. Acta 59, 1579–1588.
Liu, H., Ba, Y., Wu, L., Li, Z., Xi, G., Zhang, Y., 2018a. A hybrid lattice Boltzmann and finite difference method for droplet dynamics with insoluble surfactants. J. Fluid Mech. 837, 381–412.
Liu, Y., Chakmouradian, A., Hou, Z., Wenlei, S., Kynický, J., 2018b. Development of REE mineralization in the giant Maoniuping deposit (Sichuan, China): insights from mineralogy, fluid inclusions, and trace-element geochemistry. Miner. Depos. https://doi.org/10.1007/s00126-018-0836-y.
Longo, A.A., Dilles, J.H., Grunder, A.L., Duncan, R., 2010. Evolution of calc-alkaline volcanism and associated hydrothermal gold deposits at Yanacocha, Peru. Econ. Geol. 105, 1191–1241.
Løvoll, G., Méheust, Y., Måløy, K., Aker, E., Schmittbuhl, J., 2005. Competition of gravity, capillary and viscous forces during drainage in a two-dimensional porous medium, a pore scale study. Energy 30, 861–872.
Lu, H.Z., Liu, Y., Wang, C., Xu, Y., Li, H., 2003. Mineralization and fluid inclusion study of the Shizhuyuan W-Sn-Bi-Mo-F skarn deposit, Hunan Province, China. Econ. Geol. 98, 955–974.
Lu, Y.L., Kerrich, R., Kemp, A.I.S., McCuaig, T.C., Hou, Z.Q., Hart, C.J.R., Li, Z.X., Cawood, P.A., Bagas, L., Yang, Z.M., Cliff, J., Belousova, E.A., Jioiurdan, F., Evans, N.J., 2013. Intracontinental Eocene-Oligocene porphyry-Cu mineral systems of Yunnan, Western Yangtze Craton, China: compositional characteristics, sources, and implications for continental collision metallogeny. Econ. Geol. 108, 1541–1576.
Lukanin, O.A., Dernov-Pegarev, V.F., 2010. Partitioning of rare earth elements between an aqueous chloride fluid phase and melt during the decompression-driven degassing of granite magmas. Geochem. Int. 48, 961–978.
Maksaev, V., Munizaga, F., McWilliams, M., Fanning, M., Mathur, R., Ruiz, J., Zentilli, M., 2004. New chronology for El Teniente, Chilean Andes, from U-Pb, $^{40}Ar/^{39}Ar$, Re-Os and fission-track dating: implications for the evolution of a supergiant porphyry Cu-Mo deposit. Soc. Econ. Geol. Special Publ. 11, 15–54.
Mamtani, M.A., 2010. Strain-rate estimation using fractal analysis of quartz grains in naturally deformed rocks. J. Geol. Soc. India 75, 202–209.
Mamtani, M.A., 2012. Fractal analysis of magnetite grains- implications for interpreting deformation mechanisms. J. Geol. Soc. India 80, 308–313.
Manga, M., Loewenberg, M., 2001. Viscosity of magmas containing highly deformable bubbles. J. Volcanol. Geoth. Res. 105, 19–24.
Mangan, M., Sisson, T., 2000. Delayed, disequilibrium degassing in rhyolite magma. Decompression experiments and implications for explosive volcanism. Earth Planet. Sci. Lett. 183, 441–455.
Manneville, P., 1991. Structures Dissipatives. Chaos et Turbulence, Arléa, Saclay, pp. 420.
Markowski, A., Vallance, J., Chiaradia, M., Fontboté, L., 2006. Mineral zoning and gold occurrence in the Fortuna skarn mine, Nambija district, Ecuador. Miner. Depos. 41, 301–321.
Marshall, B., Gilligan, L.B., 1987. An introduction to remobilization: information from ore-body geometry and experimental considerations. Ore Geol. Rev. 2, 87–131.
Martin, H., 1999. Adakitic magmas: modern analogues of Archaean granitoids. Lithos 46, 411–429.
Martin, H., Smithies, R.H., Rapp, R., Moyen, J.F., Champion, D., 2005. An overview of adakite, tonalite–trondhjemite–granodiorite (TTG), and sanukitoid: relationships and some implications for crustal evolution. Lithos 79, 1–24.
Memeti, V., Paterson, S., Matzel, J., Mundil, R., Okaya, D., 2010. Using magmatic lobes as "snapshots" of magma chamber growth to help decipher the growth and evolution of large, composite batholiths: an example from the Tuolumne Intrusion, Sierra Nevada, CA. Geol. Soc. Am. Bull. 122, 1912–1931.
Menand, T., Annen, C., de Saint Blanquat, M., 2015. Rates of magma transfer in the crust: insights into magma reservoir recharge and pluton growth. Geology 43, 199–202.
Mercer, C.N., Reed, M.H., Mercer, C.M., 2015. Time scales of porphyry Cu deposit formation: insights from titanium diffusion in quartz. Econ. Geol. 110, 587–602.
Migdisov, A.A., Williams-Jones, A.E., 2013. A predictive model for metal transport of silver chloride by aqueous vapor in ore-forming magmatic-hydrothermal systems. Geochim. Cosmochim. Acta 104, 123–135.
Misra, M., Burg, J.P., Vigneresse, J.L., Mainprice, D., 2014. Rheological transition during large strain deformation of melting and crystallizing metapelites. J. Geophys. Res. B119. https://doi.org/10.1002/2013JB010777.
Morell, C., Labet, V., Grand, A., Chermette, H., 2009. Minimum electrophilicity principle: an analysis based upon the variation of both chemical potential and absolute hardness. PCCP 14, 3417–3423.
Mungall, J.E., 2002. Empirical models relating viscosity and tracer diffusion in magmatic silicate melts. Geochim. Cosmochim. Acta 66, 125–143.
Mungall, J.E., Su, S., 2005. Interfacial tension between magmatic sulfide and silicate liquids: constraints on kinetics of sulfide liquation and sulfide migration through silicate rocks. Earth Planet. Sci. Lett. 234, 135–149.
Mysen, B.O., 1988. Structure and Properties of Silicate Melts. Elsevier, Amsterdam, pp. 354.
Nadeau, O., Williams-Jones, A.E., Stix, J., 2010. Sulphide magma as a source of metals in arc-related magmatic hydrothermal ore fluids. Nat. Geosci. 3, 501–505.
Nagasawa, H., 1966. Trace element partition coefficient in ionic crystals. Science 152, 767–769.
Navrotsky, A., 1995. Thermodynamic properties of minerals. AGU Reference Shelf 2 In: Rock Physics and Phase Relations. A Handbook of Physical Constants, pp. 18–32.
Norton, D.L., Dutrow, B.L., 2001. Complex behavior of magma-hydrothermal processes: role of supercritical fluid. Geochim. Cosmochim. Acta 65, 4009–4017.
Obenholzner, J.H., Schroettner, H., Golob, P., Delgado, H., 2003. Particles from the plume of Popocatepetl volcano, Mexico – the FESEM/EDS approach. In: Oppenheimer, C., Pyle, D.M., Barclay, J. (Eds.), Volcanic Degassing. Geological Society of London Special Publication, pp. 123–148.
Oyarzun, R., Márquez, A., Lillo, J., Lopez, I., Rivera, S., 2001. Giant versus small porphyry copper deposits of Cenozoic age in northern Chile: adakitic versus normal calc-alkaline magmatism. Miner. Deposita 36, 794–798.
Padilla-Garza, R.A., Titley, S.R., Eastoe, C.J., 2004. Hypogene evolution of the Escondida porphyry copper deposit, Chile. Special Publication 11 In: Sillitoe, R.H., Perello, J., Vidal, C.E. (Eds.), Andean Metallogeny: New Discoveries, Concepts and Updates. Society of Economic Geology, pp. 141–159.
Palabos, 2010. The Palabos software project. http://www.lbmethod.org/palabos/.
Papale, P., 1999. Strain-induced magma fragmentation in explosive eruptions. Nature 397, 425–428.
Parada, M.A., Aracena, I., Tanara, H., 1987. The petrology of the Chuquicamata plutonic complex, Chile. J. Japan. Assoc. Mineral. Petrol. Econ. Geol. 82, 177–188.
Parmigiani, A., Huber, C., Bachmann, O., 2014. Mush microphysics and the reactivation of crystal-rich magma reservoirs. J. Geophys. Res. B119, 6308–6322.
Parmigiani, A., Huber, C., Bachmann, O., Chopard, B., 2011. Pore-scale mass and reactant transport in multiphase porous media flow. J. Fluid Mech. https://doi.org/10.1017/jfm.2011.330.
Parmigiani, A., Huber, C., Chopard, B., Latt, J., Bachmann, O., 2009. Application of the multi distribution function lattice Boltzmann approach to thermal flows. Eur. Phys. J. Special Topics 171, 37–43.
Paterson, L., 1981. Radial fingering in a Hele-Shaw cell. J. Fluid Mech. 113, 513–529.
Paterson, M.S., Olgaard, D.L., 2000. Rock deformation tests to large strains in torsion. J. Struct. Geol. 22, 1341–1358.
Paterson, S.R., Okaya, D., Memeti, V., Economos, R., Miller, R.B., 2011. Magma addition and flux calculations of incrementally constructed magma chambers in continental margin arcs: combined field, geochronologic, and thermal modeling studies. Geosphere 7, 1439–1468.
Pearson, R.G., 1963. Hard and soft acids and bases. J. Am. Chem. Soc. 85, 3533–3539.
Pearson, R.G., 1988. Absolute electronegativity and hardness: application to inorganic chemistry. Inorg. Chem. 27, 734–740.
Pelletier, J.D., 1999. Statistical self-similarity of magmatism and volcanism. J. Geophys. Res. B104, 15425–15438.
Persikov, E.S., Bukhtiyarov, P.G., Sokol, A.G., 2015. Viscosity of hydrous kimberlite and basaltic melts at high pressures. Russ. Geol. Geophys. 58, 1093–1100.

Petford, N., Cruden, A.R., McCaffrey, K.J.W., Vigneresse, J.L., 2000. Granite magma formation, transport and emplacement in the Earth's crust. Nature 408, 669–673.
Pettke, T., Oberli, F., Heinrich, C.A., 2010. The magma and metal source of giant porphyry-type ore deposits, based on lead isotope microanalysis of individual fluid inclusions. Earth Planet. Sci. Lett. 296, 267–277.
Pistone, M., Caricchi, L., Ulmer, P., Burlini, L., Ardia, P., Reusser, E., Marone, F., Arbaret, L., 2012. Deformation experiments of bubble- and crystal-bearing magmas: rheological and microstructural analysis. J. Geophys. Res. B 117, B05208. https://doi.org/10.1029/2011JB008986.
Pistone, M., Caricchi, L., Ulmer, P., Reusser, E., Ardia, P., 2013. Rheology of volatile-bearing crystal mushes: mobilization vs. viscous death. Chem. Geol. 345, 16–39.
Rabbia, O.M., Hernandez, L.B., French, D.H., King, R.W., Ayers, J.C., 2009. The El Teniente porphyry Cu-Mo deposit from a hydrothermal rutile perspective. Miner. Deposita 44, 849–866.
Rabinowicz, M., Vigneresse, J.L., 2004. Melt segregation under compaction and shear channelling: application to granitic magma segregation in a continental crust. J. Geophys. Res. B109. https://doi.org/10.1029/2002JB002372.
Reich, M., Parada, P., Palacios, C., Dietrich, A., Schultz, F., Lehmann, B., 2003. Adakite-like signature of Late Miocene intrusions at the Los Pelambres giant porphyry copper deposit in the Andes of central Chile: metallogenic implications. Miner. Deposita 38, 876–885.
Rice, C.M., Steele, G.B., Barfod, D.N., Boyce, A.J., Pringle, M.S., 2005. Duration of magmatic, hydrothermal and supergene activity at Cerro Rico de Potosi, Bolivia. Econ. Geol. 100, 1647–1656.
Richards, J.P., 2003. Tectono-magmatic precursors for porphyry Cu-(Mo-Au) deposit formation. Econ. Geol. 98, 1515–1533.
Richards, J.P., 2009. Postsubduction porphyry Cu–Au and epithermal Au deposits: products of remelting of subduction-modified lithosphere. Geology 37, 247–250.
Richards, J.P., 2011. Magmatic to hydrothermal metal fluxes in convergent and collided margins. Ore Geol. Rev. 40, 1–26.
Richards, J.P., 2013. Giant ore deposits formed by optimal alignments and combinations of geological processes. Nat. Geosci. 6, 911–916.
Ripley, E.M., Li, C., 2018. A review of the application of multiple isotopes to magmatic Ni-Cu-PGE deposits and the significance of spatially variable $\Delta^{33}S$ values. Econ. Geol. 112, 983–991.
Roedder, E., 1971. Fluid inclusion studies on the porphyry-type ore deposits at Bingham, Utah, Butte, Montana and Climax Colorado. Econ. Geol. 66, 98–120.
Romer, R.L., Kroner, U., 2018. Paleozoic gold in the Appalachians and Variscides. Ore Geol. Rev. 92, 475–505.
Rowins, S.M., 2000. Reduced porphyry copper-gold deposits: a new variation on an old theme. Geology 28, 491–494.
Rudnick, R.L., Gao, S., 2003. Composition of the continental crust. In: Rudnick, R.L. (Ed.), Treatise On Geochemistry. Elsevier, Amsterdam, pp. 1–64.
Rusk, B.G., Reed, M.H., Dilles, J.H., Klemm, L.M., Heinrich, C.A., 2004. Compositions of magmatic hydrothermal fluids determined by LA-ICP-MS of fluid inclusions from the porphyry copper-molybdenum deposit at Butte, MT. Chem. Geol. 210, 173–199.
Rust, A.C., Manga, M., Cashman, K.V., 2003. Determining flow type, shear rate and shear stress in magmas from bubble shapes and orientations. J. Volcanol. Geoth. Res. 122, 111–132.
Rutter, E.H., Neumann, D.H.K., 1995. Experimental deformation of partially molten Westerly granite under fluid-absent conditions with implications for the extraction of granitic magma. J. Geophys. Res. B100, 15697–15715.
Schoene, B., Schaltegger, U., Brack, P., Latkoczy, C., Stracke, A., Günther, D., 2012. Rates of magma differentiation and emplacement in a ballooning pluton recorded by U-Pb TIMS-TEA, Adamello batholith, Italy. Earth Planet. Sci. Lett. 355–356, 162–173.
Schöpa, A., Annen, C., Dilles, J.H., Sparks, S.J., Blundy, J.D., 2018. Magma emplacement rates and porphyry copper deposits: thermal modeling of the Yerington Batholith, Nevada. Econ. Geol. 112, 1653–1672.
Schwartz, M.O., Rajah, S.S., Askury, A.K., Putthapiban, P., Sjaswadi, S., 1995. The southeast Asian tin belt. Earth-Sci. Rev. 38, 95–293.
Seo, J.H., Guillong, M., Heinrich, C.A., 2009. The role of sulphur in the formation of magmatic–hydrothermal copper–gold deposits. Earth Planet. Sci. Lett. 282, 323–328.
Shannon, J.R., Walker, B.M., Carten, R.B., Geraghty, E.P., 1982. Unidirectional solidification textures and their significance in determining relative ages of intrusions at the Henderson Mine, Colorado. Geology 10, 293–297.
Shen, L., Chen, Z., 2007. Critical review of the impact of tortuosity on diffusion. Chem. Eng. Sci. 62, 3748–3755.
Shew, W.L., Poncet, S., Pinton, J.F., 2006. Force measurements on rising bubbles. J. Fluid Mech. 569, 51–60.
Shields, J.K., Mader, H.M., Pistone, M., Caricchi, L., Floess, D., Putlitz, B., 2014. Strain-induced outgassing of three-phase magmas during simple shear. J. Geophys. Res. B119, 6936–6957.
Sillitoe, R.H., 1973. The tops and bottoms of porphyry copper deposits. Econ. Geol. 68, 799–815.
Sillitoe, R.H., 2010. Porphyry copper systems. Econ. Geol. 105, 3–41.
Simmons, A.T., Tosdal, R.M., Wooden, J.L., Mattos, R., Concha, O., McCracken, S., Beale, T., 2013. Punctuated magmatism associated with porphyry Cu-Mo formation in the Paleocene to Eocene of Southern Peru. Econ. Geol. 108, 625–639.
Simon, A.C., Pettke, T., Candela, P.A., Piccoli, P.M., Heinrich, C.A., 2006. Copper partitioning in a melt–vapor–brine–magnetite–pyrrhotite assemblage. Geochim. Cosmochim. Acta 70, 5583–5600.
Sinclair, W.D., 2007. Porphyry deposits. Mineral Deposits Division, Special Publication 5 In: Goodfellow, W.D. (Ed.), Mineral Deposits of Canada: A Synthesis of Major Deposit-Types, District Metallogeny, the Evolution of Geological Provinces, and Exploration Methods. Geological Association of Canada, pp. 223–243.
Smith, C.M., Canil, D., Rowins, S.M., Friedman, R., 2012. Reduced granitic magmas in an arc setting: the Catface porphyry Cu-Mo deposit of the Paleogene Cascade Arc. Lithos 154, 361–373.
Solano, J.M.S., Jackson, M.D., Sparks, R.S.J., Blundy, J.D., Annen, C., 2012. Melt segregation in deep crustal hot zones: a mechanism for chemical differentiation, crustal assimilation and the formation of evolved magmas. J. Petrol. 53, 1999–2026.
Spencer, E.T., Wilkinson, J.J., Creaser, R.A., Seguel, J., 2015. The distribution and timing of molybdenite mineralization at the El Teniente Cu-Mo porphyry deposit, Chile. Econ. Geol. 110, 387–421.
Spray, J.G., 1992. A physical basis for the frictional melting of some rock forming minerals. Tectonophysics 204, 205–221.
Štemprok, M., 1982. Tin-fluorine-relationships-in-ore-bearing-assemblages. In: Evans, A.M. (Ed.), Metallization Associated with Acid Magmatism. Wiley & Sons, pp. 321–337.
Symonds, R.B., Rose, W.I., Reed, M.H., Lichte, F.E., Finnegan, D.L., 1987. Volatilization, transport and sublimation of metallic and non-metallic elements in high temperature gases at Merapi Volcano, Indonesia. Geochim. Cosmochim. Acta 51, 2083–2101.
Taran, Y.A., Bernard, A., Gavilanes, J.C., Africano, F., 2000. Native gold in mineral precipitates from high-temperature volcanic gases of Colima volcano, Mexico. Appl. Geochem. 15, 337–346.
Taran, Y.A., Hedenquist, J.W., Korzhinsky, M.A., Tkachenko, S.I., Schmulovich, K.I., 1995. Geochemistry of magmatic gases from Kudryavy volcano, Iturup, Kuril Islands. Geochim. Cosmochim. Acta 59, 1749–1761.
Thompson, J.F.H., Sillitoe, R.H., Baker, T., Lang, J.R., Mortensen, J.K., 1999. Intrusion-related gold deposits associated with tungsten–tin provinces. Miner. Deposita 34, 323–334.
Taylor, H.P., 1974. The application of oxygen and hydrogen isotope studies to problems of hydrothermal alteration and ore deposition. Econ. Geol. 69, 843–883.
Ulrich, T., Günther, D., Heinrich, C.A., 1999. Gold concentrations of magmatic brines and the metal budgets of porphyry copper deposits. Nature 399, 676–679.
Ulrich, T., Heinrich, C.A., 2001. Geology and alteration geochemistry of the porphyry Cu-Au deposit at Bajo de la Alumbrera, Argentina. Econ. Geol. 96, 1719–1742.
Valencia, V.A., Eastoe, C., Ruiz, J., Ochoa-Landin, L., Gehrels, G., González-Leon, C., Barra, F., Espinoza, E., 2008. Hydrothermal evolution of the porphyry copper deposit at La Caridad, Sonora, Mexico, and the relationship with a neighboring high-sulphidation epithermal deposit. Econ. Geol. 103, 473–491.
Van Brakel, J., Heertjes, P.M., 1974. Analysis of diffusion in macroporous media in terms of a porosity, a tortuosity and a constrictivity factor. Int. J. Heat Mass Transf. 17, 1093–1103.
Vidal, V., Soubiran, F., Divoux, F., Géminard, J.C., 2011. Degassing cascades in a shear-thinning viscoelastic fluid. Phys. Rev. E 84, 066302. https://doi.org/10.1103/PhysRevE.84.066302.
Vigneresse, J.L., 1995. Control of granite emplacement by regional deformation. Tectonophysics 249, 173–186.
Vigneresse, J.L., 2006. Element mobility in melts during successive intrusions of crustal-derived magmas and Sn-W mineralization. Resour. Geol. 56, 293–314.
Vigneresse, J.L., 2007. The role of discontinuous magma inputs in felsic magma and ore generation. Ore Geol. Rev. 30, 181–216.
Vigneresse, J.L., 2008. Granitic batholiths: from pervasive and continuous melting in the in the lower crust to discontinuous and spaced plutonism in the upper crust. Trans. Royal Soc. Edinburgh Earth Sci. 97, 311–324.
Vigneresse, J.L., 2015. Textures and melt-crystal-gas interactions in granites. Geosci. Front. 6, 635–663.
Vigneresse, J.L., 2019. Addressing ore formation and explorations. Geosci. Front in press.
Vigneresse, J.L., Barbey, P., Cuney, M., 1996. Rheological transitions during partial melting and crystallization with application to felsic magma segregation and transfer. J. Petrol. 37, 1597–1600.
Vigneresse, J.L., Burg, J.P., 2000. Continuous vs discontinuous melt segregation in migmatites: insights from a cellular automaton model. Terra Nova 12, 188–192.
Vigneresse, J.L., Duley, S., Chattaraj, P.K., 2011. Describing the chemical character of a magma. Chem. Geol. 287, 102–113.
Vigneresse, J.L., Truche, L., 2018. Chemical descriptors for describing physico-chemical properties with applications to geosciences. J. Mol. Model. 24, 231. https://doi.org/10.1007/s00894-018-3770-0.
Vigneresse, J.L., Truche, L., Chattaraj, P.K., 2014. Metal (copper) segregation in magmas. Lithos 208–209, 462–470.
Yuan, Z., Bai, G., Wu, C., Zhang, Z., Ye, X., 1992. Geological features and genesis of the Bayan Obo REE ore deposit, Inner Mongolia, China. Appl. Geochem. 7, 429–442.
Von der Gönna, G., Rüssell, C., 2000. Diffusivity of Various Polyvalent Elements in a Na_2O- $2SiO_2$.
Vry, V.H., Wilkinson, J.J., Seguel, J., Millan, J., 2010. Multistage intrusion, brecciation and veining at El Teniente, Chile: evolution of a nested porphyry system. Econ. Geol. 105, 119–153.
Wallace, P., Anderson Jr., A.T., 2000. Volatiles in magmas. In: Encyclopedia of Volcanoes. Academic Press, pp. 149–170.
Wallace, P.J., 2001. Volcanic SO_2 emissions and the abundance and distribution of exsolved gas in magma bodies. J. Volcanol. Geoth. Res. 108, 85–106.
Webb, S.L., Dingwell, D.B., 1990. Non-Newtonian rheology of igneous melts at high stresses and strain rates: experimental results for rhyolite, andesite, basalt and nephelinite. J. Geophys. Res. B95, 15695–15701.
Webster, J.D., Tappen, C.M., Mandeville, C.W., 2009. Partitioning behavior of chlorine and fluorine in the system apatite–melt–fluid. II: felsic silicate systems at 200 MPa. Geochim. Cosmochim. Acta 73, 559–581.
Wenchang, L., Pusheng, Z., Zengqian, H., White, N.C., 2011. The Pulang porphyry copper deposit and associated felsic intrusions in Yunnan Province, Southwest China. Econ. Geol. 106, 79–92.
White, S., Crisp, J.A., Spera, F.J., 2006. Long-term volumetric eruption rates and magma

budgets. Q03010. Geochem. Geophys. Geosyst. 7. https://doi.org/10.1029/2005GC001002.
Wilkinson, D., Willemsen, J.F., 1983. Invasion percolation: a new form of percolation theory. J. Phys. A 16, 3365. https://doi.org/10.1088/0305-4470/16/14/028.
Wilkinson, J.J., 2013. Triggers for the formation of porphyry ore deposits in magmatic arcs. Nat. Geosci. 6, 917–925.
Williams-Jones, A.E., Heinrich, C.A., 2005. Vapor transport of metals and the formation of magmatic-hydrothermal ore deposits. Econ. Geol. 100, 1287–1312.
Williamson, B.J., Herrington, R.J., Morris, A., 2016. Porphyry copper enrichment linked to excess aluminium in plagioclase. Nat. Geosci. 9, 237–241.
Yoshinobu, A.S., Okaya, D.A., Paterson, S.R., 1998. Modelling the thermal evolution of fault-controlled magma emplacement models. J. Struct. Geol. 20, 1205–1218.
Zajacz, Z., 2015. The effect of melt composition on the partitioning of oxidized sulphur between silicate melts and magmatic volatiles. Geochim. Cosmochim. Acta 158, 223–244.
Zajacz, Z., Candela, P.A., Piccoli, P.C., Sanchez-Valle, C., Wälle, M., 2013. Solubility and partitioning behavior of Au, Cu, Ag and reduced S in magmas. Geochim. Cosmochim. Acta 112, 288–304.
Zajacz, Z., Halter, W., 2009. Copper transport by high temperature, sulphur-rich magmatic vapor: evidence from silicate melt and vapor inclusions in a basaltic andesite from the Villarrica volcano (Chile). Earth Planet. Sci. Lett. 282, 115–121.
Zajacz, Z., Halter, W.E., Pettke, T., Guillong, M., 2008. Determination of fluid/melt partition coefficients by LA-ICPMS analysis of co-existing fluid and silicate melt inclusions: controls on element partitioning. Geochim. Cosmochim. Acta 72, 2169–2197.
Žák, J., Paterson, S.R., Memeti, V., 2007. Four magmatic fabrics in the Tuolumne batholith, central Sierra Nevada, California (USA): implications for interpreting fabric patterns in plutons and evolution of magma chambers in the crust. Geol. Soc. Am. Bull. 119, 187–201.
Zalc, J.M., Reyes, S.V., Iglesia, E., 2004. The effects of diffusion mechanism and void structure on transport rates and tortuosity factors in complex porous structures. Chem. Eng. Sci. 59, 2947–2960.
Zelenski, M., Bortnikova, S., 2005. Sublimate speciation at Mutnovsky volcano, Kamchatka. Eur. J. Mineral. 17, 107–118.
Zellmer, G.F., Annen, C., Charlier, B.L.A., George, R.M.M., Turner, S.P., Hawkesworth, C.J., 2005. Magma evolution and ascent at volcanic arcs: constraining petrogenetic processes through rates and chronologies. J. Volcanol. Geoth. Res. 140, 171–191.
Zhang, Y., 2010. Diffusion in minerals and melts: theoretical background. Rev. Mineral. Geochem. 72, 5–59.
Zhang, Y., Ni, H., Chen, Y., 2010. Diffusion data in silicate melts. Rev. Mineral. Geochem. 72, 311–408.

Further reading

Pearson, R.G., 1997. Chemical Hardness. John Wiley and Sons, New York, pp. 210.